

Monopole Classical Solutions and the Vacuum Structure in Lattice Gauge Theories¹

V. K. Mitrjushkin

Joint Institute for Nuclear Research, Dubna, Moscow region, 141980 Russia
e-mail: vmitr@thsun1.jinr.ru

Received May 19, 2000

Classical solutions corresponding to monopole–antimonopole pairs are found in 3d and 4d $SU(2)$ and $U(1)$ lattice gauge theories. The stability of these solutions in various theories is studied. © 2000 MAIK “Nauka/Interperiodica”.

PACS numbers: 11.15.Ha

One of the most interesting and still unresolved problems is the structure of a (nonperturbative) vacuum in QCD and a confinement mechanism.

At present, we have a number of different competing scenarios of confinement. One of the most promising approaches is a quasiclassical approach promoted by Polyakov [1], which assumes that in the treatment of infrared problems certain classical field configurations are of paramount importance. These classical field configurations (“pseudoparticles”) are supposed to be stable; i.e., they correspond to local minima of the action, and the interaction of these pseudoparticles creates a correlation length which corresponds to a new scale-confinement scale. This approach gives a clear field-theoretical prescription of how to calculate analytically nonperturbative observables in the weak coupling region. In principle, this approach can be extended to the case of “quasi-stable” solutions.

Another very attractive approach is a topological (or monopole) mechanism of confinement [2]. This mechanism suggests that the QCD vacuum state behaves like a magnetic (dual) superconductor, abelian magnetic monopoles playing the role of Cooper pairs, at least for the specially chosen (“maximally abelian”) gauge [3]. For the time being, this approach remains the most popular one in numerical studies in lattice QCD.

It is rather tempting to try to interpret lattice (abelian) monopoles as pseudoparticles (stable or quasi-stable). Recently, classical solutions have been found which correspond to Dirac sheet (i.e., flux tube) configurations [4]. It is the aim of this note to study the monopole-like ($M\bar{M}$) abelian solutions of classical equations of motion in $SU(2)$ and $U(1)$ lattice gauge theories in $d = 3$ and $d = 4$ dimensions.

In what follows, periodic boundary conditions are presumed. Lattice derivatives are $\partial_\mu f_x = f_{x+\mu} - f_x$, $\bar{\partial}_\mu f_x =$

$f_x - f_{x-\mu}$, and $\bar{\nabla}_\mu(U)f_x = f_x - U_{x-\mu}^\dagger \cdot_\mu f_{x-\mu} U_{x-\mu}$. $\Delta = -\sum_\mu \partial_\mu \bar{\partial}_\mu$, and the lattice spacing is chosen to be unity.

ABELIAN CLASSICAL SOLUTIONS

Iterative procedure. Classical equations of motion are

$$\sum_\mu \text{ImTr} \{ \sigma^a \bar{\nabla}_\mu U_{x\mu\nu} \} = 0, \quad (1)$$

where $U_{x\mu\nu} \in SU(2)$. For abelian solutions $U_{x\mu\nu} = \exp(i\sigma_3 \theta_{x\mu\nu})$, Eq. (1) becomes

$$\sum_\nu \bar{\partial}_\nu \sin \theta_{x\mu\nu} = 0. \quad (2)$$

Let us represent the plaquette angle $\theta_{x\mu\nu}$ in the form

$$\theta_{x\mu\nu} = \tilde{\theta}_{x\mu\nu} + 2\pi n_{x\mu\nu}; \quad -\pi < \tilde{\theta}_{x\mu\nu} \leq \pi, \quad (3)$$

and $n_{x\mu\nu} = -n_{x\nu\mu}$ are integer numbers. The classical equations of motion (2) can be represented in the form

$$\sum_\nu \bar{\partial}_\nu \theta_{x\mu\nu} = F_{x\mu}(\theta), \quad (4)$$

where

$$F_{x\mu}(\theta) \equiv \sum_\nu \bar{\partial}_\nu (\theta_{x\mu\nu} - \sin \theta_{x\mu\nu}) \quad (5)$$

and $\sum_\mu \bar{\partial}_\mu F_{x\mu} = 0$. For any given configuration $\{n_{x\mu\nu}\}$, these equations can be solved iteratively:

$$\theta_{x\mu}^{(1)} \longrightarrow \theta_{x\mu}^{(2)} \longrightarrow \dots \longrightarrow \theta_{x\mu}^{(k)} \longrightarrow \dots, \quad (6)$$

¹This article was submitted by the author in English.

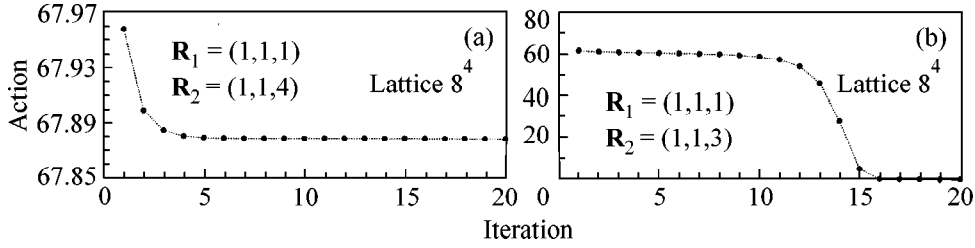


Fig. 1. Iterative solution of the classical equations.

where

$$\sum_{\nu} \bar{\partial}_{\nu} \theta_{x\nu\mu}^{(k+1)} = F_{x\mu}(\theta^{(k)}); \quad k = 1; 2; \dots \quad (7)$$

and

$$\sum_{\nu} \bar{\partial}_{\nu} \theta_{x\nu\mu}^{(1)} = 2\pi \sum_{\nu} \bar{\partial}_{\nu} n_{x\nu\mu}. \quad (8)$$

In the Lorentz gauge $\sum_{\nu} \bar{\partial}_{\nu} \theta_{x\mu} = 0$, Eqs. (7), (8) are equivalent to

$$\Delta \theta_{x\mu}^{(k+1)} = J_{x\mu}^{(k)}; \quad k = 0; 1; \dots, \quad (9)$$

where $J_{x\mu}^{(0)} = 2\pi \sum_{\nu} \bar{\partial}_{\nu} n_{x\nu\mu}$ and $J_{x\mu}^{(k)} = F_{x\mu}(\theta^{(k)})$ at $k \geq 1$. Evidently,

$$\sum_{\mu} \bar{\partial}_{\mu} J_{x\mu}^{(k)} = 0; \quad \sum_x J_{x\mu}^{(k)} = 0. \quad (10)$$

Defining the propagator

$$G_{x;y} = \frac{1}{V} \sum_{q \neq 0} \frac{e^{iq(x-y)}}{\mathcal{J}^2}; \quad \mathcal{J}^2 = \sum_{\mu} 4 \sin^2 \frac{q_{\mu}}{2}, \quad (11)$$

one can easily find solutions of Eq. (9):

$$\theta_{x\mu}^{(1)} = 2\pi \sum_{y\nu} G_{x;y} \bar{\partial}_{\nu} n_{x\nu\mu}; \quad (12)$$

$$\theta_{x\mu}^{(k+1)} = \sum_y G_{x;y} J_{y\mu}^{(k)}; \quad \sum_{\mu} \bar{\partial}_{\mu} \theta_{x\mu}^{(k+1)} = 0, \quad (13)$$

and $\sum_x \theta_{x\mu}^{(k+1)} = 0$.

The results of the iterative solution can be summarized as follows.

1. The convergence of this iterative procedure is very fast and becomes even faster with increasing distance between the monopole and antimonopole. As an example, the dependence of the action on the number of iterations on the 8^4 lattice, where \mathbf{R}_1 and \mathbf{R}_2 are positions of the static monopole and antimonopole, respectively, is shown in Fig. 1a. In fact, the first approxima-

tion $\theta_{x\mu}^{(1)}$, as given in Eq. (12), is a very good approximation to the exact solution.

2. There are no solutions if the monopole and anti-monopole are too close to each other. As an example, in Fig. 1b, one can see the dependence of the action on the number of iteration steps for $\mathbf{R}_2 - \mathbf{R}_1 = (0, 0, 2)$.

3. In four dimensions, only *static* (i.e., three-dimensional) solutions have been found.

STABILITY

The question of stability of the classical solution $U_{x\mu}^{cl}$ is the question of the eigenvalues λ_j of the matrix $L_{xy; \mu\nu}^{ab}$, where

$$S(e^{i\delta\theta} U^{cl}) = S_{cl} + \sum_{abxy\mu\nu} \delta\theta_{x\mu}^a L_{xy; \mu\nu}^{ab} \delta\theta_{y\nu}^b + \dots, \quad (14)$$

where $S_{cl} = S(U^{cl})$ and $\delta\theta_{x\mu}^a$ are infinitesimal variations of the gauge field. A solution $U_{x\mu}^{cl}$ is stable if all $\lambda_j \geq 0$. However, a solution can be unstable but quasi-stable if, say, only one eigenvalue is negative: $\lambda_1 < 0$, $\lambda_j \geq 0$, $j \neq 1$. A cooling history of such a configuration might demonstrate an approximate plateau. If it were the case, one could extend, in principle, Polyakov's approach to the case of quasistable solutions.

It is rather easy to show that in the case of $U(1)$ theory $M\bar{M}$ solutions are stable; i.e., they correspond to local minima of the action. Therefore, Polyakov's approach based on the $M\bar{M}$ classical solutions is expected to describe confinement, and pseudoparticles are (anti)monopoles.

The stability of $M\bar{M}$ classical solutions in $SU(2)$ theory was studied numerically. For this purpose, every classical $M\bar{M}$ -configuration was (slightly) heated and then a (soft) cooling procedure was used. In Fig. 2, one can see a typical cooling history of such a configuration. The classical action S_{cl} corresponding to the $M\bar{M}$ -configuration is ~ 130 . Therefore, the $M\bar{M}$ classical solution looks absolutely unstable.

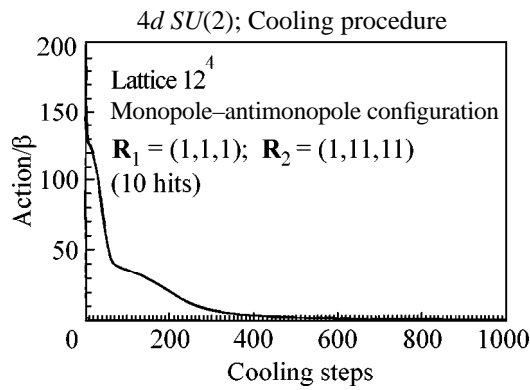


Fig. 2.

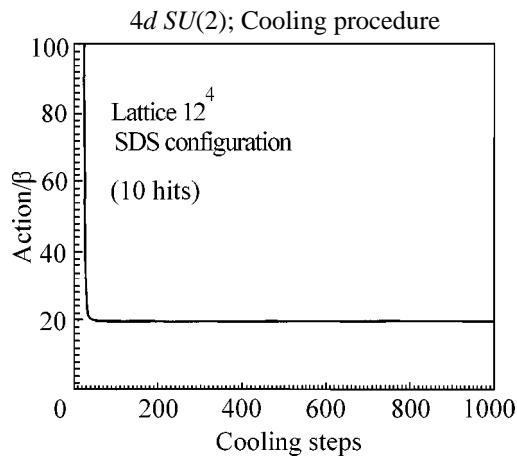


Fig. 3.

It is interesting to compare the stability of monopole classical solutions with that of Dirac sheet (flux tube) solutions. In Fig. 3, one can see a typical cooling of a heated single Dirac sheet (SDS) [4] in $SU(2)$ theory. Parameters of the cooling were chosen to be the same for all configurations. In fact, it is also unstable. However, a strong plateau permits this configuration to be defined as quasi-stable.

SUMMARY AND DISCUSSIONS

Classical solutions corresponding to monopole-antimonopole pairs in $3d$ and $4d$ $SU(2)$ and (compact) $U(1)$ lattice gauge theories have been found.

In the case of $3d$ and $4d$ $U(1)$ theories, these monopole-antimonopole classical solutions ($M\bar{M}$ pseudoparticles) are stable; i.e., they correspond to local minima of the action. Therefore, the quasiclassical approach has a chance to be successful.

In contrast, in $SU(2)$ theory ($d = 3$ and $d = 4$), $M\bar{M}$ classical solutions are completely unstable. At the moment, it is not clear whether Polyakov's (quasiclassical) approach can be applied to nonabelian theories (at least, with monopoles as pseudoparticles). It is very probable that the vacuum in the (compact) $U(1)$ theory is a rather poor model of the vacuum in $SU(2)$ theory.

It is interesting to note that the Dirac sheet (i.e., flux tube) solutions are quasi-stable in $SU(2)$ theories (for $d = 3$ and $d = 4$). This observation could be interesting in view of the famous spaghetti vacuum picture where the color magnetic quantum liquid state is a superposition of flux-tube states (Copenhagen vacuum) [5]. However, the relevance of this scenario still needs further confirmation.

This work was supported by the INTAS (grant no. 96-370), the Russian Foundation for Basic Research (project no. 99-01-01230), and the JINR Dubna Heisenberg-Landau program.

REFERENCES

1. A. M. Polyakov, Phys. Lett. B **59**, 82 (1975); Nucl. Phys. B **120**, 429 (1977).
2. G.'t Hooft, in *Proceedings of the EPS International Conference on High Energy Physics, Palermo, 1975*, Ed. by A. Zichichi (Editrice Compositori, Bologna, 1976); S. Mandelstam, Phys. Rep. C **23**, 245 (1976).
3. A. S. Kronfeld, G. Schierholz, and U.-J. Wiese, Nucl. Phys. B **293**, 461 (1987).
4. V. K. Mitryushkin, Phys. Lett. B **389**, 713 (1996).
5. N. K. Nielsen and P. Olesen, Nucl. Phys. B **144**, 376 (1978); J. Ambjorn, N. K. Nielsen, and P. Olesen, Nucl. Phys. B **152**, 75 (1979); H. B. Nielsen and P. Olesen, Nucl. Phys. B **160**, 380 (1979).

Scaling Law for a Low-Pressure Gas Breakdown in a Homogeneous DC Electric Field

V. A. Lisovsky* and S. D. Yakovin**

*Kharkov State University, pl. Svobody 4, Kharkov, 310077 Ukraine

**Physics and Technology Center, National Academy of Sciences and Ministry of Education of Ukraine,
Kharkov, 310145 Ukraine

e-mail: lisovskiy@ff.univer.kipt.kharkov.ua

Received March 15, 2000; in final form, June 5, 2000

Gas breakdown in nitrogen, air, and oxygen in a dc electric field at various interelectrode distances L is studied experimentally. A scaling law for a low-pressure gas breakdown $U_{dc} = f(pL, L/R)$ is deduced. According to this scaling law, the breakdown voltage U_{dc} is a function not only of the product of the gas pressure p and the gap length L , but also of the ratio of the gap length L to the chamber radius R . It is shown that, for any dimensions of the cylindrical discharge chamber (in the range of L/R under investigation), the ratio of the breakdown electric field to the gas pressure p at the minimum of the ignition curve remains constant: $(E_{dc}/p)_{\min} \approx \text{const}$. A method for calculating the ignition curve in a cylindrical discharge chamber with arbitrary values of L and R is proposed. © 2000 MAIK "Nauka/Interperiodica".

PACS numbers: 51.50.+v; 52.80.Hc

As is known [1–7], the ignition curves of a glow discharge are described by the Paschen law $U_{dc} = f(pL)$; i.e., the breakdown voltage U_{dc} is a function of the product of the gas pressure p and the interelectrode distance L . The Paschen law implies that the ignition curves $U_{dc}(p)$ measured for various distances L must coincide if they are drawn as the function $U_{dc}(pL)$. However, the measurements of the ignition curves of a glow discharge in neon [8] showed that, with equal values of the product pL , the breakdown voltage for a long discharge gap with planar electrodes is significantly higher than that for a short gap. More recent studies [9–14] confirmed this conclusion for some other gases (neon, argon, nitrogen, hydrogen, etc.). In spite of a great number of experimental and theoretical papers devoted to low-pressure gas breakdown in a dc electric field, a method for calculating the ignition curve at arbitrary values of the interelectrode distance L and the radius of the discharge chamber R is still lacking.

This paper is devoted to the experimental study of a breakdown in nitrogen, air, and oxygen in a dc electric field in a discharge chamber with a variable interelectrode distance L . It is shown that, in the range of the ratio L/R under study, the ignition curves shift toward high values of the product pL and discharge voltage U_{dc} as the gap length L increases. In this case, for any values of the gap length L , the ratio of the breakdown electric field to the gas pressure $(E_{dc}/p)_{\min}$ at the minimum of the ignition curve remains constant. A generalized scaling law for the low-pressure gas breakdown $U_{dc} = f(pL, L/R)$ is deduced. A method allowing one to calculate the ignition curve for a glow discharge in a cylin-

dric chamber with arbitrary dimensions from the known ignition curve for a narrow discharge gap (for $L/R \rightarrow 0$), i.e., from the usual Paschen curve, is described.

We measured the ignition curves for a glow discharge in the range of dc voltages $U_{dc} \leq 1000$ V and pressures of $p \approx 10^{-2}$ –10 torr. A discharge tube with an inner diameter of 63 mm was used. The interelectrode distance L was varied in the range 0.5–10 cm; consequently, the studies were conducted in the range $L/R = 0.16$ –3.2. Planar parallel electrodes spanned the entire cross section of the discharge tube. Both the anode and the cathode were made from stainless steel. The breakdown voltage was measured accurate to ± 2 V. When determining the ignition voltage, the growth rate of the discharge voltage did not exceed 1 V/s. In all cases, our procedure for measuring the ignition curves was as follows. We fixed a certain distance L between the electrodes and then, for various gas pressures p , measured the breakdown voltage U_{dc} . Below, we explain why only this way of measuring the ignition curves of a glow discharge is correct.

Figure 1 shows the ignition curves measured by us in nitrogen for different distances L between the electrodes. It is seen from the figure that, as L increases, the ignition curves shift not only toward higher ignition voltages U_{dc} (as was obtained in [9–14]), but also toward higher values of pL . Apparently, such a shift of the ignition curves toward higher values of U_{dc} and pL with increasing interelectrode distance L may be attributed to an increase in losses of charged particles on the

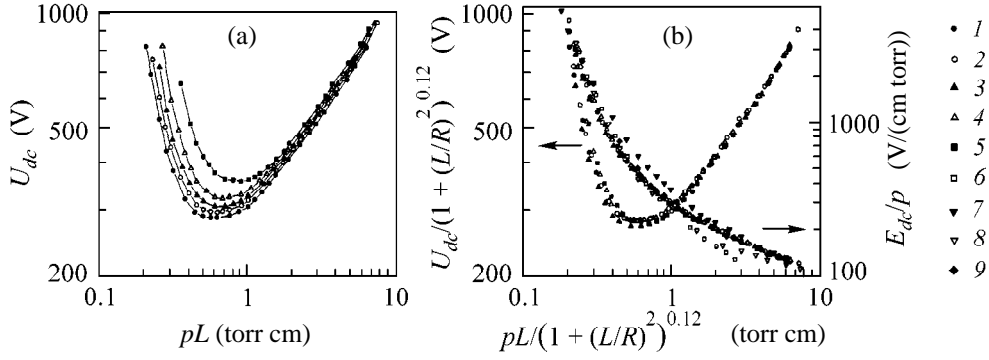


Fig. 1. (a) Experimental ignition curves of a glow discharge in nitrogen for the interelectrode distances $L = (1)$ 0.5, (2) 2, (3) 4, (4) 6, and (5) 8 cm. (b) Dependences of U_{dc}^* and E_{dc}/p on $(pL)^*$ obtained from curves (1)–(5) in Fig. 1a and the data from (6) [11], (7) [15], (8) [16], and (9) [18].

cylindrical wall of the discharge tube due to diffusion across the electric field.

Figure 2 shows the dependences of U_{\min} and $(E_{dc}/p)_{\min}$ on the value of $(pL)_{\min}$ obtained from our experimental ignition curves measured in a nitrogen discharge by varying the distance L . The solid line $U_{\min} = 407(pL)_{\min}$ and the dashed line $(E_{dc}/p)_{\min} = 407 \pm 5$ V/(cm torr) describe the results obtained fairly well. Hence, for any distance L between the electrodes, the ratio $(E_{dc}/p)_{\min}$ at the minimum of the ignition curve remains constant. This is also true if we change the value of the ion–electron emission coefficient γ of the cathode material (as was noted in [2, 3]).

Note that, by properly choosing the reference axes, we can make all of the obtained ignition curves almost coincide. For example, if we take

$$(pL)^* = pL/(1 + (L/R)^2)^a, \quad (1)$$

$$U_{dc}^* = U_{dc}/(1 + (L/R)^2)^a, \quad (2)$$

as the abscissa and ordinate, respectively, where $a \approx 0.12$ for nitrogen, then the ignition curves presented in Fig. 1a coincide accurate to ± 5 V (Fig. 1b). It is evident that, for $L/R \rightarrow 0$, we have the usual Paschen curve $U_{dc} = f(pL)$. It follows from Eqs. (1) and (2) that $U_{dc}^*/(pL)^* = U_{dc}/pL = E_{dc}/p$; i.e., the dependences $E_{dc}/p = f(pL)^*$ for different ignition curves must also coincide (which is seen in Fig. 1b). Here, we also see a reasonable agreement between our results and data from [11, 15–18]. For air, we have $a \approx 0.09$ (Fig. 3) and for hydrogen, we have $a \approx 0.03$ (Fig. 4). Note that, in Figs. 3 and 4, the dependences $E_{dc}/p = f(pL)^*$ obtained from experimental results [2, 9, 15, 16, 19] agree satisfactorily with our data. From our results, it follows that the scaling law for the gas breakdown can be written in the form $U_{dc} = f(pL, L/R)$ or $U_{dc}^* = f(pL)^*$.

Based on Eqs. (1) and (2) and the values of breakdown voltage given in the figures, we can calculate, to a high accuracy, the ignition curves for any cylindrical discharge chamber for arbitrary values of the distance

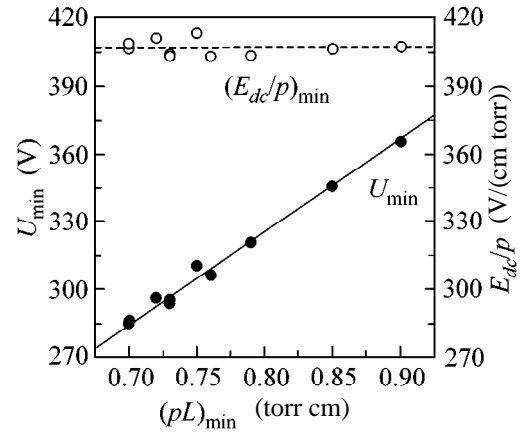


Fig. 2. Dependences of U_{\min} and $(E_{dc}/p)_{\min}$ on $(pL)_{\min}$ for nitrogen. The solid line corresponds to $U_{\min} = 407(pL)_{\min}$, and the dashed line corresponds to $(E_{dc}/p)_{\min} = 407$ V/(cm torr).

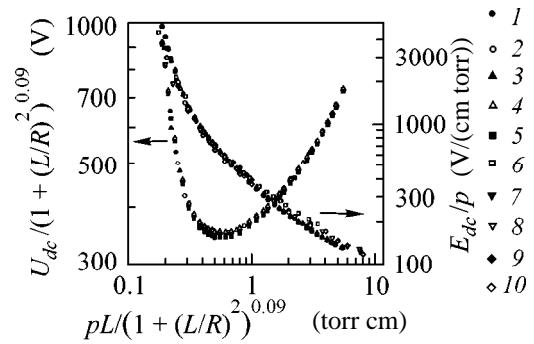


Fig. 3. Dependences of U_{dc}^* and E_{dc}/p on $(pL)^*$ for a glow discharge in air for the interelectrode distances $L = (1)$ 0.5, (2) 1, (3) 2, (4) 5, and (5) 10 cm and the data from (6) [15], (7) [19], (8) [16], and (9) [20], and (10) [21].

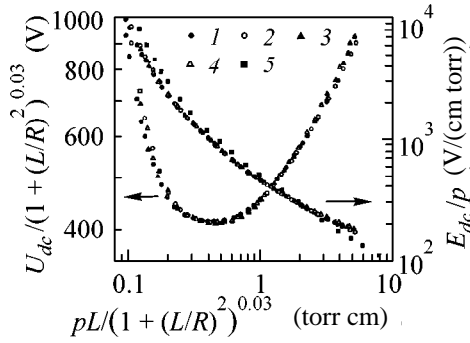


Fig. 4. Dependences of U_{dc}^* and E_{dc}/p on $(pL)^*$ for a glow discharge in oxygen for the interelectrode distances $L = (1) 0.5$, (2) 3, (3) 6, (4) 8 cm and (5) the data from [15].

L and radius R . As an example, we find the position of the minimum in the ignition curve for a nitrogen discharge for $R = 3.15$ cm, $L = 5$ cm, and a stainless-steel cathode. From Fig. 1b, it is seen that $U_{\min}^* \approx 280$ V and $(pL)_{\min}^* \approx 0.6$ torr cm. From (1) and (2), we obtain

$$(pL)_{\min} = (pL)_{\min}^* [1 + (L/R)^2]^{0.12}, \quad (3)$$

$$U_{\min} = U_{\min}^* [1 + (L/R)^2]^{0.12}. \quad (4)$$

For $L/R = 1.59$, we have $U_{\min} \approx 323$ V and $(pL)_{\min} \approx 0.7$ torr cm. From our experimental results, it follows that $U_{\min} \approx 320$ V and $(pL)_{\min} \approx 0.73$ torr cm; i.e., there is a good agreement between the coordinates of the maximum in the ignition curve obtained experimentally and those calculated using Eqs. (1)–(4). To calculate any other point on the ignition curve U_1^* and $(pL)_1^*$, we use the same procedure. In the general case, to calculate the ignition curve in a cylindrical discharge chamber with arbitrary dimensions, one should have the Paschen curve (i.e., the ignition curve measured in a discharge chamber such that $L/R \rightarrow 0$ and with the same cathode material). Then, from Eqs. (1) and (2), one can determine the values of U_{dc} and pL . If the initial ignition curve has been measured in a discharge chamber with L_0 and R_0 , such that the condition $L_0/R_0 \rightarrow 0$ does not hold, one should first calculate the dependence $U_{dc}^* = f(pL)^*$ using Eqs. (1) and (2) and then, from the same relations, calculate the ignition curve for a discharge chamber with the given dimensions L_1 and R_1 . This may be written more concisely in the following form:

$$(pL)_1 = pL_0 \left[\frac{1 + (L_1/R_1)^2}{1 + (L_0/R_0)^2} \right]^a, \quad (5)$$

$$U_{dc1} = U_{dc0} \left[\frac{1 + (L_1/R_1)^2}{1 + (L_0/R_0)^2} \right]^a, \quad (6)$$

where the index “1” stands for the ignition curve to be sought and the index “0” stands for the initially known ignition curve.

The ignition curve of a glow discharge is usually measured by two methods: (i) the distance L is fixed, and the breakdown voltage U_{dc} is measured at different values of the gas pressure p ; and (ii) the value of p is fixed, and the breakdown voltage U_{dc} is measured at different values of the distance L . However, the results obtained in this study show that the latter method of measuring the ignition curve (at a fixed value of p and variable L) is incorrect. The ignition curves obtained in this way are close to the Paschen curve only at small values of L but shift toward higher breakdown voltages with increasing L . Hence, the ignition curve of a glow discharge must be measured by varying the gas pressure p , the distance L between the electrodes being fixed.

In summary, the ignition of a glow discharge in nitrogen, air, and oxygen at a variable interelectrode distance L have been studied experimentally. It is shown that, at any interelectrode distance L , the ratio $(E_{dc}/p)_{\min}$ at the minimum of the ignition curve remains constant. In the range of L/R under study, the scaling law for gas breakdown $U_{dc} = f(pL, L/R)$ holds; i.e., the breakdown voltage U_{dc} is a function not only of the product of the gas pressure p and the gap length L , but also of the ratio L/R . A method for calculating the ignition curve in a cylindrical discharge chamber with arbitrary values of L and R is proposed.

REFERENCES

1. F. Paschen, Ann. Phys. Chem., Ser. 3 **37**, 69 (1889).
2. M. J. Druyvesteyn and F. M. Penning, Rev. Mod. Phys. **12**, 87 (1940).
3. J. M. Meek and J. D. Craggs, *Electrical Breakdown of Gases* (Clarendon, Oxford, 1953; Inostrannaya Literatura, Moscow, 1960).
4. Yu. P. Raizer, *Gas Discharge Physics* (Nauka, Moscow, 1987).
5. V. A. Lisovsky and V. D. Yegorenkov, J. Phys. D **27**, 2340 (1994).
6. A. V. Phelps and Z. Lj. Petrovic, Plasma Sources Sci. Technol. **8**, R21 (1999).
7. M. Sato, Bull. Yamagata Univ. **25**, 119 (1999).
8. J. S. Townsend and S. P. McCallum, Philos. Mag. **6**, 857 (1928).
9. H. Fricke, Z. Phys. **86**, 464 (1933).
10. S. P. McCallum and L. Klatzow, Philos. Mag. **17**, 279 (1934).
11. H. C. Miller, Physica (Amsterdam) **30**, 2059 (1964).

12. L. Jacques, W. Bruynooghe, R. Boucique, and W. Wieme, *J. Phys. D* **19**, 1731 (1986).
13. M. Yumoto, T. Sakai, Y. Ebinuma, *et al.*, in *Proceedings of the 8th International Symposium on High-Voltage Engineering, Yokohama, 1993*, p. 409.
14. G. Auday, P. Guillot, J. Galy, and H. Brunet, *J. Appl. Phys.* **83**, 5917 (1998).
15. M. J. Schonhuber, *IEEE Trans. Power Appar. Syst.* **88**, 100 (1969).
16. T. W. Dakin, J. Gerhold, Z. Krasucki, *et al.*, in *Proceedings of the International Conference on Large High-Voltage Electric Systems, Paris, 1977*, p. 1.
17. B. Held, N. Soulem, R. Peyrous, and N. Spyrou, *Trans. Inst. Electr. Eng. Jpn., Part A* **116**, 925 (1996).
18. B. Held, N. Soulem, R. Peyrous, and N. Spyrou, *J. Phys. III* **7**, 2059 (1997).
19. J. A. Pim, *Proc. Inst. Electr. Eng., Part 3* **96**, 117 (1949).
20. S. C. Brown, in *Basic Data of Plasma Physics* (Wiley, New York, 1959), p. 240.
21. H. Ritz, *Arch. Elektrotech. (Berlin)* **26**, 219 (1937).

Translated by N. Larionova

The Role of the Prepulse in Cluster Heating by a High-Power Femtosecond Laser Pulse

T. Auguste*, P. D'Oliveira*, S. Hulin*, P. Monet*, J. Abdallah, Jr.**, A. Ya. Faenov***, I. Yu. Skobelev***, A. I. Magunov***, and T. A. Pikuz***

*CEA, Centre D'Etudes de Saclay, DSM/DRECAM, Service des Photons Atomes et Molécules, 91191 Gif-sur-Yvette, France

**Los Alamos National Laboratory, P.P. Box 1663, Los Alamos, New Mexico 87545, USA

***VNIIFTRI Center for Multicharged Ion Spectrum Data, Mendeleev, 141570 Russia
***e-mail: skobelev@orc.ru

Received June 14, 2000

The interaction of a 60-fs laser pulse with argon clusters was experimentally studied. It is shown that cluster heating by an intense femtosecond pulse preceded by a picosecond prepulse can produce plasma whose ionization state is determined by the prepulse properties, while the mean energy of hot electrons is determined by the main pulse intensity. A simple model of cluster plasma evolution is suggested, allowing an adequate description of its X-ray emission. © 2000 MAIK "Nauka/Interperiodica".

PACS numbers: 52.50.Jm; 52.25.Nr; 32.30.Rj

1. In recent years, investigations into the interaction of high-power ultrashort (femtosecond) laser pulses with solid and gas targets have become particularly topical. On the one hand, these investigations provide information on the fundamental properties of a substance in extreme conditions and, on the other, they allow the use of new approaches to solving applied problems such as initiation of nuclear reactions, heavy particle acceleration, and the design of a luminous X-ray source for medicobiological and lithographic applications (see, e.g., [1–6]).

2. Evidently, the properties of plasma produced by an ultrashort laser pulse should primarily depend on the aggregate state of the target material. For example, the use of solid targets allows the production of a superdense hot (with a temperature of hundreds of electron volts) plasma whose ionization state is formed by virtue of electron–ion collisions. In the opposite case of gas targets, the temperature of the resulting relatively rarefied plasma is appreciably lower (tens of electron volts), while its ionization state is determined by the processes of multiphoton or tunnel ionization.

However, the original experiments with solid targets showed that there is one more very important parameter that determines the character of the interaction of ultrashort laser pulses with a substance, namely, the pulse contrast, i.e., the ratio of laser power in the maximum of the femtosecond pulse to the prepulse power. In particular, it turned out that a superdense plasma could be formed only if exceedingly high-contrast ($\sim 10^{10}$) pulses were used, when the heating prepulse radiation flux density was insufficient for producing preplasma, so that the energy of the main pulse was absorbed directly in the solid (see, e.g., [7–11]).

3. In recent years, a new type of cluster targets has appeared. They represent a gas containing clusters, i.e., large atomic or molecular conglomerates that are formed upon the flow of a cooled gas through a high-pressure nozzle. The cluster size L_{cl} and the number N_{cl} of particles in the cluster are determined both by the gas used and its parameters (temperature and density) and by the nozzle construction and can be as large as $L_{cl} \approx 100\text{--}1000 \text{ \AA}$ and $N_{cl} \approx 10^{4\text{--}6}$ atom/cluster, the particle density in the cluster being comparable with the solid-state density (see, e.g., reviews [1, 12]).

The character of the interaction of a femtosecond pulse with clusters depends on the pulse contrast to an even greater extent than in the case of a solid target. The situation becomes even more complicated, because the interaction is governed by another two highly important parameters, namely, the prepulse duration t_{prepulse} and the cluster size. Indeed, if the intensity of a femtosecond pulse is high enough (the typical experimental flux density is $q_{\text{las}} \approx 10^{17}\text{--}10^{18} \text{ W/cm}^2$), then the prepulse flux density is $10^{13}\text{--}10^{14} \text{ W/cm}^2$ even for a sufficiently high contrast of $10^4\text{--}10^5$ (typical values for femtosecond lasers), which is quite sufficient for cluster destruction and the production of a preplasma with electron temperature T_e of the order of 100–300 eV. The expansion of cluster plasma in time,

$$\tau_{\text{expansion}} \sim L_{cl}(m_i/Z_n k T_e)^{1/2} (10^{23}/N_{cr})^{1/3}, \quad (1)$$

(Z_n and m_i are the nuclear charge and the ion mass, respectively, and N_{cr} is the critical density for the heating laser) results in a decrease in the electron density

below its critical value [1]. This means that, if the prepulse duration satisfies the condition

$$\tau_{\text{prepulse}} \gg \tau_{\text{expansion}}, \quad (2)$$

then the main femtosecond pulse interacts not with clusters but with a rarefied plasma, so that the character of the interaction is, in fact, the same as in the heating of a gas target (weak absorption of laser radiation and the almost total absence of collisional ionization).

One can see from Eq. (1) that for the typical values $kT_e \sim 100$ eV, $N_{cr} \sim 10^{21}$ cm⁻³, and $L_{cl} \sim 100\text{--}1000$ Å the $\tau_{\text{expansion}}$ value is $\sim 1\text{--}10$ ps, so that, in the previous experiments [1] with a nanosecond prepulse, condition (2) was fulfilled with assurance. In this work, the opposite situation of a comparatively short prepulse $\tau_{\text{prepulse}} \leq \tau_{\text{expansion}}$ is experimentally studied for the case where the cluster preplasma formed after the prepulse contains dense areas efficiently absorbing the main pulse.

4. Experiments were carried out on a UHI10 setup (Saclay, France) consisting of a Ti : Sa laser with a wavelength of 800 nm and output of 10 TW. The laser beam was focused onto a cluster target with the use of an off-axis parabolic mirror; the beam diameter in the focal plane was ~ 25 μm. The duration of the main pulse was ~ 60 fs and its energy ~ 0.6 J, allowing the flux density on the target to be $\sim 10^{18}$ W/cm². The prepulse duration was ~ 1 ps. Since the contrast was $\sim 10^5$, the prepulse flux density was $\sim 10^{13}$ W/cm².

An argon cluster target was formed upon adiabatic free expansion through a high-pressure pulsed, conical nozzle (inlet and outlet diameters 1 and 8 mm, respectively, and length 20 mm).

Plasma diagnostics was performed by X-ray spectroscopy. Two X-ray spectrographs with spherically bent mica crystals were arranged in the FSPR-2D scheme [13–15] and tuned to the spectral ranges 3.9–4.2 Å and 3.35–3.45 Å, which include the He_α and He_β lines of the He-like Ar XVII ion. In some experiments, one of the spectrographs was tuned to the 3.72–3.82 Å range, which included the resonance Ly_α line of the H-like Ar XVIII ion, although this line was failed to be recorded.

5. An example of a spectrum in the range 3.9–4.2 Å is presented in Fig. 1. For comparison, analogous spectra obtained previously for an argon target heated by a nanosecond laser pulse [16] and on a plasma focus setup [17] are also shown in the same figure. It is clearly seen that the emission spectra of (b) the femtosecond laser plasma and (c) the plasma focus are quite similar and differ drastically from the emission spectrum of (a) a nanosecond laser plasma. The main distinctions are, first, that in cases (b) and (c) the lower multiplicity ions are present (Ar XV, XIV, XIII, ...) and, second, that the intensities of the Li-like Ar XVI satellites have different structures. Both distinctions can be easily explained if one assumes that the plasma ionized state corresponds to the electron temperature of the order of 100–200 eV, while the spectra are excited by the energetic (with energies $\sim 5\text{--}10$ keV) electrons. With the

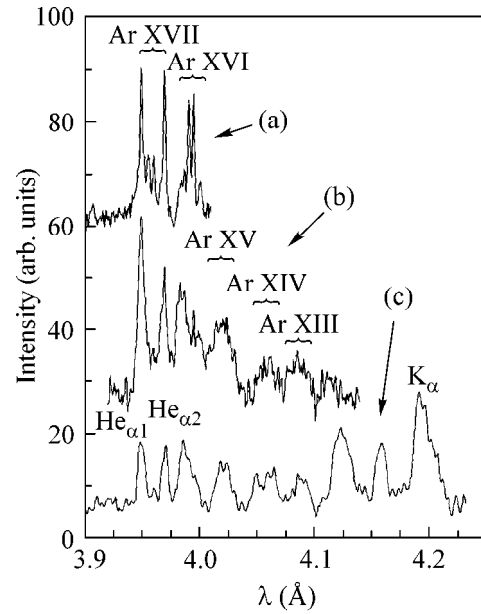


Fig. 1. Emission spectra of argon plasma produced on different plasma setups: (a) nanosecond laser plasma [16], (b) femtosecond laser plasma (this work), and (c) plasma focus [17].

plasma focus, where the plasma temperature is comparatively low and high-velocity electron beams are present, this assumption seems to be quite natural, and it was used in [17] to explain the experimental results. Below, we show that if the condition

$$\tau_{\text{prepulse}} \leq \tau_{\text{expansion}} \quad (3)$$

is fulfilled, then a similar situation may occur for the femtosecond cluster plasma as well.

6. Let us consider how the ionization state would form in the femtosecond laser cluster plasma in the presence of a sufficiently intense picosecond prepulse.

Inasmuch as, in our experiments, the heating radiation flux density in the prepulse was $\sim 10^{13}$ W/cm², one would expect cluster preheating up to temperatures T_{prepulse} of the order of 200 eV. The ionization processes in such a preplasma would proceed at a nearly solid-state electron density, and the ionization times for all argon ions containing $m \geq 3$ electrons would be longer than 1 ps [18]. This means that the He-, Li-, Be-, ... like argon ions would form in the preplasma during the prepulse, so that the ionization state would be nearly stationary with the electron temperature T_{prepulse} . Note that, since the ionization rate for the 1s shell at such temperatures is several orders of magnitudes lower than for the nl ($n > 1$) shells, the H-like Ar XVIII ions are not expected to form at the stage of heating by the prepulse.

By the time of the main pulse arrival, the heated clusters have time to expand slightly, but, if condition (3) is fulfilled, plasma areas with above-critical density are retained around each cluster. A femtosecond pulse with flux density $\sim 10^{18}$ W/cm² would be efficiently absorbed in these areas and, according to calcu-

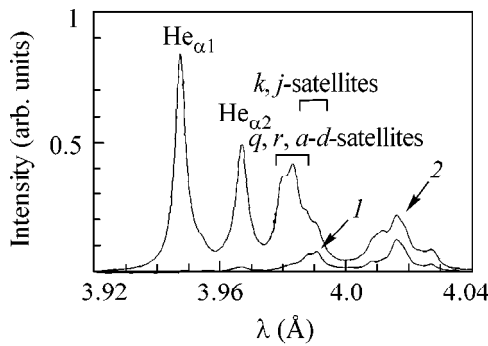


Fig. 2. Emission of argon plasma (1) before and (2) after arrival of the main femtosecond laser pulse.

lations [12, 19], would heat them up to the temperature T_{hot} of the order of several kiloelectron volts. Since, in this case, the plasma density is two orders of magnitude lower than the solid-state density, the collisional ionization times are of the order of hundreds of picoseconds, even with allowance made for a dramatic increase in the electron temperature. This implies that the main pulse would not strongly alter the plasma ionization state.

Thus, we are led to conclude that the combined action of the femtosecond pulse and the picosecond prepulse on the clusters would result in a plasma whose ionization state is determined by the prepulse flux density and corresponds to rather low electron temperatures $T_{\text{prepulse}} \sim 200$ eV and which would contain hot (kiloelectron-volt) electrons produced by the main pulse.

7. The above qualitative pattern of cluster heating dynamics and the equations of quasi-stationary radiation–collisional kinetics were used in this work to calculate plasma luminosity in the experimentally studied spectral ranges. All argon ions containing $m = 1-4$ electrons were taken into account and all electronic configurations with the principal quantum numbers $n < 6$

were considered, including the autoionizing states of the He-, Li-, and Be-like ions (a total of 1606 levels were included). Inasmuch as the thermalization time for the kiloelectron-volt electrons in a plasma with density $\leq 10^{21}$ cm $^{-3}$ is sizably longer than the plasma lifetime, they were considered as a monoenergetic beam with energy E_0 , which was set equal to 5 keV in the calculations. The computational results are presented in Figs. 2 and 3.

The plasma luminosity in the chosen spectral range is shown in Fig. 2 for two time intervals before the main pulse (curve 1) and after arrival of the main pulse (curve 2). One can see that the preplasma heating stage 1 makes a material contribution to the intensities of satellites due to the transitions from the autoionizing levels of comparatively weakly ionized Be-like Ar XV. For the Li-like Ar XVI transitions, this stage manifests itself only in the k, j satellites that are most strongly excited in the two-electron capture, while the He-like Ar XVII lines are mostly emitted after heating by the main pulse.

The calculated time-integrated luminosity is compared with the experimental spectrum in Fig. 3. One can see that our simple model of cluster plasma dynamics not only qualitatively, but also quantitatively, adequately describes the experimental results. A minor discrepancy between the experimental and theoretical spectra shown in Fig. 3a is caused by recording the He $_{\gamma}$ Ar XVII ($\lambda = 3.1996$ Å) line that corresponds to the other-order reflection from the mica crystal.

8. In summary, one can see that cluster heating by an intense femtosecond pulse preceded by a picosecond prepulse allows the production of plasma whose ionization state is governed by the prepulse properties, while the temperature (or, more precisely, the characteristic energy) of hot electrons is determined by the intensity of the main pulse. It follows that the extent of plasma nonstationarity can be rather simply controlled by changing the intensity ratio for the pulse and prepulse.

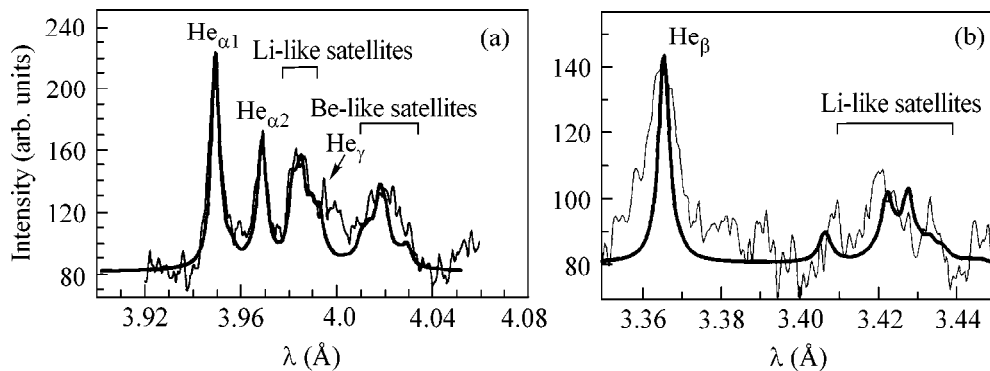


Fig. 3. Comparison of the emission spectra of the femtosecond argon cluster plasma with the model calculations for the spectral regions including Ar XVII (a) He $_{\alpha}$ and (b) He $_{\beta}$ lines. The theoretical spectra are calculated for $N_e = 10^{21}$ cm $^{-3}$, $T_{\text{preplasma}} = 190$ eV, and $E_0 = 5$ keV.

Such a plasma is of special interest primarily for the problems of atomic spectroscopy, because it provides a possibility of investigating the ion levels that are effectively populated in the collisional excitation or inner-shell ionization of many-electron, multiply charged ions. At the same time, plasma with such properties may find some practical use, e.g., in the problem of designing X-ray lasers on the Ne- and Ni-like ion transitions, because in this case the optimum conditions for achieving large population inversions are naturally realized (see, e.g., [20–23]).

This work was supported in part by the INTAS, grant no. 97-2090.

REFERENCES

1. T. Ditmire, T. Donnelly, A. M. Rubenchik, *et al.*, Phys. Rev. A **53**, 3379 (1996).
2. P. Gibbon and E. Forster, Plasma Phys. Controlled Fusion **38**, 769 (1996).
3. T. Ditmire, J. Zwelback, V. P. Yanovsky, *et al.*, Nature (London) **398**, 490 (1999).
4. J. Zwelback, R. A. Smith, T. E. Cowan, *et al.*, Phys. Rev. Lett. **84**, 2634 (2000).
5. S. Dobosz, M. Schmidt, M. Perdrix, *et al.*, Pis'ma Zh. Éksp. Teor. Fiz. **68**, 454 (1998) [JETP Lett. **68**, 485 (1998)].
6. S. Dobosz, M. Schmidt, M. Perdrix, *et al.*, Zh. Éksp. Teor. Fiz. **115**, 2051 (1999) [JETP **88**, 1122 (1999)].
7. A. Ya. Faenov, J. Abdallah, Jr., R. E. H. Clark, *et al.*, Proc. SPIE **3157**, 10 (1997).
8. A. M. Urnov, J. Dubau, A. Ya. Faenov, *et al.*, Pis'ma Zh. Éksp. Teor. Fiz. **67**, 500 (1998) [JETP Lett. **67**, 489 (1998)].
9. A. Ya. Faenov, A. I. Magunov, T. A. Pikuz, *et al.*, Phys. Scr. T **80**, 536 (1999).
10. A. Maksimchuk, M. Nantel, G. Ma, *et al.*, J. Quant. Spectrosc. Radiat. Transfer **65**, 367 (2000).
11. F. B. Rosmej, U. N. Funk, M. Gessel, *et al.*, J. Quant. Spectrosc. Radiat. Transfer **65**, 477 (2000).
12. R. A. Smith, J. W. G. Tisch, T. Ditmire, *et al.*, Phys. Scr. T **80**, 35 (1999).
13. I. Yu. Skobelev, A. Ya. Faenov, B. A. Bryunetkin, *et al.*, Zh. Éksp. Teor. Fiz. **108**, 1263 (1995) [JETP **81**, 692 (1995)].
14. T. A. Pikuz, A. Ya. Faenov, S. A. Pikuz, *et al.*, J. X-Ray Sci. Technol. **5**, 323 (1995).
15. B. K. F. Young, A. L. Osterheld, D. F. Price, *et al.*, Rev. Sci. Instrum. **69**, 4049 (1998).
16. V. M. Dyakin, I. Yu. Skobelev, A. Ya. Faenov, *et al.*, Kvantovaya Élektron. (Moscow) **24**, 709 (1997).
17. J. Abdallah, Jr., R. E. H. Clark, A. Ya. Faenov, *et al.*, J. Quant. Spectrosc. Radiat. Transfer **62**, 85 (1999).
18. L. A. Vaĩnshteĩn, I. I. Sobelman, and E. A. Yukov, *Atomic Excitation and Spectral Line Broadening* (Nauka, Moscow, 1979; Springer-Verlag, Berlin, 1981).
19. T. Ditmire, P. K. Patel, R. A. Smith, *et al.*, J. Phys. B **31**, 2825 (1998).
20. P. V. Nickles, V. N. Shlyaptsev, M. Kalachnikov, *et al.*, Phys. Rev. Lett. **78**, 2748 (1997).
21. J. Dunn, A. L. Osterheld, V. N. Shlyaptsev, *et al.*, in *Proceedings of the Eleventh APS Topical Conference on Atomic Processes in Plasmas*, Ed. by E. Oks and M. S. Pindzola (American Institute of Physics, 1998), CP443, p. 106.
22. J. Dunn, A. L. Osterheld, V. N. Shlyaptsev, *et al.*, in *Proceedings of the 6th International Conference on X-ray Lasers, Kyoto*, Ed. by Y. Kato, H. Takuma, and H. Daido, Inst. Phys. Conf. Ser., No. 159, 51 (1998).
23. J. Dunn, A. L. Osterheld, R. Shepherd, *et al.*, Phys. Rev. Lett. **80**, 2825 (1998).

Translated by V. Sakun

Some Estimates for Magnetic Fluctuations in a Turbulent Medium

N. A. Silant'ev

Instituto Nacional de Astrofísica, Óptica y Electrónica, 72000 Puebla, México

Pulkovo Observatory, Russian Academy of Sciences, Pulkovskoe shosse 65, St. Petersburg, 196140 Russia
e-mail: silant@inaoep.mx

Received May 10, 2000; in final form, June 19, 2000

A new integral relationship between the fluctuations $\mathbf{b}(\mathbf{r}, t)$ of a magnetic field and its mean $\mathbf{B}_0(\mathbf{r}, t)$ is derived for the steady-state magnetic field in a turbulent medium. This formula provides the estimate $\langle \mathbf{b} \cdot \text{curl} \mathbf{b} \rangle = -\mathbf{B}_0 \cdot \text{curl} \mathbf{B}_0$. Simultaneously, the coefficient of amplification of the mean magnetic field (α effect) is obtained: $\alpha = (\eta + \beta) \mathbf{B}_0 \cdot \text{curl} \mathbf{B}_0 / B_0^2$. The formula for α allows for a decrease in this coefficient owing to the back action of the magnetic field on the turbulent velocity field. It is shown that the Zel'dovich's estimate $\langle b^2 \rangle \approx \beta / \eta B_0^2$ for two-dimensional turbulence holds for magnetic fields at the instant the fluctuations $\langle a^2 \rangle$ of the vector potential, rather than $\langle b^2 \rangle$, reach a maximum. Here, η and β are the ohmic (molecular) and turbulent diffusion coefficients, respectively. This estimate is refined with allowance made for the fact that the condition for diffusion approximation itself relates the β , b , and B_0 quantities to each other. © 2000 MAIK "Nauka/Interperiodica".

PACS numbers: 47.65.+a; 91.25.Cw

Because of the complexity of a joint analysis of the Navier–Stokes equation and the induction equation for the magnetic field

$$\frac{\partial \mathbf{B}}{\partial t} = \text{curl} \mathbf{U}_0 \times \mathbf{B} + \text{curl} \mathbf{u} \times \mathbf{B} + \eta \nabla^2 \mathbf{B}, \quad (1)$$

estimates of the mean field $\langle \mathbf{B} \rangle \equiv \mathbf{B}_0$ and magnetic fluctuations $\langle \mathbf{b}^2 \rangle$ in various limiting cases are of great importance. In Eq. (1), \mathbf{U}_0 and \mathbf{u} stand for the regular and stochastic (turbulent) parts of the Eulerian velocity in a conducting medium, respectively. The magnetic field \mathbf{B} and the vector potential \mathbf{A} can be represented as the sums of their mean and fluctuating parts: $\mathbf{B} = \mathbf{B}_0 + \mathbf{b}$ and $\mathbf{A} = \mathbf{A}_0 + \mathbf{a}$, with $\langle \mathbf{b} \rangle = 0$ and $\langle \mathbf{a} \rangle = 0$.

Zel'dovich's paper [1] was among the first works of this kind where it was shown that a magnetic dynamo cannot occur for a two-dimensional flow of a conducting liquid. Zel'dovich also showed that, by the time $t_d \approx L_0^2 / \beta$, the initial magnetic field $\mathbf{B}_0(\mathbf{r}, 0)$ transforms into a purely fluctuating field $\mathbf{b}(\mathbf{r}, t)$ with mean-square amplitude $\langle b^2(\mathbf{r}, t_d) \rangle \approx R_m B_0^2(\mathbf{r}, 0)$. In these expressions, L_0 is the length scale of the initial potential $\mathbf{A}_0(\mathbf{B}_0(\mathbf{r}, 0) = \text{curl} \mathbf{A}_0)$. According to Zel'dovich, the fluctuations also eventually disappear in the characteristic time $\sim t_d$.

In interplanetary space, the magnetic Reynolds number $R_m \approx \beta / \eta \approx u_0 R_0 / \eta$ is enormously large: $R_m \sim$

10^9 – 10^{14} (u_0 and R_0 are the characteristic velocity and the scale of turbulent motions, respectively). Zel'dovich's estimate $\langle b^2 \rangle \approx R_m B_0^2$ also came into use for real three-dimensional turbulence [2–4] to give the $\alpha \approx u_0 / R_m$ estimate. It is known [5, 6] that in order to explain the generation of cosmic magnetic fields it is necessary that $\alpha \approx u_0$. Therefore, the estimate $\alpha \approx u_0 / R_m$ fully rules out the conventional mechanism of magnetic amplification (α effect).

It is shown below that the estimate for the 3D turbulence has a different form, namely, $\alpha = (\eta + \beta) \mathbf{B}_0 \cdot \text{curl} \mathbf{B}_0 / B_0^2 \sim u_0$. High estimates for the fluctuations imply that the back action of the magnetic field on the turbulence is determined by the energy of the fluctuations, rather than by the mean-field energy [3].

To derive new estimates and refine the meaning of Zel'dovich's estimate, the method suggested in [7] is used in this work for an analysis of the pairs of coupled equations for the $\mathbf{A}_0 \cdot \mathbf{B}_0$ and $\langle \mathbf{a} \cdot \mathbf{b} \rangle$, \mathbf{A}_0^2 and $\langle \mathbf{a}^2 \rangle$, and \mathbf{B}_0^2 and $\langle \mathbf{b}^2 \rangle$ quantities. With these systems of equations, the fluctuation rise dynamics can be traced more clearly than by considering the means $\langle \mathbf{A} \cdot \mathbf{B} \rangle$, $\langle \mathbf{A}^2 \rangle$, and $\langle \mathbf{B}^2 \rangle$. Following Zel'dovich, the analysis will be carried out for the volume-integrated quantities, so that the flux terms containing divergences disappear owing to the divergence theorem.

Analysis of the main equations. Seehafer [7] has derived a system of two exact equations for the evolution of magnetic helicity $\langle \mathbf{A} \cdot \mathbf{B} \rangle = \mathbf{A}_0 \cdot \mathbf{B}_0 + \langle \mathbf{a} \cdot \mathbf{b} \rangle$:

$$\frac{\partial \mathbf{A}_0 \cdot \mathbf{B}_0}{\partial t} \quad (2)$$

$$= -2\eta \mathbf{B}_0 \cdot \text{curl} \mathbf{B}_0 + 2\mathbf{B}_0 \cdot \mathbf{F}_0 - \text{div}(c\mathbf{E}_0 \times \mathbf{A}_0),$$

$$\frac{\partial \langle \mathbf{a} \cdot \mathbf{b} \rangle}{\partial t} \quad (3)$$

$$= -2\eta \langle \mathbf{b} \cdot \text{curl} \mathbf{b} \rangle - 2\mathbf{B}_0 \cdot \mathbf{F}_0 - \text{div}(c \langle \mathbf{e} \times \mathbf{a} \rangle).$$

Here, $\mathbf{E} = \mathbf{E}_0 + \mathbf{e}$, $\langle \mathbf{e} \rangle = 0$ is the electric field strength and c is the speed of light. One has from [8]

$$c\mathbf{E}(\mathbf{r}, t) = \eta \text{curl} \mathbf{B} - \mathbf{u} \times \mathbf{B} - \mathbf{U}_0 \times \mathbf{B}. \quad (4)$$

The electromotive force is $\mathbf{F} = \mathbf{F}_0 + \mathbf{f} = \mathbf{u} \times \mathbf{B} + \mathbf{U}_0 \times \mathbf{B}$. Its mean is $\mathbf{F}_0 = \langle \mathbf{u} \times \mathbf{b} \rangle + \mathbf{U}_0 \times \mathbf{B}_0$. In the diffusion approximation [9, 10], one usually sets

$$\langle \mathbf{u} \times \mathbf{b} \rangle \equiv \alpha(\mathbf{r}, t) \mathbf{B}_0(\mathbf{r}, t) - \beta(\mathbf{r}, t) \text{curl} \mathbf{B}_0(\mathbf{r}, t), \quad (5)$$

where the α coefficient describes the amplification of the mean magnetic field and β is the turbulent diffusion coefficient. It is assumed in the magnetic dynamo theories [5, 6, 9, 10] that $\alpha \approx u_0$ and $\beta \approx u_0 R_0$. The coefficient α is zero for a mirror-symmetric turbulence, where the velocity helicity $\langle \mathbf{u} \cdot \text{curl} \mathbf{u} \rangle = 0$. For 2D turbulence, $\mathbf{A} \cdot \mathbf{B} \equiv 0$ and $\alpha \equiv 0$. It is seen from Eqs. (2) and (3) that the α effect (more precisely, the term with \mathbf{F}_0) enhances (or reduces) the large-scale magnetic helicity and reduces (or enhances) to the same extent its small-scale fluctuating part. This statement is the main conclusion of [7]. It is worth noting that both Eqs. (2) and (3) should be equally taken into account when considering the influence of the α effect on the evolution of magnetic fluctuations. However, it is more suitable to use Eq. (4) and the Maxwell equation $\partial \mathbf{B}_0 / \partial t = -c \text{curl} \mathbf{E}_0$ instead of Eq. (2).

Let us consider a steady-state magnetic field in a medium. In this case, $\partial \langle \mathbf{a} \cdot \mathbf{b} \rangle / \partial t = 0$ and $\mathbf{B}_0(\mathbf{r}, t) = \mathbf{B}_0(\mathbf{r})$ and, hence, $c \text{curl} \mathbf{E}_0 = -\partial \mathbf{B}_0 / \partial t = 0$; i.e., $c\mathbf{E}_0 = \nabla \phi_0(\mathbf{r})$. Averaging Eq. (4) gives

$$\mathbf{F}_0 = \eta \text{curl} \mathbf{B}_0(\mathbf{r}) - \nabla \phi_0(\mathbf{r}). \quad (6)$$

Substituting Eq. (6) in Eq. (3) and volume integration yields the exact relationship

$$\int dV [\langle \mathbf{b} \cdot \text{curl} \mathbf{b} \rangle + \mathbf{B}_0 \cdot \text{curl} \mathbf{B}_0] = 0. \quad (7)$$

The term with the potential $\mathbf{B}_0 \nabla \phi_0 = \text{div}(\mathbf{B}_0 \phi_0)$ disappears after applying the divergence theorem. Therefore, the exact Eq. (7) gives the estimate

$$\langle \mathbf{b} \cdot \text{curl} \mathbf{b} \rangle \approx -\mathbf{B}_0 \cdot \text{curl} \mathbf{B}_0 \quad (8)$$

or

$$\langle b^2(\mathbf{r}) \rangle \approx l_0 / L_0 B_0^2(\mathbf{r}). \quad (9)$$

Here, l_0 is the scale of magnetic fluctuations and L_0 is the scale of the mean magnetic field $\mathbf{B}_0(\mathbf{r})$. Clearly, $l_0 < L_0$ and the energy of magnetic fluctuations is lower than the energy of the mean magnetic field.

The stationary state of a conducting liquid and a steady-state magnetic field can be determined by matching the above components, i.e., with allowance made for the back action of the magnetic field on the turbulence. Therefore, Eq. (7) allows for this back reaction, although it is derived without using the Navier–Stokes equation. The exact integral relationship (7) may be used as an additional criterion for the correctness of numerical computations of the evolution of a magnetic field on its way to the stationary state.

In the diffusion approximation (5), the exact Eq. (6) takes the form

$$\alpha(\mathbf{r}) B_0^2 = (\eta + \beta) \mathbf{B}_0 \cdot \text{curl} \mathbf{B}_0 - \text{div} \mathbf{B}_0 \phi_0(\mathbf{r}). \quad (10)$$

Making use of the well-known [11] expression for a curl-free field through its divergence, the following explicit formula can be written from Eq. (4) for $\phi_0(\mathbf{r})$:

$$\phi_0(\mathbf{r}) = \text{div} \int dV' [\langle \mathbf{u} \times \mathbf{b} \rangle + \mathbf{U}_0 \times \mathbf{B}_0] |\mathbf{r} - \mathbf{r}'|^{-1} / 4\pi. \quad (11)$$

This expression is purely formal, because the integrand contains unknown functions. The diffusion approximation (5) implies that $\mathbf{B}_0(\mathbf{r})$ and $\mathbf{U}_0(\mathbf{r})$ are smooth on the turbulence scale, $\sim R_0$. In this case, the term $\text{div} \mathbf{B}_0(\mathbf{r}) \phi_0(\mathbf{r})$ containing double differentiation of a smooth function is smaller than the first term in Eq. (10). This yields the following estimate:

$$\alpha(\mathbf{r}) \approx (\eta + \beta(\mathbf{r})) \mathbf{B}_0 \cdot \text{curl} \mathbf{B}_0 / B_0^2. \quad (12)$$

In the stationary state, the magnetic amplification caused by the turbulent motion of a conducting liquid or gas should be in exact balance with the field weakening through ohmic dissipation. This balance cannot be properly described in the diffusion approximation (5). Because of this, the substitution of $\mathbf{B}_0 \cdot \mathbf{F}_0$ does not lead to the exact Eq. (7) in this approximation; instead, it gives

$$\int dV [\eta \langle \mathbf{b} \cdot \text{curl} \mathbf{b} \rangle - \beta(\mathbf{r}) \mathbf{B}_0 \cdot \text{curl} \mathbf{B}_0 + \alpha(\mathbf{r}) B_0^2] = 0. \quad (13)$$

Interestingly, this formula also leads to estimate (12), provided that the exact relationship (7) is used.

The steady-state condition (6) plays a crucial role in obtaining estimates (7)–(9). Insofar as the term with the potential disappears upon integration, this condition implies that it is ohmic dissipation which determines the relative fluctuation level in the stationary state. In what follows, the amplitude of nonstationary fluctuations will be estimated for the instant t_b or t_a when $\langle b^2 \rangle$ or $\langle a^2 \rangle$, respectively, reaches its maximum value. For these instants of time, condition (6) is not fulfilled, and most likely it is the turbulent motions which determine the fluctuation level, provided that the times t_b and t_a are

shorter than the characteristic time for establishing the stationary state. Evidently, the estimates for these three characteristic times depend on the particular type of turbulence. Since the stationary fluctuations (9) are small, these estimates can be considered as upper bounds on the fluctuations at times t_b and t_a .

The Seehafer-type equation for magnetic helicity can be written directly for the B_0^2 and $\langle b^2 \rangle$ quantities:

$$\frac{\partial B_0^2}{\partial t} = 2\alpha \mathbf{B}_0 \cdot \text{curl} \mathbf{B}_0 - 2(\eta + \beta)(\nabla_i B_{0j})^2 + (\eta + \beta)\nabla^2 B_0^2, \quad (14)$$

$$\frac{\partial \langle b^2 \rangle}{\partial t} = -2\alpha \mathbf{B}_0 \cdot \text{curl} \mathbf{B}_0 - 2\eta \langle (\nabla_i b_j)^2 \rangle + 2\beta(\nabla_i B_{0j})^2 + \gamma B_0^2 + 2\langle \mathbf{b} \cdot \text{curl}(\mathbf{u} \times \mathbf{b}) \rangle + \eta \nabla^2 \langle b^2 \rangle. \quad (15)$$

These equations are written in the diffusion approximation, where they pictorially demonstrate the energy evolution for both the mean magnetic field and magnetic fluctuations. The new coefficient γ is of the order of $\approx \beta/R_0^2$. The terms with ∇^2 disappear upon volume integration, and they will be ignored in the subsequent estimates. First and foremost, these equations suggest that the α effect enhances the large-scale magnetic field and reduces the fluctuations. In the stationary state, the balance between the enhancement of the large-scale part and its weakening is mainly provided by the self-consistency of the coefficients α and β : $\alpha \sim \beta/L_0$. The same estimate follows from Eq. (12).

To estimate the mean-square fluctuation $\langle b^2 \rangle$ at the instant t_b reaches its possible maximum, it is most profitable to use the exact nondiffusional form of Eq. (15). The corresponding estimate of the expression $-2\eta \langle (\nabla_i b_j)^2 \rangle + 2\langle (\mathbf{u} \times \mathbf{B}_0) \cdot \text{curl} \mathbf{b} \rangle + 2\langle (\mathbf{u} \times \mathbf{b}) \cdot \text{curl} \mathbf{b} \rangle = 0$ shows that the balance between the enhancement and weakening of the magnetic field is achieved in two steps. The main balance is fulfilled at the level of adjusting the turbulent motions without inclusion of the ohmic dissipation. This yields $\langle b^2 \rangle \sim B_0^2$. The remaining disbalance of the order of $\eta/u_0 l_0$ of the main energy level is eliminated by the ohmic diffusion. The $\langle b^2 \rangle \sim B_0^2$ estimate also persists for the maximum value $\eta/u_0 l_0 \sim 1$ as well. Note that this estimate is valid for the two-dimensional turbulence as well.

Two-dimensional turbulence. The equations for A_0^2 and $\langle a^2 \rangle$ in a 2D turbulence considered by Zel'dovich in [1] have the form

$$\frac{\partial A_0^2}{\partial t} = -2\eta B_0^2 + 2A_0 F_0 + \eta \nabla^2 A_0^2, \quad (16)$$

$$\frac{\partial \langle a^2 \rangle}{\partial t} = -2\eta \langle b^2 \rangle - 2A_0 F_0 + \eta \nabla^2 \langle a^2 \rangle - \text{div} \langle \mathbf{u}(2A_0 a + a^2) \rangle. \quad (17)$$

In these equations, the vector potential $\mathbf{A} = \mathbf{e}_z[A_0(x, y, t) + a(x, y, t)]$, while the magnetic field and the turbulent velocity are perpendicular to the z axis with unit vector \mathbf{e}_z . All quantities depend only on the coordinates x, y and the time t . The electromotive force is directed along the z axis and equals $F_0 = -\text{div} \langle \mathbf{u} \mathbf{a} \rangle$. In the diffusion approximation, $F_0 \equiv \beta \nabla^2 A_0$.

Zel'dovich considered only one volume-integrated equation for the $\langle A^2 \rangle = A_0^2 + \langle a^2 \rangle$ quantity:

$$\frac{d}{dt} \int dV [A_0^2 + \langle a^2 \rangle] = -2\eta \int dV [B_0^2 + \langle b^2 \rangle]. \quad (18)$$

He neglected the term with $\langle a^2 \rangle$ on the left-hand side and the B_0^2 term on the right-hand side and set $dA_0^2/dt \sim bA_0^2/L_0^2 \sim \beta B_0^2$ to arrive at the estimate $\langle b^2 \rangle_{\text{max}} \sim \beta/\eta B_0^2$. By B_0 was meant the initial magnetic field.

Apart from the terms with ∇^2 and div disappearing after volume integration, the system of Eqs. (16) and (17) has a clear physical meaning. The square of the mean potential monotonically decreases with the characteristic time $t_d \sim L_0^2/\beta$ of turbulent mixing. The mean-square fluctuation $\langle a^2 \rangle$ of the potential increases from the initial zero value with the same characteristic time t_d , reaches its maximum value $\langle a^2 \rangle_{\text{max}}$, and then tends to zero with the characteristic time $t_\eta \sim l_0^2/\eta$. The system eventually reaches the stationary state, for which both the mean magnetic field and its fluctuations disappear, in accordance with the Zel'dovich dynamo-suppression theorem.

At the instant t_a , when $\langle a^2 \rangle$ reaches its maximum, the derivative $\partial \langle a^2 \rangle / \partial t = 0$, and the following estimate holds in the diffusion approximation:

$$\langle b^2(t_a) \rangle \approx \beta/\eta B_0^2(t_a) = R_m B_0^2(t_a). \quad (19)$$

This estimate relates the magnetic fluctuations $\langle b^2 \rangle$ to the mean (not the initial!) magnetic field at the instant of time when the potential fluctuations reach a maximum. Therein lies the refinement of Zel'dovich's estimate. The time corresponding to the maximum of $\langle b^2 \rangle$ fluctuations does not coincide with the time corresponding to the maximum of potential fluctuations $\langle a^2 \rangle$. The l_0 scale strongly depends on the turbulence structure and, hence, estimate (19) can apply to the situation $t_a \gg t_d$ for which the mean field $B_0(t_a)$ is so small that the fluctuation level $\langle b^2 \rangle$ may be lower than the initial magnetic field.

Nevertheless, estimate (19) is invalid, because the diffusion approximation $F_0 = -\text{div} \langle \mathbf{u} \mathbf{a} \rangle \equiv \beta \nabla^2 A_0$ itself

implies the relationship $\beta \approx u_0 l_0 b / B_0$. Substitution of this β value into Eq. (19) gives the final estimate:

$$\langle b^2(t_a) \rangle \approx (u_0 l_0 / \eta)^2 B_0^2(t_a). \quad (20)$$

This estimate also directly follows from the exact Eq. (17) without recourse to the β value. According to Eq. (20), one has $b(t_a) \approx B_0(t_a)$ for the Kolmogorov-type spectra with $u_0 l_0 \approx \eta$. For the spectra with $l_0 \sim R_0$, the fluctuation decay time $t_a \gg t_d$. In this time, B_0 virtually disappears, so that the relative fluctuation level becomes very high. This example demonstrates that it is more convenient to make estimates by using, from the outset, the exact equations, as was done in the 3D case.

As was already pointed out, the diffusion approximation cannot be used in determining the stationary state. In the 2D case considered, $\text{div} \mathbf{E}_0 \equiv 0$ and the steady-state condition $\text{curl} \mathbf{E}_0 = 0$ means that $\mathbf{E}_0 = 0$; i.e., $F_0 = -\eta \nabla^2 A_0$. Substitution of this expression into Eq. (17) and volume integration gives

$$\int dV (B_0^2 + \langle b^2 \rangle) = 0. \quad (21)$$

This means that $\mathbf{B}_0 = 0$ and $\mathbf{b} = 0$, as one would expect according to the Zel'dovich dynamo-suppression theorem. The derivation of Eq. (21) is a somewhat alternative proof of this theorem.

To summarize, the estimates made in this work for the stationary 3D case and for a possible $\langle b^2 \rangle$ maximum before reaching the stationary state indicate that the magnetic fluctuations are smaller than, or of the same order as, the energy of the mean magnetic field. This signifies that the amplification coefficient α can be large enough, $\sim u_0$, for the magnetic dynamo to be realized in interplanetary space.

The estimate $\langle \mathbf{b} \cdot \text{curl} \mathbf{b} \rangle \approx -\mathbf{B}_0 \cdot \text{curl} \mathbf{B}_0$ obtained in this work strongly reduces the estimate for a decrease in the α coefficient owing to the back action of the magnetic field on the turbulence, compared to the results of [4]. In that work, an approximate analytical theory was suggested for this effect. The authors did not take into account the steady-state condition (6) and used the diffusion approximation (5) in the case $\mathbf{B}_0 = \text{const}$ to obtain from Eq. (13) the relationship $\langle \mathbf{b} \cdot \text{curl} \mathbf{b} \rangle = -\alpha B_0^2 / \eta$ for the stationary state. They also used the approximate linearized relationship $\alpha = -\tau_0 \langle \mathbf{u} \cdot \text{curl} \mathbf{u} \rangle / 3 + \tau_0 \langle \mathbf{b} \cdot \text{curl} \mathbf{b} \rangle / 12\pi\rho$ to obtain

$$\alpha = \frac{\alpha_0}{1 + \tau_0 R_m B_0^2 / 12\pi\rho\beta}, \quad (22)$$

where $\alpha_0 = -\tau_0 \langle \mathbf{u} \cdot \text{curl} \mathbf{u} \rangle / 3$, ρ is the density of a liquid or gas, and τ_0 is the characteristic time of turbulent

velocities. It follows from above that the steady-state condition (6) should necessarily be taken into account when considering the stationary case. That is why Eq. (22) is invalid. However, if the steady-state condition, i.e., the relationship $\langle \mathbf{b} \cdot \text{curl} \mathbf{b} \rangle = -\alpha B_0^2 / (\eta + \beta)$ had been taken into account in [4], then the enormous Reynolds number R_m would not have appeared in Eq. (22). Thus, the decrease in α is, in fact, small; it is only halved if the magnetic and kinetic energies are equal to one another. This fact is in qualitative agreement with the results of numerical computations [12]. However, it should be pointed out that Eq. (22) was derived using the Navier–Stokes and magnetic induction equations linearized in \mathbf{u} and \mathbf{b} ; i.e., it applies only to relatively weak fluctuations. The estimates obtained for the fluctuations in this work, to some extent, justify this approach.

REFERENCES

1. Ya. B. Zel'dovich, Zh. Éksp. Teor. Fiz. **31**, 154 (1956) [Sov. Phys. JETP **4**, 460 (1956)].
2. S. I. Vainshtein and R. Rosner, Astrophys. J. **376**, 199 (1991).
3. S. I. Vainshtein and F. Cattaneo, Astrophys. J. **393**, 165 (1992).
4. A. V. Gruzinov and P. H. Diamond, Phys. Rev. Lett. **72**, 1651 (1994).
5. Ya. B. Zel'dovich and A. A. Ruzmaïkin, Usp. Fiz. Nauk **152**, 263 (1987) [Sov. Phys. Usp. **30**, 494 (1987)].
6. N. O. Weiss, in *Lectures on Solar and Planetary Dynamos*, Ed. by M. R. E. Proctor and A. D. Gilbert (Cambridge Univ. Press, Cambridge, 1994).
7. N. Seehafer, Phys. Rev. E **53**, 1283 (1996).
8. L. D. Landau and E. M. Lifshitz, *Course of Theoretical Physics*, Vol. 8: *Electrodynamics of Continuous Media* (Nauka, Moscow, 1992; Pergamon, New York, 1984).
9. F. Krause and K.-H. Rädler, *Mean-Field Magnetohydrodynamics and Dynamo Theory* (Pergamon, Oxford, 1980).
10. H. K. Moffatt, *Magnetic Field Generation in Electrically Conducting Fluids* (Cambridge Univ. Press, Cambridge, 1978; Mir, Moscow, 1980).
11. N. E. Kochin, *Fundamentals of Vector Analysis and Principles of Tensor Calculus* (Nauka, Moscow, 1961).
12. L. L. Kichatinov, V. V. Pipin, and G. Rüdiger, Astron. Nachr. **315**, 157 (1994).

Translated by V. Sakun

How to Create an Alice String (Half-Quantum Vortex) in a Vector Bose–Einstein Condensate¹

U. Leonhardt* and G. E. Volovik***, ****

*School of Physics and Astronomy, University of St. Andrews, KY16 9SS, Scotland

**Department of Physics, Royal Institute of Technology, 100 44 Stockholm, Sweden

***Low Temperature Laboratory, Helsinki University of Technology, 02015 Espoo, Finland

****Landau Institute for Theoretical Physics, Russian Academy of Sciences, ul. Kosygina 2, Moscow, 117940 Russia

Received June 19, 2000

We suggest a procedure of how to prepare a vortex with $N = 1/2$ winding number—a counterpart of the Alice string—in Bose–Einstein condensates. © 2000 MAIK “Nauka/Interperiodica”.

PACS numbers: 03.75.Fi; 67.57.Fg

Vortices with a fractional winding number can exist in different condensed matter systems; see review paper [1]. Observation of atomic Bose condensates with a multi-component order parameter in laser manipulated traps opens the possibility to create half-quantum vortices there. We discuss $N = 1/2$ vortices in a Bose condensate with the hyperfine spin $F = 1$ and also in a mixture of two Bose condensates.

The order parameter of an $F = 1$ Bose condensate consists of three complex components, according to the number of projections $M = (+1, 0, -1)$. These components can be organized to form the complex vector \mathbf{a} :

$$\Psi_{\mathbf{v}} = \begin{pmatrix} \Psi_{+1} \\ \Psi_0 \\ \Psi_{-1} \end{pmatrix} = \begin{pmatrix} (a_x + ia_y)/\sqrt{2} \\ a_z \\ (a_x - ia_y)/\sqrt{2} \end{pmatrix}. \quad (1)$$

There are two symmetrically distinct phases of the $F = 1$ Bose condensates:

(i) The chiral or ferromagnetic state occurs when the scattering length a_2 in the scattering channel of two atoms with the total spin 2 is less than that with the total spin zero, $a_2 < a_0$ [2, 3]. It is described by the complex vector

$$\mathbf{a} = f(\hat{\mathbf{m}} + i\hat{\mathbf{n}}), \quad (2)$$

where $\hat{\mathbf{m}}$ and $\hat{\mathbf{n}}$ are mutually orthogonal unit vectors, with $\hat{\mathbf{l}} = \hat{\mathbf{m}} \times \hat{\mathbf{n}}$ being the direction of the spontaneous momentum \mathbf{F} of the Bose condensate, which violates the parity and time-reversal symmetry; f is the amplitude of the order parameter.

(ii) The polar or superfluid nematic state, which occurs for $a_2 > a_0$, is described up to the phase factor by the real vector

$$\mathbf{a} = f\hat{\mathbf{d}}e^{i\Phi}, \quad (3)$$

where $\hat{\mathbf{d}}$ is a real unit vector. The direction of the vector $\hat{\mathbf{d}}$ can be inverted by a change in phase $\Phi \rightarrow \Phi + \pi$. That is why phase-insensitive properties of the polar state are also insensitive to the reversal of the $\hat{\mathbf{d}}$ direction. In this respect, $\hat{\mathbf{d}}$ is similar to the director in nematic liquid crystals.

The chiral state (i) corresponds to the orbital part of the matrix order parameter in superfluid ³He-A, while the nematic state (ii) corresponds to the spin part of the same ³He-A order parameter. The order parameter matrix of ³He-A is the product of two vector order parameters: $A_{\alpha k} \propto a_{\alpha}^{\text{nematic}} a_k^{\text{chiral}}$. That is why each of the two states shares some definite properties of superfluid ³He-A.

In particular the chiral state (i) displays continuous vorticity [2, 3], which was extensively investigated in superfluid ³He-A (see [4] and reviews [5, 6]). An isolated continuous vortex is the so-called Anderson–Toulouse–Chechetkin vortex. The smooth core of the vortex represents the skyrmion, in which the $\hat{\mathbf{l}}$ -vector sweeps the whole unit sphere. Outside the soft core, the $\hat{\mathbf{l}}$ -vector is uniform, while the order parameter phase has finite winding. In ³He-A and, thus, also in the $F = 1$ Bose condensate, it is the 4π winding around the soft core; i.e., the continuous vortex has winding number $N = 2$. This continuous vortex can also be represented [6, 5] as a pair of the so-called continuous Mermin–Ho vortices [7], each having the winding number $N = 1$.

¹This article was submitted by the authors in English.

The $\hat{\mathbf{I}}$ -vector in the Mermin–Ho vortex covers only half of a unit sphere and thus is not uniform outside the soft core. Such a half-skyrmion is also called a meron. An optical method to create the meron—the Mermin–Ho vortex—in the $F = 1$ Bose condensate has been recently discussed in [8].

For the spin-1/2 Bose condensates, the order parameter is a spinor, which represents “half of the vector”. That is why the continuous Anderson–Toulouse–Chechetkin vortex (in which $\hat{\mathbf{I}}$ sweeps the whole unit sphere) has a winding number that is two times less in such condensates; i.e., the skyrmion is the $N = 1$ continuous vortex [9]. The spinorial order parameter is the counterpart of the order parameter in the Standard Model of the electroweak interactions, which is the spinor Higgs field transforming under the $SU(2)$ symmetry group. That is why the $N = 1$ continuous vortex in the spin-1/2 Bose condensates simulates the continuous electroweak string in the Standard Model. The Higgs field in the continuous electroweak string (and thus the $N = 1$ continuous vortex in the spin-1/2 Bose condensate) has the following distribution of the order parameter [10, 11]:

$$\begin{pmatrix} \Psi_{\uparrow} \\ \Psi_{\downarrow} \end{pmatrix} = f \begin{pmatrix} e^{i\phi} \cos \frac{\theta(r)}{2} \\ \sin \frac{\theta(r)}{2} \end{pmatrix}, \quad (4)$$

$$\hat{\mathbf{I}} = \hat{\mathbf{z}} \cos \theta(r) + \hat{\mathbf{r}} \sin \theta(r).$$

Here, (z, r, ϕ) are coordinates of a cylindrical system, $\theta(0) = \pi$, and $\theta(\infty) = 0$. Note that the meron configuration in such a system, with $\theta(0) = \pi$ and $\theta(\infty) = \pi/2$, would have an $N = 1/2$ winding number.

The $N = 1$ vortices with the order parameter described by Eq. (4), have recently been generated in a Bose condensate with two internal levels [12], following the proposal elaborated in [13]. Though these two internal levels are not related by an exact $SU(2)$ symmetry, under some conditions there is an approximate $SU(2)$ symmetry and the $N = 1$ vortex does represent a skyrmion. This vortex has a smooth (soft) core, whose size is essentially larger than that of the conventional vortex core, which has a dimension of the order of the coherence length. Such enhancement of the core size allowed the observation of the $N = 1$ vortex-skyrmion by optical methods [12]. From Eq. (4), it follows that this continuous $N = 1$ vortex can also be represented as a vortex in the $|\uparrow\rangle$ component, whose core is filled by the $|\downarrow\rangle$ component.

The nematic state (ii) may contain a no less exotic topological object—the topologically stable $N = 1/2$ vortex [14]—which has still eluded experimental identification in superfluid $^3\text{He-A}$. The $N = 1/2$ vortex is a

combination of the π -vortex in the phase Φ and the π -disclination in the nematic order parameter vector $\hat{\mathbf{d}}$:

$$\mathbf{a} = f(r) \left(\hat{\mathbf{x}} \cos \frac{\phi}{2} + \hat{\mathbf{y}} \sin \frac{\phi}{2} \right) e^{i\phi/2}. \quad (5)$$

A change in the sign of the vector $\hat{\mathbf{d}}$ when circumscribing around the core is compensated by a change in sign of the exponent $e^{i\Phi} = e^{i\phi/2}$, so that the whole order parameter is smoothly connected after circumnavigating.

This $N = 1/2$ vortex is the counterpart of the so-called Alice string considered in particle physics [15]: a particle which moves around an Alice string flips its charge or parity. In a similar manner, a quasiparticle moving adiabatically around the vortex in $^3\text{He-A}$ or in a Bose condensate with $F = 1$ in nematic state (ii) finds its spin or its momentum projection M reversed with respect to the fixed environment. This is because the $\hat{\mathbf{d}}$ vector, which plays the role of quantization axis for the spin of a quasiparticle, rotates by π about the vortex. As a consequence, several phenomena (e.g., the global Aharonov–Bohm effect) discussed in the particle physics literature [16, 17] correspond to effects in $^3\text{He-A}$ physics [6, 18], which can be extended to the atomic Bose condensates.

In high T_c superconductors with a nontrivial order parameter, the half-quantum vortex was identified as being attached to the intersection line of three grain boundaries [19], as suggested in [20]. This $N = 1/2$ vortex has been observed via the fractional magnetic flux it generates.

In the spin projection representation, the asymptotic form of the order parameter in the $N = 1/2$ vortex in the nematic phase is

$$\Psi_v \propto e^{i\phi/2} \begin{pmatrix} e^{i\phi/2} \\ 0 \\ e^{-i\phi/2} \end{pmatrix} = \begin{pmatrix} e^{i\phi} \\ 0 \\ 1 \end{pmatrix}. \quad (6)$$

This means that the $N = 1/2$ vortex can be represented as a vortex in the spin-up component $|\uparrow\rangle$, while the spin-down component $|\downarrow\rangle$ is vortex-free. Such a representation of the half-quantum vortex in terms of the regular $N = 1$ vortex in one of the components of the order parameter also occurs in $^3\text{He-A}$. The general form of the order parameter in the half-quantum vortex, which also includes the core structure, is

$$\Psi_v = \begin{pmatrix} f_1(r) e^{i\phi} \\ 0 \\ f_2(r) \end{pmatrix}, \quad f_1(0) = 0, \quad (7)$$

$$|f_1(\infty)| = |f_2(\infty)|.$$

Note that, since the $M = 0$ component in Eq. (6) is zero, the half-quantum vortex can also be generated in the Bose condensate with two internal degrees of freedom explored in [12]. The necessary condition for this is that in the equilibrium state of such condensate both components must be equally populated. This is required by the asymptotic form of Eq. (7), where both components have the same amplitude. If the amplitudes are not exactly equal, the half-quantum vortex acquires a tail in the form of a domain wall terminating on the vortex. The same happens in $^3\text{He-A}$, where the half-quantum vortex is the termination line of the topological soliton.

Equation (6) may suggest a way to generate a half-quantum vortex in an alkali Bose–Einstein condensate simply by combining the successful idea [12, 13] for producing skyrmions with proposal [21] for making scalar vortices by the effect of light forces. Let us start from the homogeneous state

$$\Psi_{\text{v(initial)}} = f \begin{pmatrix} e^{i\alpha} \\ 0 \\ e^{i\beta} \end{pmatrix}, \quad (8)$$

which corresponds to the phase $\Phi = (\alpha + \beta)/2$ and the nematic vector $\hat{\mathbf{d}} = \hat{\mathbf{x}} \cos(\alpha - \beta)/2 + \hat{\mathbf{y}} \sin(\alpha - \beta)/2$. A light spot will illuminate the condensate with an intensity distribution I that draws a half-quantized vortex $I = I_0 e^{i\phi/2}$.

The light should be a short pulse and it should be non-resonant with the atomic transition frequencies. Simultaneously, uniform microwave radiation will penetrate the condensate. The radiation should be detuned far from the transition frequency between the spin components $|\uparrow\rangle$ and $|\downarrow\rangle$ of the condensate, such that it only causes shifts in the relative phases between $|\uparrow\rangle$ and $|\downarrow\rangle$ and no population transfer. The light spot will imprint an optical mask onto the homogeneous microwave field due to the optical Stark effect. Therefore, the generated relative phase shift will follow the half-quantum vortex drawn by the light spot. Simultaneously, the condensate gains an overall scalar phase factor caused by the intensity kick of the light. This factor should exactly compensate for the phase mismatch between the components, which is left from the optically assisted microwave effect. Of course, the intensities of light and microwave radiation should be properly adjusted, but this could be arranged. In this simple way, an Alice string can be created in a multicomponent Bose–Einstein condensate of alkali atoms.

We thank Matti Krusius and Brian Anderson for fruitful discussions. The work of G.E.V. was supported in part by the Russian Foundation for Fundamental Research and by the European Science Foundation. U.L. was supported by the Alexander von Humboldt Foundation and the Goran Gustafsson Stiftelse.

REFERENCES

1. G. E. Volovik, Proc. Natl. Acad. Sci. USA **97**, 2431 (2000).
2. T. L. Ho, Phys. Rev. Lett. **81**, 742 (1998).
3. T. Isoshima, M. Nakahara, T. Ohmi, and K. Machida, cond-mat/9908470; T. Ohmi and K. Machida, J. Phys. Soc. Jpn. **67**, 1822 (1998).
4. R. Blaauwgeers, V. B. Eltsov, H. Götz, *et al.*, Nature (London) (2000) (in press).
5. V. B. Eltsov and M. Krusius, in *Topological Defects and the Non-Equilibrium Dynamics of Symmetry Breaking Phase Transitions*, Ed. by Y. M. Bunkov and H. Godfrin, (Kluwer, Dordrecht, 2000), pp. 325–344.
6. M. M. Salomaa and G. E. Volovik, Rev. Mod. Phys. **59**, 533 (1987).
7. N. D. Mermin and T. L. Ho, Phys. Rev. Lett. **36**, 594 (1976).
8. K. P. Marzlin, W. Zhang, and B. C. Sanders, cond-mat/0003273.
9. T. L. Ho, *Bose–Einstein Condensates with Internal Degrees of Freedom*, invited talk at International Conference on Low Temperature Physics LT-22, Helsinki, August 1999.
10. M. Hindmarsh and T. W. B. Kibble, Rep. Prog. Phys. **58**, 477 (1995).
11. A. Achucarro and T. Vachaspati, Phys. Rep. **327**, 347 (2000).
12. M. R. Matthews, B. F. Anderson, P. C. Haljan, *et al.*, Phys. Rev. Lett. **83**, 2498 (1999).
13. J. E. Williams and M. J. Holland, Nature (London) **401**, 568 (1999).
14. G. E. Volovik and V. P. Mineev, Pis'ma Zh. Éksp. Teor. Fiz. **24**, 605 (1976) [JETP Lett. **24**, 561 (1976)].
15. A. S. Schwarz, Nucl. Phys. B **208**, 141 (1982).
16. J. March-Russel, J. Preskill, and F. Wilczek, Phys. Rev. D **50**, 2567 (1992).
17. A. C. Davis and A. P. Martin, Nucl. Phys. B **419**, 341 (1994).
18. M. V. Khazan, Pis'ma Zh. Éksp. Teor. Fiz. **41**, 396 (1985) [JETP Lett. **41**, 486 (1985)].
19. J. R. Kirtley, C. C. Tsuei, M. Rupp, *et al.*, Phys. Rev. Lett. **76**, 1336 (1996).
20. V. Geshkenbein, A. Larkin, and A. Barone, Phys. Rev. B **36**, 235 (1987).
21. L. Dobrek, M. Gajda, M. Lewenstein, *et al.*, Phys. Rev. A **60**, R3381 (1999).

Size Quantization of Acoustic Phonons in CuCl Nanocrystals

S. V. Gupalov and I. A. Merkulov

Ioffe Physicotechnical Institute, Russian Academy of Sciences, Politekhnikeskaya ul. 26, St. Petersburg, 194021 Russia
e-mail: gupalov@coherent.ioffe.rssi.ru

Received June 21, 2000

It is shown that the mixed character of spheroidal vibrational modes of semiconductor quantum dots of spherical shape may lead to the appearance of a line in the low-frequency Raman spectra of nanocrystals whose spectral position is independent of the average radius of nanocrystals in the sample over a wide range of sizes. This effect is associated with the rapid saturation of the dispersion dependence for transversal acoustic phonons in the bulk semiconductor. The maximum radius of quantum dots at which the line indicated above is observed in the spectrum has been estimated. © 2000 MAIK “Nauka/Interperiodica”.

PACS numbers: 63.20.Dj; 78.30.Hv; 78.66.Li

In recent years, the physics of semiconductor nano-heterostructures has developed into an independent field of investigation in solid-state physics. Quasi-two-dimensional structures (quantum wells) based on cubic semiconductors, which possess lower symmetry than the bulk crystal, are the best understood objects in this field. The reduction of symmetry in low-dimensional systems results in the degenerate states of heavy and light holes at the top of the valence band (the Γ point of the Brillouin zone) becoming split upon size quantization. As a consequence, two sets of size-quantization levels (and related subbands) arise, which correspond to heavy and light holes at the wave vector in the plane of layers equal to zero. A different situation is observed in quantum dots of spherical shape (nanocrystals). These objects possess the same symmetry as the bulk semiconductor. Therefore, the size-quantization levels generally correspond to mixed states with contributions from both heavy and light holes [1, 2]. The spatial confinement similarly affects acoustic phonons as well: so-called spheroidal vibrational modes arise, which are neither longitudinal nor transversal, but have a mixed character (see [3] and references therein). At first glance, it seems that this should not strongly affect the experimentally observed properties of the system. In fact, the mixed character of size-quantization hole levels in spherical nanocrystals affects their energy position, but their dependence on the nanocrystal radius remains proportional to R^{-2} . Analogously, the eigenfrequencies of the spheroidal vibrational modes of a spherical quantum dot, as well as the frequencies of the purely longitudinal, totally symmetric mode and the purely transversal, torsional modes, are inversely proportional to the radius of the quantum dot. Therefore, the manifestation of the mixed character of holes and acoustic phonons is of a quantitative, rather than qualitative, nature. However, it is not difficult to imagine a situation when the mixed character of size-quantized particles is of princi-

pal importance. It is this situation that is accomplished in nature for acoustic phonons in spherical CuCl nanocrystals. In this case, the transversal component of spheroidal vibrations ensures the high density of size-quantized states at the frequency of the boundary bulk *TA* phonons, and the contribution of the longitudinal component leads to efficient exciton–phonon interaction. As a result, an intense line is observed in the low-frequency Raman spectra at the frequency of the boundary bulk *TA* phonons, whose energy position does not depend on the radius of the quantum dot.¹ Below, we will first discuss the peculiarities of the quantization of acoustic phonons in nanocrystals and the selection rules for low-frequency Raman scattering, and then we will pass to the consideration of the situation characteristic of CuCl.

Raman scattering by acoustic phonons in nanocrystals. Low-frequency Raman scattering in semiconductor nanocrystals has been extensively studied in recent years [3–10]. Generally, one or several narrow peaks are observed in Raman spectra, whose energy position is inversely proportional to the average radius of nanocrystals in the sample. This fact, as was mentioned above, is a consequence of the size quantization of acoustic phonons. Actually, if a nanocrystal is considered as a homogeneous elastic sphere, each vibrational mode can be associated with a discrete set of eigenfrequencies, the distance between which is inversely proportional to the sphere radius. A vibration of the sphere is characterized by the values of the angular momentum (the total angular momentum of the phonon) and its projection, and, additionally, it belongs to one of the two types. The torsional vibrations relate to the first type. These vibrations are purely transversal; that is, the divergence of the displacement vector for these vibrations equals zero. The vibrations of the second type have come to be known as

¹ A.I. Ekimov, private communication.

spheroidal. These vibrations are of a mixed nature; that is, in general, neither the divergence nor the rotor of the displacement vector for such vibrations vanishes. Note that there also exists a degenerate case of spheroidal vibrations corresponding to the total angular momentum of the phonon $F = 0$. These are so-called breathing or totally symmetric vibrations, which are purely longitudinal.

The selection rules for low-frequency Raman scattering in nanocrystals were discussed in a number of works [3, 11]. In [3], the processes were considered in which a quasi-zero-dimensional exciton in the ground state interacting with acoustic phonons through the deformation potential served as an intermediate state for light scattering. It was shown that only scattering processes with the participation of totally symmetric phonons are possible when the exciton is formed by an electron and a hole from simple (twofold spin degenerate) bands ($\Gamma_6 \times \Gamma_7$ exciton in crystals of the T_d class). If the hole forming the exciton is characterized by the spin $J = 3/2$ ($\Gamma_6 \times \Gamma_8$ exciton in crystals of the T_d class), processes with the participation of spheroidal phonons with the total angular momentum $F = 2$ are also allowed. Note that piezoelectric interaction must be taken into account in polar crystals along with exciton-phonon interaction through the deformation potential. However, only the removal of forbiddenness for the interaction with spheroidal vibrations with the angular momentum $F = 2$ will be important in the subsequent discussion. It has been mentioned above that the sufficient condition for this removal is the occurrence of interaction through the deformation potential and a complex structure of the valence band. Therefore, we will not compare the efficiency of these two mechanisms of exciton-phonon interaction.

Because the intermediate state through which Raman scattering is carried out (quasi-zero-dimensional exciton) is localized within a length of the order of the nanocrystal radius, phonons with a wavelength of the same order of magnitude will most efficiently interact with this state. Therefore, only a small number of features corresponding to vibrations of a certain symmetry can be observed in low-frequency Raman spectra.

Thus, narrow lines corresponding to scattering by spheroidal phonons with the total angular momentum $F = 0$ and $F = 2$ at frequencies inversely proportional to the average radius of nanocrystals in the sample must be observed in low-frequency Raman spectra of semiconductor nanocrystals for excitation at a frequency close to the absorption line associated with the excitation of an exciton with a hole with the spin $J = 3/2$. Such spectra were observed in a number of works in which CdS, CdSe, and CdS_xSe_{1-x} dispersed in various glass matrices were studied [4, 5, 7–10].

The aforesaid is related in full measure only to the situation when the acoustic phonons in a bulk semiconductor are described by a linear dispersion law. A characteristic feature of bulk CuCl is the fact that the frequen-

cies of longitudinal acoustic phonons at the boundaries of the Brillouin zone significantly exceed the frequencies of transversal acoustic phonons. Thus, at the point X of the Brillouin zone at $T = 4.2$ K, $\Omega_{TA}(X) = 38.6 \pm 4$ cm⁻¹ and $\Omega_{LA}(X) = 123 \pm 6$ cm⁻¹ [12]. Moreover, the dispersion branches of transversal acoustic phonons are saturated rapidly. In this case, the dispersion dependence for the LA phonons may be considered linear to a great degree of accuracy in the region where the dispersion law for the bulk TA phonons is strongly nonlinear. The dispersion law of the bulk acoustic phonons in CuCl for the [100], [110], and [111] directions is given in [12]. The dispersion branch corresponding to the TA phonons for the [100] direction is twofold degenerate and goes to saturation at the point $[\xi 00]$ where $\xi \approx 0.4$. Below, we will consider that the phonon spectrum is isotropic and coincides with the spectrum for the [100] direction.

Quantization of acoustic phonons in CuCl nanocrystals. Consider how the above peculiarity of bulk CuCl is formally manifested in the quantization of phonons in a nanocrystal. The displacement of points inside a spherical nanocrystal for a spheroidal vibrational mode with the total angular momentum F and its projection F_z can be written as a linear combination of the longitudinal $\mathbf{u}_{F, F_z}^s(\mathbf{r}, t)$ and the transversal $\mathbf{u}_{F, F_z}^{v2}(\mathbf{r}, t)$ solutions [3]:

$$\begin{aligned} \mathbf{u}_{F, F_z}(\mathbf{r}, t) = & a\mathbf{u}_{F, F_z}^s(\mathbf{r}, t) + b\mathbf{u}_{F, F_z}^{v2}(\mathbf{r}, t) \\ & \times \left\{ [a\sqrt{F+1}j_{F+1}(q_l r) + b\sqrt{F}j_{F+1}(q_t r)] \mathbf{Y}_{F, F_z}^{F+1}\left(\frac{\mathbf{r}}{r}\right) \right. \\ & \left. + [a\sqrt{F}j_{F-1}(q_l r) - b\sqrt{F+1}j_{F-1}(q_t r)] \mathbf{Y}_{F, F_z}^{F-1}\left(\frac{\mathbf{r}}{r}\right) \right\} \\ & \times \exp(-i\Omega t) + \text{c.c.}, \end{aligned} \quad (1)$$

where Ω is the phonon energy, q_l and q_t are the wave numbers of the longitudinal and the transversal bulk

phonons with the energy Ω , $\mathbf{Y}_{F, F_z}^L\left(\frac{\mathbf{r}}{r}\right)$ are spherical vectors, and $j_L(x)$ are Bessel spherical functions. The coefficients a and b in this linear combination are determined from the boundary conditions at $r = R$. We will neglect the probability of phonon passage from the nanocrystal to the surrounding matrix. Then, the vibrational spectrum is discrete and the eigenfrequencies are obtained from the dispersion equation that follows from the boundary conditions at $r = R$. From the form of the displacement given by Eq. (1), it is clear that the dispersion equation will take the form

$$e(q_l R)f(q_t R) + g(q_l R)h(q_t R) = 0, \quad (2)$$

where $e(x)$, $f(x)$, $g(x)$, and $h(x)$ are functions that depend on the specific form of the boundary conditions and oscillate with the characteristic distance between its

zeros of the order of several π . For the boundary conditions corresponding to a sphere with a free surface, these functions in the explicit form are given, for example, in [6]. If, in some region of frequencies, the dependence $q_l(\Omega)$ is linear and the dependence $q_t(\Omega)$ is super-linear, it is clear that $f(q_l R)$ and $h(q_t R)$, as functions of the frequency Ω , will oscillate much more frequently than $e(q_l R)$ and $g(q_t R)$, determining the characteristic distance between the roots of Eq. (2) and, consequently, between the eigenfrequencies of vibrations. Therefore, a large number of vibrational levels corresponding to spheroidal acoustic phonons, in particular, with the total angular momentum $F = 2$, will crowd together at the frequency of the boundary bulk TA phonons. The number of these levels is determined by the number of roots of the dispersion equation (2) that fall within the saturation region of the dispersion branch of bulk TA phonons and is approximately equal to $N \approx (1 - \xi)R/a$, where a is the lattice constant. Hence, a line must be observed at this frequency in low-frequency Raman spectra of nanocrystals for excitation at the absorption line associated with a $\Gamma_6 \times \Gamma_8$ exciton ($Z_{1,2}$ line), and its intensity must be N times higher compared to the case of the linear dispersion of bulk TA phonons.

According to [3], the matrix element of the exciton–phonon interaction through the deformation potential between the vibrations of the form given by Eq. (1) (with $F = 2$) and a quasi-zero-dimensional $\Gamma_6 \times \Gamma_8$ exciton in the spherical approximation is proportional to the quantity $aq_l B_v(q_l R) - \sqrt{6} b q_t C_v(q_t R)$, where $B_v(x)$ and $C_v(x)$ are functions determined in [3]. These functions differ significantly from zero at the values of x smaller than, or of the order of, several π . The last circumstance reflects the fact that phonons with a wavelength of the order of the diameter of the quantum dot interact with an exciton localized within the quantum dot most efficiently. At the frequency of the boundary bulk TA phonons Ω_0 , $q_l \sim \pi/a$. Therefore, $q_l R \sim \pi R/a \gg \pi$ and the contribution from the transversal component of the spheroidal vibration to the exciton–phonon interaction can be neglected. In this case, $q_l \sim \Omega_0/c_l$, where c_l is the longitudinal sound velocity. Therefore, the value of R_0 at which the value of $\Omega_0 R_0/c_l$ becomes of the order of several π determines the maximum radius of the nanocrystal for which the line at the frequency Ω_0 is still present in the low-frequency Raman spectrum. An estimation gives $R_0 \sim 50 \text{ \AA}$.

It is important to note that the existence of a line in the low-frequency Raman spectra that does not depend on the average radius of nanocrystals is due to the mixed character of spheroidal vibrations with the angular momentum $F = 2$. Actually, if these vibrations had no longitudinal component, they would scarcely interact with a quasi-zero-dimensional exciton and would not be observed in Raman scattering. At the same time, the absence of the longitudinal component would lead to the fact that the lines at frequencies in the vicinity of

Ω_0 could not be distinguished from the lines corresponding to size-quantized vibrations with frequencies inversely proportional to the average radius of nanocrystals in the sample.

Thus, we showed that, because of the mixed character of spheroidal vibrations, an intense line must be observed in the low-frequency Raman spectra of spherical CuCl nanocrystals. This line is located at the saturation frequency of the dispersion dependence of transversal acoustic phonons in the bulk semiconductor. The longitudinal component of spheroidal vibrations ensures the efficiency of exciton–phonon interaction, and the transversal component provides for the large density of states at the saturation frequency. We emphasize that the occurrence of a line in the spectrum whose position does not depend on the average radius of nanocrystals over a wide size range is rather untypical for quasi-zero-dimensional systems. Actually, the size-quantization effect is usually manifested as a strong dependence of all the characteristic energies of the system on the size of the object. Thus, the dependence $E \propto R^{-1}$ is observed for the eigenfrequencies of acoustic vibrations in spherical nanocrystals, the dependence $E \propto R^{-2}$ is observed for the size-quantization levels of carriers (excitons), and even the dependence $E \propto R^{-3}$ is observed for the exchange splitting of excitonic levels [13, 14]. We note in conclusion that, along with the line described above, lines from unmixed phonon modes with $F = 0$ and from mixed phonon modes with $F = 2$ can be observed experimentally at frequencies at which both the dispersion branches of acoustic phonons in the bulk semiconductor are linear. The position of all these lines must be inversely proportional to the average radius of nanocrystals in the sample.

We are grateful to A.I. Ekimov, who familiarized us with unpublished experimental results on low-frequency Raman scattering in CuCl nanocrystals. The work was partially supported by the program Nanostructures of the Russian Ministry of Science, by the Russian Foundation of Basic Research (project nos. 00-02-16997 and 00-02-16991), and by the program of support for young scientists of Russian Academy of Sciences. One of the authors (S. G.) is grateful to INTAS (project no. 99-00015) for financial support of this work.

REFERENCES

1. G. B. Grigoryan, É. M. Kazaryan, Al. L. Éfros, and T. V. Yazeva, *Fiz. Tverd. Tela (Leningrad)* **32**, 1772 (1990) [*Sov. Phys. Solid State* **32**, 1031 (1990)].
2. P. C. Sercel and K. J. Vahala, *Phys. Rev. B* **42**, 3690 (1990).
3. S. V. Gupalov and I. A. Merkulov, *Fiz. Tverd. Tela (St. Petersburg)* **41**, 1473 (1999) [*Phys. Solid State* **41**, 1349 (1999)].
4. A. Tanaka, S. Onari, and T. Arai, *Phys. Rev. B* **47**, 1237 (1993).
5. A. Roy and A. K. Sood, *Solid State Commun.* **97**, 97 (1996).

6. T. Takagahara, J. Lumin. **70**, 129 (1996).
7. L. Saviot, B. Champagnon, E. Duval, *et al.*, J. Non-Cryst. Solids **197**, 238 (1996).
8. L. Saviot, B. Champagnon, E. Duval, and A. I. Ekimov, J. Cryst. Growth **184/185**, 370 (1998); Phys. Rev. B **57**, 341 (1998).
9. P. Verma, W. Cordts, G. Irmer, and J. Monecke, Phys. Rev. B **60**, 5778 (1999).
10. V. G. Melehin and V. D. Petrikov, Phys. Low-Dimens. Struct. **9/10**, 73 (1999).
11. E. Duval, Phys. Rev. B **46**, 5795 (1992).
12. B. Prevot, B. Hennion, and B. Dorner, J. Phys. C **10**, 3999 (1977); *Landolt-Börnstein Numerical Data and Functional Relationships in Science and Technology*, Ed. by O. Madelung (Springer-Verlag, Berlin, 1982), Vol. III/17b.
13. M. Nirmal, D. J. Norris, M. Kuno, *et al.*, Phys. Rev. Lett. **75**, 3728 (1995).
14. S. V. Goupalov and E. L. Ivchenko, J. Cryst. Growth **184/185**, 393 (1998); Acta Phys. Pol. A **94**, 341 (1998).

Translated by A. Bagatur'yants

Electronic Structure of Carbon Multilayer Nanotubes

A. S. Kotosonov* and V. V. Atrazhev**

*Research Institute of Structural Graphite Materials, Elektrodnaya ul. 2, Moscow, 111524 Russia

**Emanuel Institute of Biochemical Physics, Russian Academy of Sciences, ul. Kosygina 4, Moscow, 117977 Russia

Received May 24, 2000; in final form, June 20, 2000

The integral electron density of states at the Fermi level in carbon multilayer nanotubes, which belong to quasi-one-dimensional systems, has been calculated within the tight-binding approximation. It is shown that the density-of-state functions for nanotubes with 20 or more layers and for quasi-two-dimensional graphites virtually coincide. This agreement explains the successful application of the band theory of quasi-two-dimensional graphite to the description of magnetic properties of nanotubes over a wide temperature range. © 2000 MAIK "Nauka/Interperiodica".

PACS numbers: 73.20.-r; 71.24.+q

Carbon nanotubes consist of coiled graphene layers and represent hollow seamless cylinders of nanometer diameter and several micrometers in length [1]. The symmetry type, diameter, and electronic structure of one-layer nanotubes are almost fully characterized by integer indices (n , m) uniquely related to the unit cell parameters of the tube [2–4]. It was shown by theoretical calculations that, depending on the indices (n , m), one-layer nanotubes can be both metals and semiconductors. If the value of q in the relationship $2n + m = 3q$ equals an integer number, the one-layer nanotubes belong to metals; otherwise, the tubes are semiconductors [5–7]. With increasing n and m , the diameter of a one-layer nanotube grows and the band gap decreases in inverse proportion to its diameter. At the same time, having virtually equal diameters ($d_t \approx 1.36$ nm), an (11, 9) tube has an interband gap of 0.62 eV, whereas a (10, 10) tube is a metal.

Recently, considerable progress has been achieved in obtaining and experimentally studying one-layer nanotubes. However, the majority of the nanotubes obtained in amounts sufficient for their investigation and application belong to multilayer nanotubes. In multilayer nanotubes, the cylinders are coaxially inserted into each other, three-dimensional order is lacking because of the steric constraints on the neighboring layers, and the interlayer distance (≈ 0.344 nm) is larger than in the graphite crystal (0.3354 nm). Extensive investigations of multilayer nanotubes showed that they possess interesting electrical and magnetic properties promising for applications. In particular, it was experimentally shown in [8–12] that the orientationally averaged magnetic susceptibility of some multilayer nanotubes is no lower than that of graphite and is exceeded only by that of superconductors. At the same time, a satisfactory explanation was provided neither for the absolute value nor for the temperature dependence of the diamagnetic susceptibility of the multilayer nano-

tubes studied [8–12]. This was evidently due to difficulties associated with choosing a suitable band model.

The first theoretical estimates of the magnetic susceptibility were made for one-layer nanotubes [13, 14]. It was found that their susceptibility depends intricately on the diameter and chirality and on the magnetic field strength. However, the main conclusion of [13, 14] was that one-layer nanotubes must be diamagnets, and the diamagnetic susceptibility perpendicular to the tube axis must be higher than that along the axis. However, it was stated in [15] that the diamagnetic susceptibility component along a nanotube could be dominant because of ring currents around the belts of the one-layer nanotube. Unfortunately, in order to compare particular estimates with experimental data, the number of one-layer nanotubes with the same structure must be sufficient for measurements, which cannot as yet be accomplished in practice.

As to multilayer nanotubes, it was shown only rather recently in [16–18] that the quasi-two-dimensional graphite band model [19], which had been developed previously to explain the electronic properties of graphites with a turbostratic structure, could be formally used for the description of diamagnetism, g factor, and spin paramagnetic susceptibility of current carriers in multilayer nanotubes over a wide temperature range. This model also turned out to be useful both for treating the magnetic properties of graphite clusters [20] and for understanding the published measurements of the diamagnetic susceptibility of multilayer nanotubes [8–12].

As a rule, the band theory of quasi-two-dimensional graphite was successfully used for treating the electronic properties of many carbon materials with a distinct two-dimensional graphite structure of a planar type. Because typical multilayer nanotubes 10–30 nm in diameter are considered to be quasi-one-dimensional objects, the applicability of the quasi-two-dimensional graphite model to these systems must be confirmed by relatively independent theoretical estimates. In this connection,

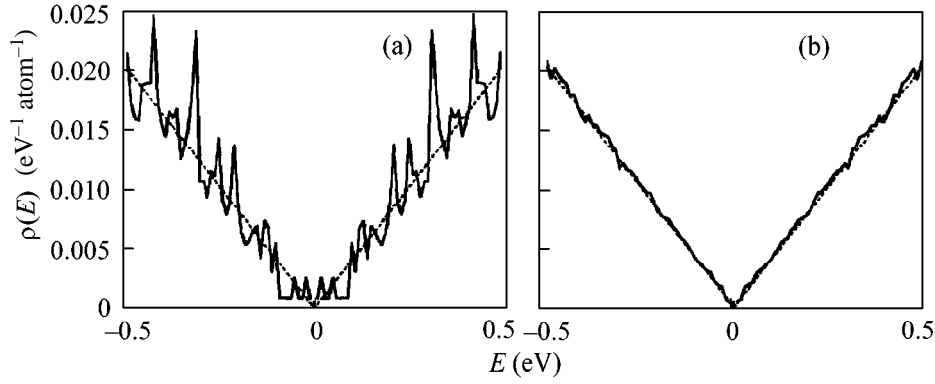


Fig. 1. Density of states $\rho(E)$ for (a) 5-layer and (b) 20-layer nanotubes in comparison with the function $\rho(E)$ for two-dimensional graphite (dashed lines).

this work was devoted to calculations of the integral electron density of states for multilayer nanotubes at the Fermi level, which coincides with the region where the valence and conduction bands touch each other. The tight-binding approximation, which was repeatedly applied to studying one-layer nanotubes [5–7], was used in the calculations.

The energy spectrum of π electrons of a one-layer (n, m) nanotube without regard to the curvature of the surface takes the form [7]

$$E(k_x, k_y) = \pm \gamma_0 \left\{ 1 + 4 \cos \left[\frac{3a_0}{2} (k_y \cos \theta + k_x \sin \theta) \right] \right. \\ \times \cos \left[\frac{\sqrt{3}a_0}{2} (k_y \sin \theta - k_x \cos \theta) \right] \\ \left. + 4 \cos^2 \left[\frac{\sqrt{3}a_0}{2} (k_y \sin \theta - k_x \cos \theta) \right] \right\}^{1/2}, \quad (1)$$

where the y and x axes are directed, respectively, along the axis and the perimeter of the tube. The quasi-continuous wave vector k_y scans the values $k_y \leq \pi/a_0 \sqrt{3(p^2 + q^2 + pq)}$ in the first Brillouin zone, and

the discrete wave vector $k_x = 2\pi J/a_0 \sqrt{3(n^2 + m^2 + nm)}$ numbers the branches of the spectrum. Here, $J = 1, 2, \dots, N/2$, N is the number of atoms in the unit cell and a_0 is the distance between the neighboring atoms in the layer (0.142 nm). The parameters (p, q) of the primitive translation vector along the tube axis are found as the least integer numbers obeying the condition $p(2n + m) + q(2m + n) = 0$. The parameter γ_0 is defined by the interaction of π electrons of the nearest neighboring atoms in the layer (≈ 3 eV). The angle θ characterizes the chirality of a one-layer nanotube and is found from the relationship $\theta = \tan^{-1}(3^{1/2}m/(m + 2n))$.

Because one-layer nanotubes are quasi-one-dimensional objects, their density of states has singularities in

the form of peaks $1/(E - E_N)^{1/2}$ and the number of these singularities equals the number of spectrum branches. If the interlayer interaction is neglected, the density of states for a multilayer nanotube is a sum of the density of states over all the tubes taken with the corresponding normalization factors. The neglect of the interlayer interaction is fully justified, because it is two orders of magnitude smaller than γ_0 and only slightly changes the electronic spectrum of each tube. This is confirmed by the results of numerical calculations of the electronic spectrum for two- and three-layer tubes with allowance made for the interlayer interaction [5, 21]. Then, the total density of states will be a function with a quasi-random distribution of peaks. In real experiments, a sample consists of a great number of tubes, and the density of states is averaged over the tubes differing in diameter and chirality.

Numerical calculations of the density of states were performed for multilayer nanotubes differing in the number of layers. The radius of the smallest tube was taken to be 0.678 nm, which corresponded to a (10, 10) or (11, 9) tube, and the radius of each subsequent tube was increased by 0.344 ± 0.002 nm. In the calculations, tubes of any chirality that obeyed this condition were taken into account. The density of states was calculated from its definition $\rho(E, \Delta E) = (\Delta N/\Delta E)/N$, where ΔN is the number of states within the energy interval ΔE and N is the total number of states. For each tube, the vector k_y scans a discrete set of values in the first Brillouin zone and the corresponding energy levels are calculated by Eq. (1). The energy interval under consideration is divided into intervals ΔE , and the number of states within this interval is $\rho(E)N\Delta E$. Generally speaking, ΔE should be set zero, but the numerical calculation were performed with $\Delta E = 10$ meV. The density of states obtained was the average over the energy interval ΔE , and density fluctuations on a smaller scale were not considered. However, if $kT > \Delta E$, the fine details of $\rho(E)$ are insignificant.

Figure 1 displays the energy dependence of the density of states in the vicinity of the band touch region for

a multilayer nanotube with (a) 5 and (b) 20 cylinders. It is evident that, in the case of 20-layer tubes ($d_t \approx 14$ nm), it virtually coincides with $\rho(E)$ for two-dimensional graphite. That is, whereas $\rho(E)$ of an isolated tube has one-dimensional singularities, $\rho(E)$ of a multilayer nanotube with a large number of layers is an almost smooth linear function near the band center. As for quasi-two-dimensional graphite, the density-of-state function for a multilayer nanotube in the vicinity of a conical point is approximated well by the linear relationship $\rho(E) = 0.041|E| \text{ eV}^{-1} \text{ atom}^{-1}$. This approximation is good over a rather wide energy interval ($-0.5, +0.5$ eV).

In perfect quasi-two-dimensional graphites and multilayer nanotubes, the valence band at a temperature $T = 0$ is fully filled and the conduction band is empty; that is, the Fermi level coincides with the zeroth conical point. However, similar to impurity boron atoms, the structural defects inherent in these materials are acceptors and shift the Fermi level deep into the valence band, creating extrinsic holes in the graphene layer with a concentration on the order of 10^{10} – 10^{12} cm^{-2} (depending on the layer imperfection or the degree of doping). As a rule, the concentrations of holes and defects coincide in these materials, and the defects serve as effective scattering centers for current carriers and lead to the broadening of the density of states in the vicinity of the conical point and the Fermi level. In the calculation of magnetic and electrical properties, this broadening is formally taken into account by introducing an effective temperature $T_e = T + \delta$, where the additional parameter δ is connected with the extrinsic carrier degeneracy temperature T_0 by the relationship $\delta \approx 0.5T_0$ in the case of linear defects or $\delta \approx (0.1\text{--}0.15)T_0$ if ionized point defects are predominant [16–19].

As an example, Fig. 2 shows a comparison between the measured diamagnetic susceptibilities for multilayer nanotubes at 70–900 K and the values calculated within the quasi-two-dimensional graphite band model. Nanotubes with an average diameter of ≈ 15 nm were chosen for this study. The multilayer nanotubes were prepared and characterized by the methods described in [18]. The diamagnetic susceptibility measurements were performed at a magnetic field strength of 2–9 kOe with the use of an electronic microbalance. The measurement error did not exceed 10^{-8} emu/g .

It is known that the diamagnetic susceptibility along a multilayer nanotube, as well as along the graphite layers, is small and coincides with the atomic susceptibility of carbon $\chi_a = -0.3 \times 10^{-6} \text{ emu/g}$. The large diamagnetism of quasi-two-dimensional graphites and multilayer nanotubes is related to the diamagnetic susceptibility component in the direction perpendicular to the carbon layers (χ_3) and is determined by the interband contribution to the diamagnetic susceptibility of current carriers, which equals $\chi_3 - \chi_a$. It is important to note that the diamagnetic susceptibility perpendicular to the axis of a multilayer nanotube equals $(\chi_3 + \chi_a)/2$; that is, at the

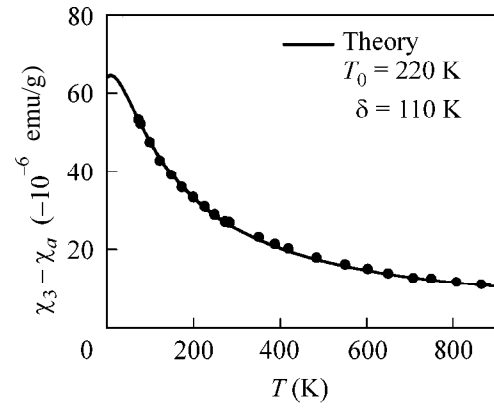


Fig. 2. Temperature dependence of the diamagnetic susceptibility of current carriers in multilayer nanotubes; the points are for the experimental data, and the solid line is for the calculation within the framework of the quasi-two-dimensional graphite band model.

same value of χ_3 , the anisotropy of a multilayer nanotube is two times smaller than the anisotropy of quasi-two-dimensional graphite. Independent of the material type, the experimental value of $\chi_3 - \chi_a$ is found from the relationship $\chi_3 - \chi_a = 3\langle\chi\rangle - 3\chi_a$, where $\langle\chi\rangle$ is the orientationally averaged magnetic susceptibility of the sample.

For the chosen tubes, the measured values of $\chi_3 - \chi_a$ are presented in Fig. 2 by points. It is evident that the experimental data are actually approximated well by the calculated curve obtained within the quasi-two-dimensional graphite band model with the use of equations and methods presented in [16, 18, 19]. As for quasi-two-dimensional graphite, it was assumed in the calculations of the diamagnetic susceptibility of multilayer nanotubes that $\gamma_0 = 3 \text{ eV}$. The extrinsic carrier degeneracy temperature T_0 and δ were the only fitting parameters. The value of T_0 (220 K) corresponds to a hole concentration of $2.7 \times 10^{10} \text{ cm}^{-2}$. The value of $0.5T_0$ found for δ points to the linear character of the layer defects [16–19]. For the same type of defects, the diamagnetic susceptibility of multilayer nanotubes is proportional to $1/T_0$. At low concentrations of defects, the diamagnetic susceptibility of nanotubes may be higher than that of quasi-two-dimensional graphite and can be several times higher than the diamagnetic susceptibility of a single crystal of graphite at low temperatures. For high imperfection of the carbon layers, the diamagnetism of multilayer nanotubes can drop down to the value of χ_a . If the number of layers in multilayer nanotubes decreases to 5–7, the diamagnetism of nanotubes decreases and quantitative analysis with the use of the quasi-two-dimensional graphite model becomes impossible, as it is seen in Fig. 1a. Moreover, the $\rho(E)$ function essentially depends on the diameter and chirality of tubes composing the small-diameter multilayer nanotubes.

At the same time, the successful application of the quasi-two-dimensional graphite band model to multi-

layer nanotubes with an average diameter of ≥ 14 nm for the explanation of diamagnetic susceptibility in this work and in the works [16, 18], as well as for the explanation of the spin paramagnetism and g factor of current carriers in [17], allows the suggestion that the integral density of states for all the layers actually predetermines the magnetic properties of these quasi-one-dimensional objects. The justified use of the quasi-two-dimensional graphite model significantly facilitates the process of quantitative description and explanation of experimental data obtained for multilayer nanotubes.

This work was supported by the Russian Foundation for Basic Research (project nos. 99-03-32382 and 99-03-33208) and the program "Fullerenes and Atomic Clusters" (project no. 20006).

REFERENCES

1. S. Iijima, *Nature* (London) **354**, 56 (1991).
2. R. Saito, M. Fujita, G. Dresselhaus, and M. S. Dresselhaus, *Phys. Rev. B* **46**, 1804 (1992).
3. J. W. Mintmire, B. I. Dunlap, and C. T. White, *Phys. Rev. Lett.* **68**, 631 (1992).
4. N. Hamada, S. Savada, and A. Oshiyama, *Phys. Rev. Lett.* **68**, 1579 (1992).
5. M. S. Dresselhaus, G. Dresselhaus, and R. Saito, *Carbon* **33**, 883 (1995).
6. J. W. Mintmire and C. T. White, *Carbon* **33**, 893 (1995).
7. V. F. Lin and Kenneth W.-K. Shung, *Phys. Rev. B* **51**, 7592 (1995).
8. J. Heremans, C. H. Olk, and D. T. Morelli, *Phys. Rev. B* **49**, 15122 (1994).
9. X. K. Wang, R. P. H. Chang, A. Patashinski, and J. B. Ketterson, *J. Mater. Res.* **9**, 1578 (1994).
10. A. P. Ramirez, R. C. Haddon, O. Zhou, *et al.*, *Science* (Washington, D.C.) **265**, 84 (1994).
11. O. Chauvet, L. Forro, W. Basca, *et al.*, *Phys. Rev. B* **52**, 6963 (1995).
12. S. Bandow, *J. Appl. Phys.* **80**, 1020 (1996).
13. R. Saito, G. Dresselhaus, and M. S. Dresselhaus, *Phys. Rev. B* **50**, 14698 (1994).
14. H. Ajiki and T. Ando, *J. Phys. Soc. Jpn.* **62**, 2470 (1993); **64**, 4382 (1995).
15. J. P. Lu, *Phys. Rev. Lett.* **74**, 1123 (1995).
16. A. S. Kotosonov and S. V. Kuvshinnikov, *Phys. Lett. A* **230**, 377 (1997).
17. A. S. Kotosonov and D. V. Shilo, *Carbon* **36**, 1649 (1998).
18. A. S. Kotosonov, *Pis'ma Zh. Éksp. Teor. Fiz.* **70**, 468 (1999) [*JETP Lett.* **70**, 476 (1999)]; erratum: *Pis'ma Zh. Éksp. Teor. Fiz.* **70**, 690 (1999) [*JETP Lett.* **70**, 709 (1999)].
19. A. S. Kotosonov, *Pis'ma Zh. Éksp. Teor. Fiz.* **43**, 30 (1986) [*JETP Lett.* **43**, 37 (1986)]; *Zh. Éksp. Teor. Fiz.* **93**, 1870 (1987) [*Sov. Phys. JETP* **66**, 1068 (1987)]; *Fiz. Tverd. Tela* (Leningrad) **33**, 2616 (1991) [*Sov. Phys. Solid State* **33**, 1477 (1991)].
20. O. E. Andersson, B. L. V. Prasad, H. Sato, *et al.*, *Phys. Rev. B* **58**, 16387 (1998).
21. A. A. Ovchinnikov and V. V. Atrazhev, *Fiz. Tverd. Tela* (St. Petersburg) **40**, 1950 (1998) [*Phys. Solid State* **40**, 1769 (1998)].

Translated by A. Bagatur'yants

Short-Pitch and Long-Pitch Modes as a Key for the Understanding of Phase Sequences and Types of Ordering in Antiferroelectric Smectic Liquid Crystals¹

M. Gorkunov*, S. Pikin*,**, and W. Haase**

**Shubnikov Institute of Crystallography, Russian Academy of Sciences, Leninskii pr. 59, Moscow, 117333 Russia*
e-mail: gorkunov@ns.crys.ras.ru

***Institut für Physikalische Chemie Technische Universität Darmstadt, 64287 Darmstadt, Germany*

Received June 2, 2000

A novel theoretical approach is suggested for the description of phase transitions and structures observed in antiferroelectric smectic liquid crystals. Allowance is made for two possible types of ordering: short-pitch and long-pitch helical modes. The thermodynamic behavior of the material is treated as a result of the competition between these two modes. The formulated theory reproduces the main features of the experimentally observed phase sequences and structures, thus explaining their physical nature. © 2000 MAIK “Nauka/Interperiodica”.

PACS numbers: 64.70.Md; 61.30.Cz; 77.84.Nh

1. The main features of phase transitions and macroscopic properties of antiferroelectric smectic liquid crystals have been intensively studied during the last decade. A huge amount of experimental data was recently contributed by the information on the structural details obtained in the experiments on resonance X-ray scattering [1, 2]. At the same time, there was no theoretical model, until now, which could describe both phase sequences and observed structures. Thus, e.g., the so-called “Ising-like” model [3] appears to explain the main features of the phase diagrams, but the predicted structures of the phases are in great discrepancy with the X-ray data [4, 5]. Another well-developed model, which is usually referred to as the “XY-model” [6], involves the short-pitch helical order, which is much more consistent with the X-ray data, but the theory seems to be unable to describe the corresponding phase transitions. Therefore, a great necessity for an appropriate theory still exists.

While creating such a theory, one should hope to explain the main features of the antiferroelectric smectics behavior in the temperature interval between the high-temperature nontilted smectic-A* phase and the low-temperature antiferroelectric phase (AF, where the neighboring layers are tilted in opposite directions), which can be formulated as the following:

—In the racemic mixtures, the phase sequence is quite simple, and by decreasing the temperature, the A phase transits to the nontwisted synclinic C phase (all the molecules there are tilted in the same direction), while the latter transits to the anticlinic phase (which is

the nonchiral analogue of the AF phase) at some lower temperature.

—In the chiral materials, more phases are observable. They arise in between the phases mentioned above and, according to the last experimental data, all have helical structures with an extremely short pitch [2].

—The phase that arises between the A* and C* phases, called usually the C_α^* phase, has a pitch that sufficiently changes with temperature, being much smaller than in the C* phase.

The ferrielectric phases that are located between the C* and AF phases have a pitch very close to some integer number of smectic layers. By decreasing the temperature, these phases change each other, so that the pitch decreases discretely (from 4 layers to 3 layers and finally to almost 2 layers in the twisted AF phase in the case observed in [1, 2]).

Below, we present a new approach that seems to account for all these main features, reproducing the observed phase sequences and structures. The main idea is to allow the substance to form two types of helical structures: a long-pitch helix with optical pitch and a short-pitch one with a pitch comparable to the smectic layer thickness. The idea of such an approach was first formulated in a semiphenomenological way in [4, 5, 7]. Here, we develop the idea in a different manner, taking into account that the physical background of these two modes can be connected, e.g., with the fact that inter-layer interactions, which lead to the appearance of antiferroelectric order, are likely to be determined by the interaction between chiral tails of the molecules [8]. Then, the molecules in neighboring layers, which are

¹This article was submitted by the authors in English.

arranged tail-to-tail, should tend to form a short-pitch structure, while the others are likely to form a long-pitch helix.

2. In general, the free energy density of the medium which is able to form both types of order, can be written with two order parameters:

$$F(\theta_L, \theta_S) = F_L(\theta_L) + F_S(\theta_S) + F_{LS}(\theta_L, \theta_S), \quad (1)$$

where θ_L and θ_S are the amplitudes (tilt angles) of the long-pitch and short-pitch modes, respectively; F_L and F_S are the free energies of the related individual modes; and F_{LS} is the contribution from the interaction of the modes. The phases of the system should possess the values θ_L and θ_S that minimize Eq. (1), and we can divide them into four classes: smectic-A phase, where both amplitudes are zero; L phases, where only θ_L is non-zero; S-phases, where θ_S is non-zero; and LS phases, in which both types of ordering are present simultaneously.

It is clear from the physical point of view that the LS phase is hardly probable in our case, at least when the pitches differ by a few orders of magnitude. Actually, it can take place, e.g., if the helices unwind each other, thus forming a common helix. The corresponding elastic energy of this unwinding should make such coexistence thermodynamically unprofitable. In the other hypothetical case, different areas of the substance can arrange structures with different pitches, but it would disturb the orientation (nematic) order within the layers, thus also being strongly unprofitable.

Therefore, the behavior of the system can be reduced to the competition between the L and S phases and the A phase. Then, at a given temperature the phase with the lowest free energy is stabilized. At temperatures when $F_L = F_S$, the first-order transitions between L and S phases occur. The closeness of the free energies should lead to the fluctuative appearance of the absent order parameter, which will be significant for our further consideration.

All intermolecular interactions in smectics can be divided into two parts: in-layer interactions between the molecules within the same layer and interlayer interactions between the molecules from different layers. We suppose the first ones to be mainly responsible for the tilting amplitude of the molecules and the appearance of ferroelectric polarization, while the interlayer interactions define the orientation of the tilting in different layers and the formation of the helices. It is established that the tilting amplitude is not affected by the transitions from one helical phase to another. Thus it is reasonable to assume that L and S modes differ only by interlayer contributions, and the in-layer part for both modes is the same.

In analyzing the interlayer contribution, we will follow the general approach of the XY-model [6], accounting only for the nearest neighbor interactions. It is convenient to present the director of the k th layer in

the form $\mathbf{n}_k = \mathbf{n}_z + \mathbf{c}_k$, where \mathbf{n}_z (the same for all layers) is parallel to crystalline axis z , and \mathbf{c}_k is the transversal part (C-director). Then the nonchiral quadratic in the θ part of the interaction between some n th and $(n + 1)$ th layers is proportional to

$$-n_z^2(\mathbf{c}_n \cdot \mathbf{c}_{n+1}) \approx -\theta^2 \cos \Psi, \quad (2)$$

where Ψ is the angle between the C-director of the layers and the minus sign reflects the fact that the synclinc ordering is preferable for this term. The chiral part should have the form

$$n_z^2((\mathbf{c}_n \times \mathbf{c}_{n+1}) \cdot \mathbf{e}) \approx -\theta^2 \sin \Psi, \quad (3)$$

where the unit vector \mathbf{e} points along the z axis in the direction of increasing layer number.

In addition to this, the specific anticlinic interaction responsible for the antiferroelectric ordering should be added. Following the results for the dipole-dipole interactions between the chiral tails [8], we assume it to have the form $\theta^4 \cos \Psi$, with some positive factor for the anticlinic order preferable here. Some chiral interaction like $\theta^4 \sin \Psi$ also should exist. We omit the possible terms with $\cos 2\Psi$ and $\sin 2\Psi$, because accounting for them will complicate further calculations but will bring nothing qualitatively new. Then the free energy of the short-pitch mode can be written as

$$F_S = t\theta_S^2 + \frac{1}{2}b\theta_S^4 - (V \cos \Psi + \alpha \sin \Psi)\theta_S^2 + (U \cos \Psi - \beta \sin \Psi)\theta_S^4, \quad (4)$$

where we introduce phenomenological parameters of the interlayer interaction: V and U for the nonchiral interaction and α and β for the chiral one. The in-layer part (the first pair of terms) is written in the ordinary form, the coefficient b being constant, and $t = A(T - T_0)$ is the only temperature-dependent coefficient.

In the free energy of the long pitch mode, which can be constructed in the same way, the anticlinic term should be absent. Unless a large value of the pitch means small values of the chiral parameters, we can neglect them and obtain

$$F_L = 1/2b\theta_L^4 + (t - V)\theta_L^2, \quad (5)$$

putting the same parameter of the synclinc interaction V .

3. Minimizing Eq. (5) with respect to θ_L , we obtain that the long-pitch phase can appear when $t < V$ and then

$$\theta_L^2 = -\frac{1}{b}(t - V), \quad F_L = -\frac{1}{2b}(t - V)^2. \quad (6)$$

Minimizing the free energy (4) with respect to Ψ , we obtain the condition

$$\tan \Psi = \frac{\alpha + \beta \theta_S^2}{V - U \theta_S^2}, \quad (7)$$

and with such Ψ , the free energy of the S-mode equals

$$F_S = 1/2b\theta_S^4 + t\theta_S^2 - \theta_S^2 \sqrt{(V - U\theta_S^2)^2 + (\alpha + \beta\theta_S^2)^2}. \quad (8)$$

In the vicinity of the phase transition from the A* phase, the tilt angle is small and can be neglected under the square root. Then we obtain the temperature of the transition from A* phase to S phase, the short-pitch mode tilt angle, and the free energy of the S phase as

$$t_{A \rightarrow S} = \sqrt{V^2 + \alpha^2}, \quad \theta_S^2 = -\frac{1}{b}(t - \sqrt{V^2 + \alpha^2}), \quad (9)$$

$$F_S = -\frac{1}{2b}(t - \sqrt{V^2 + \alpha^2})^2.$$

Comparison of Eqs. (6) and (9) gives that in this temperature range the S phase has lower free energy and appears first. So far, as one decreases the temperature, the transition from the A* phase to the S phase should be observed. We believe this corresponds to the so-called A*-C $_{\alpha}$ transition. It has second order, and its temperature $t_{A \rightarrow S}$ depends on chirality. According to Eq. (7), the pitch of the S phase decreases with decreasing temperature (with increasing θ_S^2), which is consistent with the results of the X-ray measurements [2].

Thus, in the closest vicinity of the transition point from the A* phase, the interlayer interactions significantly change the behavior of the tilt angle of the modes, shifting the transition point. With a further decrease in temperature, one reaches the temperature range $|t| \gg V$. Here, this interlayer contribution to tilting becomes small. Then we can set $\theta_S^2 = -t/b$ in Eq. (8) and obtain the free energy of the S phase as

$$F_S = -\frac{t^2}{2b} + \frac{t}{b} \sqrt{\left(V + U\frac{t}{b}\right)^2 + \left(\alpha - \beta\frac{t}{b}\right)^2}. \quad (10)$$

In the same approximation, the free energy of the L-phase equals

$$F_L = -\frac{t^2}{2b} + V\frac{t}{b}. \quad (11)$$

To analyze the phase transitions between the L and S phases, one should find the temperatures where these free energies are equal. It happens at temperatures

$$t_{S \leftrightarrow L} = -\frac{b}{U^2 + \beta^2} \times [UV - \alpha\beta \pm \sqrt{(UV - \alpha\beta)^2 - \alpha^2(U^2 + \beta^2)}], \quad (12)$$

the minus sign before the square root corresponding to S \rightarrow L transition and the plus sign corresponding to the L \rightarrow S transition, as far as the temperature decreases. Therefore the L phase appears in the interval between the temperatures (12). We believe this L phase

describes the C* phase in the observed phase sequences. The condition for C* phase appearance can be obtained as a requirement of the square root's presence in Eq. (12), and it takes the form

$$V > \alpha[\sqrt{1 + (\beta/U)^2} + \beta/U]. \quad (13)$$

As a consequence of Eqs. (12) and (13), we see so far that the C* phase interval becomes narrower when the chirality increases and even disappears at large values of the chiral parameters.

As a result, we find that, by starting from the A* phase and decreasing the temperature, the transition to the C $_{\alpha}$ phase at point $t_{A \rightarrow S}$ takes place first. Afterwards, the transition to the C* phase appears at temperature given by Eq. (12) with the minus sign. Finally, the transition back to some S phase occurs at temperature (12) with the plus sign.

4. To analyze the S phase, which occurs below the C* phase, one should account for the fact that the free energies of both types of order are very close, differing only by the contributions from the interlayer interactions. Then the L-order can appear fluctuatively in the S phase. If the characteristic times of such fluctuations are longer than the short-pitch helix relaxation times, then this phenomena is locally similar to the action of some external vectorlike field on the short-pitch helix perpendicular to the helical axis.

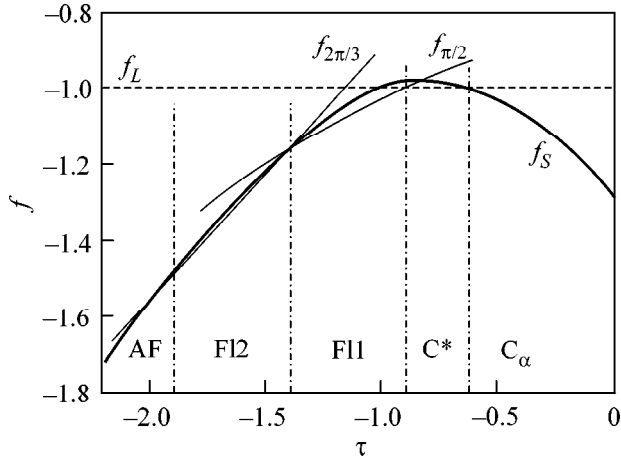
The free energy of the short-pitch mode (4) under the action of the external vector field \mathbf{L} should include the field-dependent terms. The interaction of some n th layer with the field can be represented as a sum of terms proportional to the powers of the product $(\mathbf{L} \cdot \mathbf{c}_n)$. The corresponding contribution from all layers to the free energy density can be reduced to

$$\Delta F_S = \frac{1}{N} \sum_{k=1}^{\infty} \sum_{n=1}^N u_k \cos[k(\Psi n + \varepsilon - \varphi)], \quad (14)$$

where φ is the azimuth angle of the field, ε is the phase of the short-pitch helix, and N is a macroscopic number of smectic layers. The coefficients $u_k \propto L^k \theta_S^k$ phenomenologically characterize the interaction energy.

After the summation over n , Eq. (14) appears to have a singular dependence on Ψ , being nonzero only if $\Psi = 2\pi s/k$ with integer s and k . After minimization over the phase ε , we obtain it to be equal to φ or $\varphi + \pi/k$, depending on the sign of the corresponding constant u_k and therefore providing the negative sign of the contribution to the free energy. Then the free energy contains "locking" terms that make the commensurate structure profitable. The corresponding full energies of such commensurate states are, for instance,

$$F_{\pi/2} = -\frac{t^2}{2b} - \frac{t}{b} \left(\beta \frac{t}{b} - \alpha \right) - |u_4| \quad (15)$$



Reduced free energies of the long-pitch state (f_L), incommensurate short-pitch state (f_S), and commensurate states ($f_{\pi/2}$ and $f_{2\pi/3}$) as functions of the dimensionless temperature τ . Phase transitions occur at the intersections of the lowest curves. Corresponding phases are indicated underneath.

for the 4-layered structure and

$$F_{2\pi/3} = -\frac{t^2}{2b} - \frac{t}{2b} \left[\frac{t}{b} (U + \beta\sqrt{3}) + (V - \alpha\sqrt{3}) \right] - |u_3| \quad (16)$$

for the 3-layered one. The interaction parameters of the lowest order are presented here, since u_k should decrease as k increases. It is also clear that these parameters have sufficient temperature dependence, since the amplitude of L-fluctuations decreases vastly as the difference ($F_L - F_S$) increases. These locking terms make the commensurate structure profitable compared to the incommensurate one, as free energies (15) and (16) are less than incommensurate energy (10) in certain temperature intervals near the points at which Ψ defined by Eq. (7) is close to the values $\pi/2$ and $2\pi/3$, respectively.

We can suggest that the ferrielectric-like electrooptic behavior occurs as a result of L-order induction by the electric field. Thus, following the notations confirmed in the literature, we denote our 4-layered phase as FI1 and the 3-layered one as FI2. Obviously, in general, such locking occurs every time the ratio $\Psi/2\pi$ equals any rational number s/k . The value of the corresponding locking energy then equals $|u_k|$, which is comparably small at large k , so that the phases with small k have a much wider temperature range.

At temperatures below the regions of the commensurate phases, the incommensurate pitch of the S-structure is slightly larger than 2-layers, what means that it corresponds to the twisted antiferroelectric phase. With a further temperature decrease, the short pitch also decreases, approaching 2-layers asymptotically. This means that, effectively, the pitch of the AF phase twist-

ing increases as the temperature goes down, which was clearly seen experimentally by means of optical selective reflections [9, 10]. The twisting sign of the antiferroelectric helix is opposite compared to the ferroelectric one.

To analyze the phase sequence, it is convenient to compare the reduced dimensionless free energies $f = (F + t^2/2b)/V\theta^2$. Thus, for the L phase this reduced energy equals $f_L = -1$; the reduced energies of the commensurate states $f_{\pi/2}$ and $f_{2\pi/3}$, according to Eqs. (15), (16), possess almost linear temperature dependence, as only the locking terms give small nonlinear contributions. The corresponding analysis of the phase sequence is illustrated in the figure, where the typical reduced free energies of the states are presented as functions of the dimensionless temperature $\tau = tU/bV$. The system follows the lowest possible curve, and the transitions occur at intersection points. The arising phases are indicated underneath.

The small incommensurability of the FI phases that was observed in the X-ray experiments can arise due to the twisting of the L-field. The finite size of the fluctuating areas should widen the δ -function-like dependence of the Eq. (14), making it Lorentzian-like. This can also give rise to the incommensurability, which will be temperature-dependent in this case.

5. Our approach reproduces the main features of phase sequences and structures observed in antiferroelectric smectics. It can also be used for the description of nonchiral (racemic) mixtures. As we set α and β to zero values, the S-state describes synclinic order above the temperature $t = -bV/U$ and anticlinic order below it. From Eqs. (9), (12), it follows that in a racemate the temperature range of the C_α phase vanishes completely and the A phase transits directly to the C phase. The transition to the S phase given by Eq. (12) then happens at the point $t = -2bV/U$, i.e., at the point where the S mode already forms an anticlinic structure. So far, the last transition corresponds to the C–AF one in the racemate.

As a conclusion, we can make some estimations of the involved parameters for the substance 10OTBBB1M7, which was thoroughly studied by both X-ray [2] and optical [11] techniques. As was found, the S-pitch in the C_α phase in this compound varies monotonically from about 8 layers close to the A* phase up to 5 layers near the C* phase. The 8-layer periodicity means the value $\Psi \approx \pi/4$ when $\theta_S \rightarrow 0$, and according to Eq. (7), it yields $V \approx \alpha$. So far, for the S-mode the chiral interlayer interactions in this case are of the same order as the nonchiral ones. Certainly, it does not necessarily mean that the substance possesses anomalously high chirality. It is more likely to be the consequence of the low value of the parameter V , which can be treated as a result of some anticlinic contribution to the corresponding quadratic in θ term in Eq. (4).

For $V \approx \alpha$, our approach predicts the narrow temperature range of the C* phase, which is consistent with the

observed phase sequence [2, 11], where this range is only about 1°C. From its low temperature side, the C* phase bounds the 4-layered FI1-phase. Unless the latter appears near the temperature for which the incommensurate S-pitch equals 4 layers, above the upper edge of the C* phase this pitch should be slightly larger, i.e., about 5 layers. This is consistent with the 5-layer structure of the C_α phase observed before the transition to C*.

Obviously, to fit the whole phase sequence one must know the temperature behavior of the locking parameters u_k . These parameters must decrease strongly as the difference ($F_L - F_S$) grows, being larger near the L-S-transition point. This means that the locking in the FI1 phase, which neighbors the L-phase, is stronger than that in the FI2 phase. That is why the temperature interval of the FI2 phase is smaller. This can also explain why the structure of the FI1 phase is rather well stabilized compared to the FI2 structure, which is quite unstable, giving the low-accuracy experimental data.

Financial support from the Deutsche Forschungsgemeinschaft (Ha 782/39-2 and the bilateral program Ha 782/49-2) and from the Russian Foundation for Basic Research (Grant no. 00-02-17801) are acknowledged. S.P. acknowledges the receipt of the research award of the Alexander von Humboldt-Stiftung.

REFERENCES

1. P. Mach, R. Pindak, A.-M. Levelut, *et al.*, Phys. Rev. Lett. **81**, 1015 (1998).
2. P. Mach, R. Pindak, A.-M. Levelut, *et al.*, Phys. Rev. E **60**, 6793 (1999).
3. A. Fukuda, Y. Takanishi, T. Isozaki, *et al.*, J. Mater. Chem. **4**, 997 (1994).
4. M. Gorkunov, S. Pikin, and W. Haase, Pis'ma Zh. Éksp. Teor. Fiz. **69**, 227 (1999) [JETP Lett. **69**, 243 (1999)].
5. S. Pikin, M. Gorkunov, D. Kilian, and W. Haase, Liq. Cryst. **26**, 1107 (1999).
6. M. Cepic and B. Zeks, Mol. Cryst. Liq. Cryst. **263**, 61 (1995).
7. S. A. Pikin, S. Hiller, and W. Haase, Mol. Cryst. Liq. Cryst. **262**, 425 (1995).
8. M. Osipov and A. Fukuda, Phys. Rev. E (in press).
9. K. Miyachi, Y. Takanishi, K. Ishikawa, *et al.*, Ferroelectrics **149**, 61 (1993).
10. T. Akizuki, K. Miyachi, Y. Takanishi, *et al.*, Jpn. J. Appl. Phys. **38**, 4832 (1999).
11. I. Mousevich, M. Skarabot, M. Conradi, *et al.*, in *Proceedings of the VIII International Topical Meeting on the Optics of Liquid Crystals, Puerto Rico, 1999*, Mol. Cryst. Liq. Cryst. (in press).

Low-Frequency Raman Scattering in the Orientationally Disordered Phase of a C₆₀ Crystal

V. K. Malinovskii*, N. V. Surovtsev, and A. P. Shebanin**

*Institute of Automatics and Electrometry, Siberian Division, Russian Academy of Sciences,
Universitetskii pr. 1, Novosibirsk, 630090 Russia*
* e-mail: malinovsky@iae.nsk.su

** *Joint Institute of Geology, Geophysics, and Mineralogy, Siberian Division, Russian Academy of Sciences,
Universitetskii pr. 3, Novosibirsk, 630090 Russia*

Received June 2, 2000

Low-frequency (3–120 cm⁻¹) Raman scattering in the orientationally disordered phase and the photopolymerized state of fullerite was investigated. Experimental data suggest that, by analogy with scattering in disordered media (glasses), the low-frequency spectra can be described in terms of scattering by the localized vibrational states. © 2000 MAIK “Nauka/Interperiodica”.

PACS numbers: 61.48.+c; 78.30.Na; 63.20.-e

A molecular crystal composed of fullerene molecules C₆₀ (fullerite) is a rather unusual object for solid-state physics. At room temperature, fullerite is a special case of plastic crystals. The fullerene molecules undergo rotation in the fcc lattice sites. The sphericity of the molecule and the weak intermolecular interaction differentiate fullerite from the majority of other plastic crystals, where the molecules tend to be planar and the intermolecular interaction is strongly anisotropic. The specific features of fullerite have generated great scientific interest in it, both as an object for fundamental research and in the search for unusual properties that can find technological uses.

Raman scattering is widely used in studying fullerite. However, most Raman studies were aimed at investigating the intramolecular vibrations with frequencies higher than 100 cm⁻¹ (see e.g., [1, 2]). The works devoted to low-frequency (<100 cm⁻¹) Raman studies of fullerite are, in fact, lacking. The study of low-frequency Raman scattering in plastic crystals with unusual properties, to which fullerite belongs, is a highly topical problem and of interest for the understanding of its vibrational and relaxation dynamics. In [3], the low-frequency Raman spectra of crystalline C₆₀ were examined to reveal the librational modes in the orientationally ordered fullerite phase ($T < 260$ K). The spectrum of orientationally disordered fullerite was treated in [3] as a “Lorentzian background, indicative of scattering due to the isotropic rotation of the C₆₀ molecules.” However, it is shown below that this interpretation of the Raman spectra is contradictory to the NMR data.

It is the purpose of this work to elucidate the origin of the low-frequency Raman spectrum of a high-temperature fullerite phase. Low-frequency (3–120 cm⁻¹)

Raman scattering in fullerite is experimentally studied for the orientationally disordered phase and the photopolymerized state. The low-frequency Raman spectrum is interpreted as a spectrum caused by scattering from the localized vibrational states, by analogy with the scattering in disordered media; and it is shown that this spectrum is not associated with scattering by the rotations of the C₆₀ molecules.

We studied polycrystalline C₆₀ films with surfaces of good optical quality fabricated at the Institute of Organic Chemistry, Siberian Division, Russian Academy of Sciences. The Raman spectra were measured for samples placed in a vacuum chamber. The spectra were recorded on a U1000 spectrometer with excitation by the 514-nm argon laser line. The spectra were recorded in a 90°-scattering scheme (for exterior angle), and the electric field vector lay in the plane of incidence. Grazing incidence of laser radiation on the films was used (~80° from the normal to the surface). The typical slit width of the spectrometer was 1.5 cm⁻¹. The spectral ranges 3–120 cm⁻¹ and 1100–1600 cm⁻¹ were examined.

It is known that illumination of the C₆₀ crystal by a wavelength shorter than 650 nm can induce photopolymerization in a sample. The photopolymerization rate strongly depends on the intensity of the irradiating light. In the Raman scattering experiments, the sample state can be monitored by the Raman spectra in the range 1400–1500 cm⁻¹, because the initial C₆₀ is characterized by a peak at 1470 cm⁻¹, while the photopolymerized sample shows a maximum at 1460 cm⁻¹ [4]. Possible photopolymerization during the course of the experiment was monitored by recording the high-frequency spectra (1440–1480 cm⁻¹) before and after the

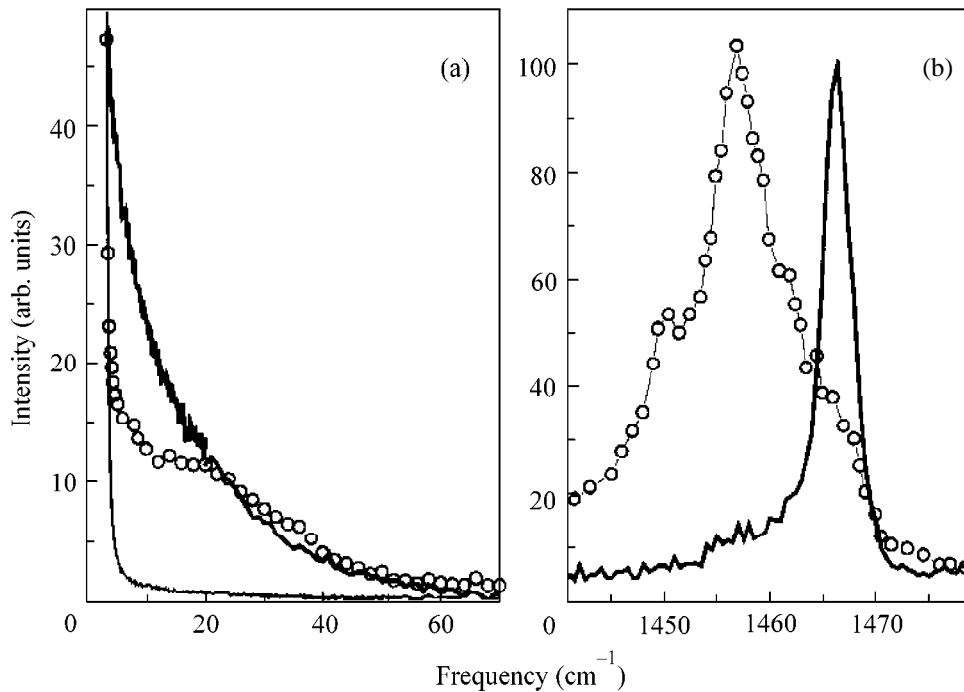


Fig. 1. (a) Low-frequency and (b) high-frequency spectra. Solid line is for the fullerite, and circles are for the PP fullerite. The thin line in Fig. 1a corresponds to the instrumental contour of elastic light scattering.

low-frequency Raman spectra were measured. We found that no detectable phototransformation occurs while measuring the low-frequency spectra at a low excitation level ($\sim 1 \text{ W/cm}^2$). In what follows, by the term “fullerite” we mean a sample measured at low laser intensity, as distinct from the photopolymerized (PP) fullerenes, i.e., samples obtained after prolonged illumination with intensity $> 10 \text{ W/cm}^2$.

Figure 1 shows the low- and high-frequency spectra of the fullerite and the PP fullerite. The spectrometer background caused by elastic scattering of laser radiation from a rough surface is shown in the same figure. The spectra are normalized to the scattering intensity at 3 cm^{-1} , where the contribution from the instrumental wing of the elastic line dominates in all spectra. It is seen from a comparison of the “spectrum” of the elastic line with the film spectra that the experimental data are trustworthy starting at frequencies near 5 cm^{-1} . Fig. 1 allows the conclusion to be drawn that, in addition to the changes in the high-frequency Raman spectrum, photopolymerization also induces changes in the low-frequency spectrum. (This fact was also used for monitoring the absence of photopolymerization during the accumulation of the low-frequency spectra).

The photopolymerization process is accompanied by linking of the fullerene molecules by covalent bonds in random directions. Because of the disorder in the polymerizing covalent bonds between the fullerene molecules, one can expect that the low-frequency spectrum of the PP fullerite resembles, in many respects, the spectra of amorphous polymers.

The low-frequency Raman spectra in Fig. 2 are given in the so-called reduced representation as functions of the reduced intensity $I_R = I/(n+1)$, where I is the Raman intensity, $n = 1/\exp(\hbar\omega/kT)$ is the Bose factor, and ω is the change in the scattered light frequency. For comparison, the spectrum of poly(methyl methacrylate) (PMMA, taken from [5]) is also shown in Fig. 2. This spectrum was normalized to the frequency of a maximum in the spectrum of the PP fullerite, for which reason it was compressed by a factor of 3.2. The spectra of the amorphous polymer and the PP fullerite show a good qualitative similarity. The maximum in the reduced spectrum of a polymer usually corresponds to the edge of its acoustic spectrum. The edge of the acoustic spectrum of a polymer is determined by the localization of vibrational excitations on the monomers. When the spectrum of the PP fullerite is considered as a full analogue to the spectra of classical polymers, an independent estimate can be obtained of how many times the experimental spectrum of PMMA should be compressed for the maxima of the reduced PMMA spectra and the spectrum of the PP fullerene to coincide. The size of a monomer in the PP fullerite can be estimated as a distance of $\sim 1 \text{ nm}$ to the nearest neighbor in the fcc lattice, while the size of the PMMA monomer along the polymer chain is $\sim 0.31 \text{ nm}$; the longitudinal and transverse sound velocities in fullerite are 3.3 and 1.7 km/s , respectively [6], and coincide with the sound velocity in PMMA. From these data, it is expected that the compression factor is approximately 3, in nice agreement with the factor used in Fig. 2. There-

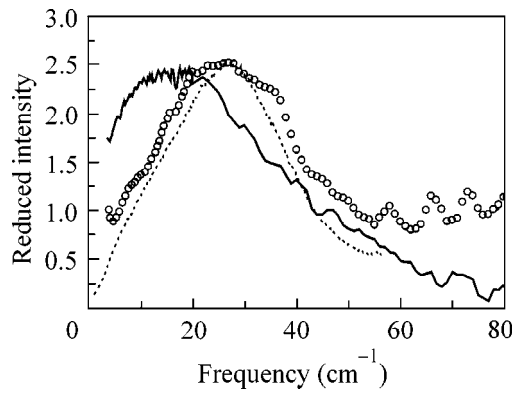


Fig. 2. Reduced low-frequency spectrum $I_R = I/(n + 1)$. Solid line is for the fullerite, and circles are for the PP fullerite. Dotted line corresponds to the PMMA spectrum compressed by a factor of 3.2.

fore, apart from the qualitative correlation between the spectra, there is a good quantitative agreement between the edge of the acoustic spectrum in the PP fullerite and a conventional polymer. This result is nontrivial, because conventional polymers are amorphous, whereas the centers of the molecules in the PP fullerite are positioned in the lattice sites.

Whereas the interpretation of the low-frequency Raman spectrum of PP fullerite has a good intuitive basis, the origin of the low-frequency spectrum in fullerite is less clear. It was suggested in [3] that the low-frequency Raman spectrum of fullerite is due to scattering by the isotropically rotating C_{60} molecules. In this case, the intensity maximum is determined by the molecular rotation time. In [7], the reorientation dynamics of molecules in the fullerite were measured by the NMR technique. The value of $\tau = 12$ ps obtained for the reorientation time [in the expression $F(t) \propto \exp(t/\tau)$ for the reorientational correlation function] at room temperature corresponds to an intensity maximum at 0.44 cm^{-1} . A comparison of the intensity maximum in Fig. 2 with the NMR data indicates that molecular rotation cannot be responsible for the low-frequency spectrum in the frequency range of interest. Additional information can be obtained from an analysis of the spectral shape for the reduced intensity. For scattering by rotating molecules, the spectrum should be described by the reduced Lorentzian contour $I_R \propto \omega/(1 + (\omega/\gamma)^2)$ with a maximum at γ . The experimental spectrum is compared with the Lorentzian contour in Fig. 3. The discrepancy between the experimental spectrum and the analytical curve is clearly seen. The spectrum measured in [3] at a temperature of 259 K is also shown in Fig. 3 (for convenience, it is normalized to the maximum frequency). It is clear from Fig. 3 that the data in [3] are also contradictory to the Lorentzian description of the spectrum. Moreover, the fact that the high-frequency portion of the spectrum in Fig. 3 decreases faster than the Lorentzian curve allows the

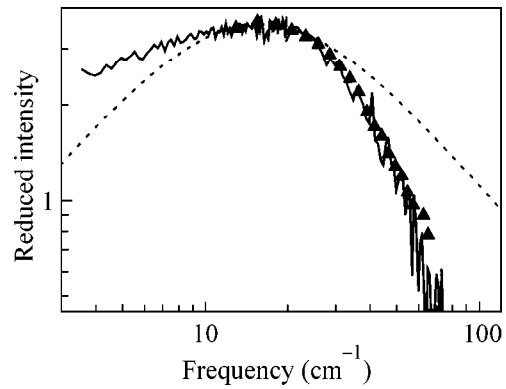


Fig. 3. Reduced low-frequency spectrum of the fullerite at room temperature (solid line). Triangles are for the spectrum at $T = 259$ K (from [3]). Dotted line is for the reduced Lorentzian contour.

conclusion to be drawn that the experimental spectrum can be described by none of the relaxation time distributions. This follows from the fact that each relaxation time generates a Lorentzian contour, while their sum cannot decrease with frequency faster than each one of them.

An alternative explanation for the low-frequency spectrum consists in its interpretation as a vibrational spectrum of a disordered medium (the so-called boson peak [8]). The low-frequency spectra of disordered media are characterized by an excess of the density of vibrational states. Raman scattering from acoustic modes is allowed in disordered media because of vibration localization on a nanometer scale [8]. The Shuker–Gammon formula [9] relates the density $g(\omega)$ of vibrational states in a disordered medium to the Raman intensity through the coupling coefficient $C(\omega)$:

$$I(\omega) = C(\omega)g(\omega)\frac{n+1}{\omega}.$$

The frequency dependence of $C(\omega)$ can be determined from a comparison of the density of vibrational states with the Raman spectra. For the vibrational states in glasses, it depends linearly on frequency [10].

The coupling coefficient $C(\omega)$ for fullerite is illustrated in Fig. 4. It was obtained from the comparison of the Raman spectra with the data on the density of vibrational states measured in [11] by inelastic neutron scattering. One can see in Fig. 4 that the coupling coefficient is far from being constant, as is expected for the relaxational spectrum (see, e.g., [12]), but can be fitted by a linear law, as in ordinary glasses [10]. Thus, the frequency behavior of $C(\omega)$ is also evidence that the low-frequency Raman spectra observed for fullerite are due to scattering by vibrational excitations following the pattern seen in inelastic light scattering in disordered media (glasses).

Let us now discuss the origin of the low-frequency Raman spectrum in fullerite. It is formed in circum-

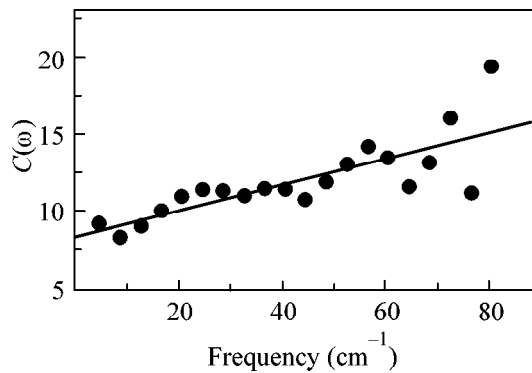


Fig. 4. The $C(\omega)$ coefficient and its linear approximation.

stances where the characteristic times of molecular rotation are appreciably longer than the period of acoustic vibrations (as follows from the NMR data; see above). In such a situation, an acoustic phonon propagates through a medium with the “frozen” random mutual orientations of fullerene molecules. The interaction energy of the neighboring molecules strongly depends on the mutual orientation, leading to large local fluctuations of the elastic constants. It was recently shown [13] by numerical simulation that the scatter of the elastic constants of intermolecular interaction gives rise to a boson peak even if the atomic positions are ordered in a crystal. Our data can be considered as an experimental implementation of such a possibility. The distinguishing feature of fullerite is that the fluctuations of the elastic constants are dynamic and disappear upon time averaging.

In summary, the low-frequency Raman spectra of fullerite in its orientationally disordered phase and the photopolymerized state are experimentally studied in this work. The analysis has shown that these spectra are not purely relaxational and, moreover, cannot be rationalized in terms of light scattering by isotropic molecular rotations. The low-frequency spectra are interpreted as being due to scattering by the vibrational states in media that are inhomogeneous on the nanometer scale, by analogy with the low-frequency scattering in glasses. The spectrum of the photopolymerized fullerite is shown to qualitatively correspond to the

spectra of conventional polymers, and quantitative agreement is obtained between the positions of the edges of acoustic spectra in these media.

We are grateful to A.V. Okotrub and Yu.V. Shevtsov for the preparation of the fullerite films used in this work. This work was supported by the program “Fullerenes and Atomic Clusters” (project no. 5-4-99), the Russian Foundation for Basic Research (project no. 99-02-16697), and the grant of the Siberian Division of Russian Academy of Sciences for young scientists (N.V. Surovtsev).

REFERENCES

1. P. J. Horoyski, M. L. W. Thewalt, and T. R. Anthony, *Phys. Rev. B* **54**, 920 (1996).
2. P. H. M. van Loosdrecht, P. J. M. van Bentum, and G. Meijer, *Phys. Rev. Lett.* **68**, 1176 (1992).
3. P. J. Horoyski and M. L. W. Thewalt, *Phys. Rev. B* **48**, 11446 (1993).
4. T. Wägberg, P. Jacobsson, and B. Sundqvist, *Phys. Rev. B* **60**, 4535 (1999).
5. N. V. Surovtsev, A. Mermet, E. Duval, and V. N. Novikov, *J. Chem. Phys.* **104**, 6818 (1996).
6. N. P. Kobelev, R. K. Nikolaev, Ya. M. Soifer, and S. S. Khasanov, *Fiz. Tverd. Tela (St. Petersburg)* **40**, 173 (1998) [*Phys. Solid State* **40**, 154 (1998)].
7. R. Tycko, G. Dabbagh, R. M. Fleming, *et al.*, *Phys. Rev. Lett.* **67**, 1886 (1991).
8. J. Jäckle, in *Amorphous Solids: Low-Temperature Properties*, Ed. by W. A. Phillips (Springer-Verlag, Berlin, 1981), p.135.
9. R. Shuker and R. W. Gammon, *Phys. Rev. Lett.* **25**, 222 (1970).
10. A. Fontana, R. Dell’Anna, M. Montagna, *et al.*, *Europhys. Lett.* **47**, 56 (1999).
11. B. Renker, F. Gompf, H. Schober, *et al.*, *J. Supercond.* **7**, 647 (1994).
12. A. P. Sokolov, U. Buchenau, W. Steffen, *et al.*, *Phys. Rev. B* **52**, R9815 (1995).
13. W. Schirmacher, G. Diezemann, and G. Ganter, *Phys. Rev. Lett.* **81**, 136 (1998).

Translated by V. Sakun

Broadening of the Specific Heat Jump in Three-Dimensional Superconductors

I. A. Fomin

Kapitsa Institute for Physical Problems, Russian Academy of Sciences, ul. Kosygina 2, Moscow, 117973 Russia

Received June 9, 2000

The Ginzburg–Landau theory is used to calculate perturbatively the influence of stochastic inhomogeneities on the smearing of the specific heat jump in three-dimensional superconductors. The small-scale and large-scale (compared to the correlation length) inhomogeneities are simultaneously taken into account to derive a finite and continuous (in the vicinity of T_c) expression for the temperature dependence of the superconductor specific heat. © 2000 MAIK “Nauka/Interperiodica”.

PACS numbers: 74.25.Bt; 74.70.Tx; 74.62.Dh

1. The transition of ideal homogeneous metals to the superconducting state is accompanied by a sharp [vertical in the $C(T)$ graph] jump in specific heat. In the presence of inhomogeneities, the jump is smeared out [1, 2]. The investigations of strongly anisotropic and unconventional high- T_c and heavy-fermion superconductors have renewed interest in the description of jump smearing [3, 4]. This work was stimulated by the experimental study of the influence of defects on the sharpness of the superconducting transition in the heavy-fermion UPt₃ compound [5, 6]. The magnetic and nonmagnetic impurities both reduce the superconducting transition temperature T_c in compounds with unconventional pairing, with the T_c decrease being proportional to the impurity concentration [7]. The spatial fluctuations of the impurity concentration give rise to a change in the local transition temperature $T_c(\mathbf{r})$. The influence of these fluctuations on the temperature dependence of the specific heat near T_c depends on whether the fluctuations of $T_c(\mathbf{r})$ are large- or small-scale compared to the correlation length $\xi(T)$. As $T \rightarrow T_c$, the correlation length $\xi \rightarrow \infty$. The temperature fluctuation amplitude δT is the natural cutoff parameter, and the fluctuations can be considered large-scale if their spatial scale is larger than $\xi(\delta T)$. The large-scale variations may be due, in particular, to the macroscopic inhomogeneity of a sample. In what follows, it is assumed that there are no such inhomogeneities in the samples.

The small-scale fluctuations introduce a correction term into the expression for specific heat at $T < T_c$. Since this term diverges as $T \rightarrow T_c$ [1], the formula derived in [1] can only account for the “tail” of the fluctuation correction to the specific heat at $T < T_c$. Although the asymptotic form of the correction at $T > T_c$ was found in [2], the formula describing the behavior of the specific heat in the vicinity of T_c and matching both asymptotic expressions is as yet lacking. In this work, the influence of both large- and small-scale $T_c(\mathbf{r})$

fluctuations on the specific heat near T_c is taken into account for the case when the fluctuations are small. The $C(T)$ dependence in the three-dimensional case is described by a finite and continuous function depending on the stochastic properties of a random function $T_c(\mathbf{r})$. Note that by T_c is meant the average transition temperature, in the vicinity of which the specific heat suffers major changes. The true transition temperature corresponding to the formation, for the first time, of an infinite cluster of superconducting domains falls within the “high-temperature tail” (see [2]). The singularity of the specific heat at this temperature cannot be described within the framework of perturbation theory.

2. To simplify the treatment, let us consider a superconductor with a one-component order parameter. The starting mathematics for this case is a slightly modified copy of an appropriate part of [1]. The Ginzburg–Landau functional is written as

$$F_s - F_n = v \int \left\{ \frac{T - T_c}{T} |\psi|^2 + \frac{1}{2} B |\psi|^4 + c |\nabla \psi|^2 \right\} dv, \quad (1)$$

where v is the density of states. The jump in specific heat per unit volume is expressed through the derivative of the average order parameter

$$C_s - C_n = -v \frac{\partial}{\partial T} \left(\frac{1}{v} \int |\psi|^2 dv \right). \quad (2)$$

The smearing of the specific heat jump is mainly due to the fluctuations of the coefficient of $|\psi|^2$ in expansion (1). This coefficient can conveniently be written as

$$\frac{T - T_c}{T} = \frac{T - \langle T_c \rangle}{T} + \frac{\langle T_c \rangle - T_c(\mathbf{r})}{T} \equiv \tau + \zeta(\mathbf{r}), \quad (3)$$

where $\langle T_c \rangle$ is the mean transition temperature and $\zeta(\mathbf{r})$ is a random function belonging to the ensemble with

$\langle \zeta(\mathbf{r}) \rangle = 0$ and the correlation function

$$\phi(\mathbf{r} - \mathbf{r}') = \langle \zeta(\mathbf{r})\zeta(\mathbf{r}') \rangle. \quad (4)$$

In this equation and in what follows, the angular brackets stand for the ensemble averages. In the notations adopted, the Ginzburg–Landau equation for the functional (1) is written as

$$\tau\psi + B\psi|\psi|^2 - \nabla(c\nabla\psi) = -\zeta(\mathbf{r})\psi. \quad (5)$$

The ψ function is assumed to be real in the absence of a magnetic field. The spatially inhomogeneous solution arises because of the random field $\zeta(\mathbf{r})$, which is taken to be a small perturbation (the appropriate criterion will be formulated later). The spatial scale of the $\zeta(\mathbf{r})$ field is on the order of $\xi_0 = \hbar v_f / T_c$. To first order in $\zeta(\mathbf{r})$, the scale of the additional term in the expression for the order parameter is the same. The spectral density of the $\zeta(\mathbf{r})$ fluctuation in the \mathbf{k} space rapidly decreases with a decrease in \mathbf{k} (increase in the spatial scale). Simple estimation shows that the first-order corrections can be considered small-scale over the whole temperature range, except in a negligibly small vicinity of T_c . The second-order corrections contain a sizable large-scale component because of the compensation for the spatial dependence in the products of Fourier components with opposite wave vectors. With these large-scale corrections in mind, let us introduce the characteristic scale θ for jump smearing caused by large-scale corrections and the corresponding spatial scale $\xi_\theta = \xi_0 / \sqrt{\theta}$. The sample size L is assumed to be large enough for the condition $\xi_0 \ll \xi_\theta \ll L$ to be satisfied. The relation of θ to the properties of the $\zeta(\mathbf{r})$ function will be clarified in the course of the calculations. Let us seek the solution of Eq. (5) in the form $\psi = \bar{\psi}(1 + \chi)$, where the amplitude $\bar{\psi}$ is a smooth function, while the addition χ accounts for the small-scale variations. To make the separation unequivocal, let us require that $\bar{\chi} = 0$. The bar stands for averaging over the scale of order ξ_θ . To second order in $\zeta(\mathbf{r})$ and χ , Eq. (5) takes the form

$$\begin{aligned} \tau\bar{\psi}(1 + \chi) + B\bar{\psi}^3(1 + 3\chi + 3\chi^2) \\ - c[\bar{\psi}\Delta\chi + 2\nabla\bar{\psi}\nabla\chi + (1 + \chi)\Delta\bar{\psi}] = -\zeta\bar{\psi}(1 + \chi). \end{aligned} \quad (6)$$

Averaging of Eq. (6) over the $\sim\xi_\theta$ scale yields

$$c\Delta\bar{\psi} = \tau\bar{\psi} + B\bar{\psi}^3(1 + 3\bar{\chi}^2) + \bar{\psi}\overline{\zeta(\mathbf{r})\chi(\mathbf{r})}. \quad (7)$$

The local transition temperature, defined as the temperature for which $\bar{\psi} = 0$, is shifted from its average position by (cf. [1])

$$\tau_0 = -\overline{\zeta(\mathbf{r})\chi(\mathbf{r})}|_{\bar{\psi}=0}. \quad (8)$$

Setting $t = \tau - \tau_0$ in Eq. (7), one can recast it as

$$c\Delta\bar{\psi} = t\bar{\psi} + B\bar{\psi}^3(1 + 3\bar{\chi}^2) + (\tau_0 + \overline{\zeta(\mathbf{r})\chi(\mathbf{r})})\bar{\psi}. \quad (9)$$

To evaluate $\overline{\zeta\chi}$ and $\bar{\chi}^2$, the equation for the rapidly varying terms linear in $\zeta(\mathbf{r})$ and $\chi(\mathbf{r})$,

$$t\chi + 3B\bar{\psi}^2\chi - c\Delta\chi = -\zeta(\mathbf{r}), \quad (10)$$

should be solved for $\chi(\mathbf{r})$. This can be done, e.g., by taking Fourier transforms:

$$\zeta_{\mathbf{k}} = \int \zeta(\mathbf{r})e^{-i\mathbf{k}\mathbf{r}} d^3r; \quad \chi_{\mathbf{k}} = \int \chi(\mathbf{r})e^{-i\mathbf{k}\mathbf{r}} d^3r.$$

The result is

$$\tau_0 = \int \frac{d^3k}{(2\pi)^3} \frac{\zeta_{\mathbf{k}}\zeta_{-\mathbf{k}}}{ck^2}. \quad (11)$$

To connect τ_0 with the stochastic properties of the $\zeta(\mathbf{r})$ ensemble, let us consider the Schrödinger equation for a particle with mass $m = \hbar^2/2c$ moving in the potential $\zeta(\mathbf{r})$,

$$-c\Delta\psi + \zeta(\mathbf{r})\psi = \varepsilon\psi, \quad (12)$$

and assume that $\zeta(\mathbf{r})$ is a perturbation [8]. The τ_0 shift coincides, to a sign, with the leading correction ε_0 to the $\varepsilon = 0$ eigenvalue. The potential ensemble $\zeta(\mathbf{r})$ generates “shift density” $g(\varepsilon_0)$ which, by definition, is connected with the density of states $\rho(\varepsilon)$ on the $d\varepsilon$ interval by the relationship

$$\rho(\varepsilon) = \frac{1}{4\pi^2 c^{3/2}} \int_{-\infty}^{\varepsilon} g(\varepsilon_0) \sqrt{\varepsilon - \varepsilon_0} d\varepsilon_0. \quad (13)$$

This is a standard integral equation for $g(\varepsilon_0) \equiv g(x)$. Its solution can be written in the form

$$g(x) = 2\pi c^{3/2} \int_{-\infty}^x \frac{\rho''(z) dz}{\sqrt{x-z}}, \quad (14)$$

where the prime denotes differentiation. At present, an extensive literature is devoted to studying the density of states for the Schrödinger equation with a random potential (for bibliography, see [9]). Expression (14) allows the desired shift density $g(x)$ to be determined from the known density of states $\rho(\varepsilon)$. The $\Delta\tau_0$ interval, in which the function $g(-\tau_0)$ is essentially nonzero, is precisely the one that plays the role of jump smearing θ introduced above. For the other averages in Eq. (9), one has

$$\begin{aligned} \overline{\zeta(\mathbf{r})\chi(\mathbf{r})} + \tau_0 &= -2t \int \frac{d^3k}{(2\pi)^3} \frac{\zeta_{\mathbf{k}}\zeta_{-\mathbf{k}}}{ck^2(ck^2 - 2t)}; \\ \bar{\chi}^2 &= \int \frac{d^3k}{(2\pi)^3} \frac{\zeta_{\mathbf{k}}\zeta_{-\mathbf{k}}}{(ck^2 - 2t)^2}. \end{aligned} \quad (15)$$

As in [1], one can take advantage of the fast convergence of the integrals to replace $\zeta_{\mathbf{k}}\zeta_{-\mathbf{k}}$ by $\phi_0 = \int \phi(\mathbf{r}) d\mathbf{r}$, after which the integrals on the right-hand sides can be

evaluated. For t independent of coordinates, Eq. (9) has the steady-state solution $\bar{\psi} = 0$ and

$$\bar{\psi}^2 = -\frac{t}{B} \left(1 - \frac{7}{8\pi c^{3/4}} \frac{\phi_0}{\sqrt{-2t}} \right)$$

at $t < 0$. For changes in t on a scale much larger than ξ_0 , one can neglect the contribution from the ‘‘roundings’’ occurring for $\int |\psi|^2 dV$ at the $t = 0$ surfaces, and the solution to Eq. (9) can almost always be approximated by the indicated steady-state solutions:

$$\begin{aligned} \bar{\psi} &= 0 \text{ at } t > 0, \\ \bar{\psi}^2 &= -\frac{t}{B} \left(1 - \frac{7}{8\pi c^{3/4}} \frac{\phi_0}{\sqrt{-2t}} \right) \text{ at } t < 0. \end{aligned} \quad (16)$$

To calculate the specific heat, one must know $\bar{\psi}^2 = \bar{\psi}^2 (1 + \chi^2)$. Combining Eqs. (15) and (16), one gets

$$\begin{aligned} \bar{\psi}^2 &= 0 \text{ at } t > 0, \\ \bar{\psi}^2 &= -\frac{t}{B} \left(1 - \frac{3}{4\pi c^{3/4}} \frac{\phi_0}{\sqrt{-2t}} \right) \text{ at } t < 0. \end{aligned} \quad (17)$$

The solution for $t < 0$ coincides with the one previously obtained by Larkin and Ovchinnikov, with the only difference that the temperature is now measured from the local transition temperature τ_0 . The final averaging over the ensemble or the sample volume is performed with the $g(-\tau_0)$ density:

$$\langle \bar{\psi}^2 \rangle = \int_{-\infty}^{+\infty} g(-\tau_0) \bar{\psi}^2(\tau - \tau_0) d\tau_0. \quad (18)$$

After evaluation of the $\partial \langle \bar{\psi}^2 \rangle / \partial \tau$ derivative and standard manipulations, one arrives at the following expression for the specific heat in the jump smearing zone vs. reduced temperature τ :

$$C_s = C_n + \frac{v}{B} \int_0^{\infty} \left(1 - \frac{3\phi_0}{2\pi(2c)^{3/2} \sqrt{u}} \right) g(-\tau - u) du. \quad (19)$$

The integration with weight $g(-\tau - u)$ eliminates the root singularity in the second term under the integral and makes the expression finite. Equation (19) is the solution of the stated problem. It expresses the specific heat as a function of temperature near T_c through the zero Fourier transform ϕ_0 of correlation function (4) and the $g(\tau)$ function connected with the density of states $\rho(\epsilon)$ for random potential $\zeta(\mathbf{r})$ by relationship (14).

3. When deriving Eq. (19), the random function $\zeta(\mathbf{r})$ was assumed to be a small perturbation. For this reason, the condition for applicability of this formula is

$\phi_0/c^{3/2} \sqrt{\theta} \ll 1$. With the rough estimate $\theta \sim \tau_0$, this condition reduces to $(\phi_0/\xi_0^3)^{1/2} \ll 1$. For randomly distributed impurities, one has

$$\phi_0 = \frac{1}{T_c^2} \left(\frac{dT_c}{dn} \right)^2 \bar{n},$$

where dT_c/dn is the derivative of the critical temperature with respect to the concentration of impurities that suppress superconductivity. As a result, the applicability criterion can be written as

$$\frac{\Delta T_c}{T_c} \frac{1}{\sqrt{n} \xi_0^3} \ll 1.$$

Here, ΔT_c is the impurity-induced decrease in the mean transition temperature. This criterion is always fulfilled for unconventional superconductors. The behavior of the specific heat in the vicinity of T_c is mainly governed by the $g(\tau)$ function. At $T < T_c$ and in the $|\tau| \gg \theta$ limit, Eq. (19) transforms into Eq. (13) from [1]. The asymptotic expression for $|\tau| \gg \theta$ at $T > T_c$ differs from the one

obtained in [2] by the absence of the $\bar{\psi}^4/(\bar{\psi}^2)^2$ multiplier. This distinction arises because the jump smearing in the close vicinity of T_c is governed by the large-scale fluctuations. The order parameter for such fluctuations is close to a constant value, while the indicated multiplier is close to unity. The main role in the tail of jump smearing belongs to fluctuations on the $\sim \xi$ scale, so that $\bar{\psi}^4/(\bar{\psi}^2)^2$ is different from unity. Note, however, that the case in point is only a preexponential factor of the order of unity.

The generalization of Eq. (19) to the multicomponent order parameter is straightforward, provided that either there is only a single superconducting phase or the transitions in different phases are well separated in temperature. For UPT₃, two closely-spaced transitions are observed, which merge as the concentration of defects increases. To describe both jumps self-consistently, it is necessary to include the terms of order $|\psi|^6$ in functional (1). The lack of such computations hampers the comparison of the formulas obtained in this work with the available UPT₃ data.

The major part of this work was done at the Institute of the French Commissariat on Atomic Energy in Grenoble. I am grateful to J. Flouquet for hospitality and stimulating discussions, to the J. Fourier University for financial support of my stay in Grenoble, to J.-P. Brison for collaboration, and to A.I. Larkin and Yu.N. Ovchinnikov for discussions and helpful criticism.

REFERENCES

1. A. I. Larkin and Yu. N. Ovchinnikov, Zh. Éksp. Teor. Fiz. **61**, 1221 (1971) [Sov. Phys. JETP **34**, 1279 (1971)].

2. B. L. Ioffe and A. I. Larkin, Zh. Éksp. Teor. Fiz. **81**, 707 (1981) [Sov. Phys. JETP **54**, 378 (1981)].
3. Yu. N. Ovchinnikov and V. Z. Kresin, Europhys. Lett. **46**, 794 (1999).
4. Yu. N. Ovchinnikov, S. A. Wolf, and V. Z. Kresin, Phys. Rev. B **60**, 4329 (1999).
5. J.-P. Brison, H. Suderow, P. Rodière, *et al.*, Physica B **281–282**, 872 (2000).
6. R. J. Keizer, A. de Visser, M. J. Graf, *et al.*, Phys. Rev. B **60**, 10527 (1999).
7. A. A. Abrikosov and L. P. Gor'kov, Zh. Éksp. Teor. Fiz. **39**, 1781 (1960) [Sov. Phys. JETP **12**, 1243 (1960)].
8. L. D. Landau and E. M. Lifshitz, *Course of Theoretical Physics*, Vol. 3: *Quantum Mechanics: Non-Relativistic Theory* (Nauka, Moscow, 1989, 4th ed.; Pergamon, Oxford, 1977, 3rd ed.).
9. B. I. Shklovskiĭ and A. L. Éfros, *Electronic Properties of Doped Semiconductors* (Nauka, Moscow, 1979; Springer-Verlag, New York, 1984).

Translated by V. Sakun

Giant Magnetoresistance of $\text{Me}_x\text{Mn}_{1-x}\text{S}$ (Me = Fe, Cr) Sulfides

G. A. Petrakovskii, L. I. Ryabinkina, G. M. Abramova*,
A. D. Balaev, D. A. Balaev, and A. F. Bovina

Kirenskiĭ Institute of Physics, Siberian Division, Russian Academy of Sciences,
Akademgorodok, Krasnoyarsk, 660036 Russia

* Krasnoyarsk State University, Krasnoyarsk, 660062 Russia

Received June 14, 2000

The structural, electrical, and magnetic properties, as well as the magnetoresistance of polycrystalline $\text{Me}_x\text{Mn}_{1-x}\text{S}$ (Me = Fe and Cr) sulfides were investigated in longitudinal magnetic fields of up to 50 kOe over the temperature range 4.2–300 K. The ferromagnetic compound $\text{Fe}_x\text{Mn}_{1-x}\text{S}$ ($x = 0.29$) exhibits the giant magnetoresistance (GMR) effect with magnitude $\delta_H = -450\%$ in a field of 30 kOe at 50 K. Antiferromagnetic $\text{Cr}_x\text{Mn}_{1-x}\text{S}$ ($x = 0.5$) sulfide undergoes a transition to the GMR state ($\delta_H \sim -25\%$ in a field of 30 kOe at 4.2 K) in the region of antiferromagnet–ferromagnet transition ($T_c \sim 66$ K). A mechanism of the GMR in these compounds is discussed. © 2000 MAIK “Nauka/Interperiodica”.

PACS numbers: 75.70.Pa; 71.30.+h; 72.80.-r

In spite of a great body of experimental data on the giant magnetoresistance (GMR) phenomenon in manganese lanthanide oxides with the perovskite structure, the mechanism of the GMR effect still remains to be clarified [1]. That is why a search for, and the study of, new compounds exhibiting the GMR effect and having a non-perovskite structure is a topical problem. Earlier [2], we revealed the GMR effect in $\text{Fe}_x\text{Mn}_{1-x}\text{S}$ sulfides derived from manganese monosulfide. The greatest effect ($\delta_H \sim -83\%$) in a transverse magnetic field of 10 kOe was observed for $x = 0.29$. This work reports the results of studying the structural, electrical, magnetic, and magnetoelectric properties of $\text{Fe}_x\text{Mn}_{1-x}\text{S}$ ($x = 0.29$) and $\text{Cr}_x\text{Mn}_{1-x}\text{S}$ ($x = 0.5$) sulfides at temperatures of 4.2–300 K in longitudinal magnetic fields of up to 50 kOe.

Polycrystalline samples of $\text{Me}_x\text{Mn}_{1-x}\text{S}$ (Me = Fe and Cr) were synthesized from pure elemental chromium, iron, manganese, and sulfur in evacuated quartz tubes by high-temperature annealing for a week [2]. X-ray structural analysis was performed on a DRON-2.0 diffractometer with monochromatic $\text{Cu } K_\alpha$ radiation in the temperature range 100–300 K. Electrical resistance was measured potentiometrically on a direct current over the temperature range of 4.2–300 K in longitudinal fields $H = 0, 2, 10, 30,$ and 50 kOe. The magnetic properties were measured on a vibrating-coil magnetometer with a superconducting solenoid in magnetic fields of up to 30 kOe in the range 77–300 K.

According to the X-ray data, the synthesized samples of $\text{Fe}_{0.29}\text{Mn}_{0.71}\text{S}$ and $\text{Cr}_{0.5}\text{Mn}_{0.5}\text{S}$ are solid solutions with the NaCl fcc lattice typical of manganese monosulfide [2, 3]. The X-ray patterns of the samples show

three extra lines with 5% relative intensity, indicating the presence of a possible impurity phase. The fcc lattice parameter of $\text{Fe}_x\text{Mn}_{1-x}\text{S}$ ($x = 0.29$) is $a = 5.186$ Å at room temperature. The compound undergoes a structural transition at $T_s \sim 147$ K, similar to that observed

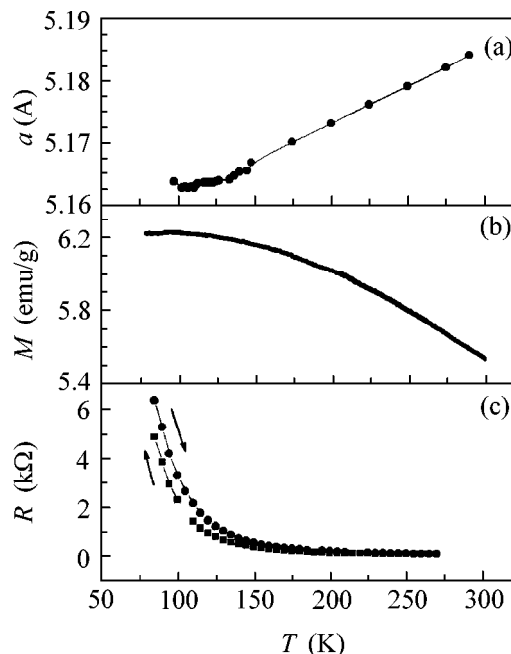


Fig. 1. Temperature-dependent (a) lattice parameter, (b) magnetization, and (c) resistivity of $\text{Fe}_{0.29}\text{Mn}_{0.71}\text{S}$.

for manganese monosulfide at 150 K [3]. As the temperature decreases, the lattice parameter first decreases, next is almost independent of temperature at 120–140 K, and then shows a tendency to increase below 120 K (Fig. 1a). An analogous structural transition also occurs in the $\text{Cr}_x\text{Mn}_{1-x}\text{S}$ ($x = 0.5$) sulfide near 160 K.

Magnetic measurements showed that the samples are ferromagnets at temperatures $T < 300$ K (Me = Fe) and $T < T_c = 66$ K (Me = Cr). The saturation magnetization ($H \sim 7\text{--}10$ kOe) for $\text{Fe}_x\text{Mn}_{1-x}\text{S}$ ($x = 0.29$) is 6.24 emu/g at 300 K. The temperature curves for the magnetization of the sulfides under study are shown in Figs. 1b and 3a. The value of $\rho_{77\text{ K}} \sim 10^2 \Omega \text{ cm}$ found for the resistivity of the samples at 77 K is five orders of magnitude lower than for $\alpha\text{-MnS}$. The conduction in the samples is of the semiconductor type with a thermal hysteresis in zero magnetic field at temperatures below 250 K (Fig. 1c).

Figure 2 demonstrates the temperature curves for the magnetoresistance δ_H of $\text{Fe}_x\text{Mn}_{1-x}\text{S}$ ($x = 0.29$) in longitudinal magnetic fields of 10, 30, and 50 kOe. It was pointed out in [2] that the negative magnetoresistance δ_H for this sulfide increases on lowering the temperature below 250 K in a field of 10 kOe and reaches its maximum value at ~ 160 K. Below 120 K, where the NaCl structure is distorted, the magnetoresistance changes sign. It was established that the change in sign of magnetoresistance disappears upon repeated measurements with the same sample at 120 K. This is likely caused by the hysteresis effects and the magnetic-induced changes in the state of the samples. After field removal, the magnetoresistance is lower than its initial (prior to the experiment) value at $T = 170$ K ($T > T_s$) and higher at 110 K ($T < T_s$). The resulting δ_H value calculated for fields of 0 and 10 kOe at 170 K is equal to -70% for the field buildup and to -50% for the field removal; at 110 K, the corresponding values are $+15\%$ and -127% .

As the magnetic field increases to 50 kOe, the negative magnetoresistance peak shifts to lower temperatures (Fig. 2). At 30 kOe, the negative magnetoresistance δ_H reaches a value of -450% for $\text{Fe}_x\text{Mn}_{1-x}\text{S}$ ($x = 0.29$) at ~ 50 K. At 50 kOe, this value is -87% .

Figure 3 shows the temperature curves for the magnetization (Fig. 3a) and magnetoresistance (Fig. 3b) of $\text{Cr}_x\text{Mn}_{1-x}\text{S}$ ($x = 0.5$). At 66 K, this sulfide undergoes the antiferromagnet–ferromagnet transition, whose nature is caused by the orbital degeneracy of the chromium ions and by the cooperative Jahn–Teller effect. One can see from Fig. 3 that the transition to the negative magnetoresistance state occurs in the range of magnetic transition. The δ_H value increases with lowering temperature and reaches a value of $\sim -25\%$ at 4.2 K in a field of 30 kOe.

An analysis of the experimental data obtained earlier in [2, 5] indicates that the concentration dependences of the electrical and magnetic properties of the

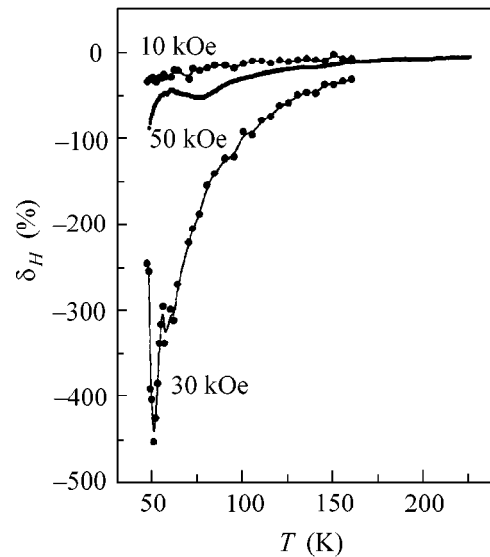


Fig. 2. Temperature-dependent magnetoresistances in a longitudinal magnetic field.

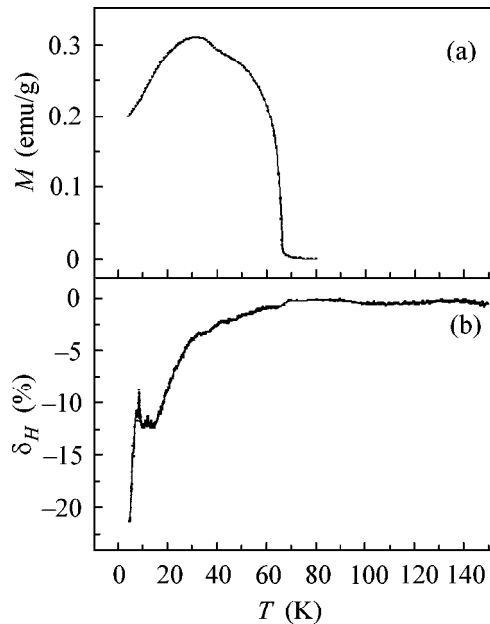


Fig. 3. Temperature-dependent (a) magnetization and (b) magnetoresistance of $\text{Cr}_{0.5}\text{Mn}_{0.5}\text{S}$ in a longitudinal magnetic field of 30 kOe.

solid solutions $\text{Me}_x\text{Mn}_{1-x}\text{S}$ are in many respects similar to those observed for manganese lanthanides. Namely, the ferromagnetic properties emerge simultaneously with the metallization of the samples; that is, the $\text{Me}_x\text{Mn}_{1-x}\text{S}$ samples with low concentration $x < 0.2$ are antiferromagnetic semiconductors, whereas the samples with $x \sim 0.4\text{--}0.6$ are ferromagnetic metals. The GMR effect is most pronounced in the intermediate compositions preceding the concentration transition to

the metallic state. It was assumed in [2] that among the possible GMR mechanisms in iron–manganese sulfides, there is a separation of magnetic and electronic phases, namely, the formation of a system in which the regions of antiferromagnetic semiconductor and ferromagnetic metal coexist. It is established in this work that the behavior of resistivity and magnetoresistance of the samples exhibits not only the temperature hysteresis but also the magnetic hysteresis. It is well known that the probability for the hysteretic effects to occur in the polycrystalline samples increases because of the presence of grain boundaries. However, the polycrystalline version of the hysteretic effects cannot explain the strong temperature shift of the magnetoresistance peak from 160 to 50 K in $\text{Fe}_x\text{Mn}_{1-x}\text{S}$. Since the GMR effect in $\text{Me}_x\text{Mn}_{1-x}\text{S}$ sulfides is observed in the region where the cubic lattice is distorted, a more thorough study of the crystal structure and the nature of the structural transition is necessary for the elucidation of the GMR mechanism. It is not improbable that the crystal structure of sulfides alters under the action of a magnetic field and thermocycling, as, e.g., it occurs in the $\text{RbDy}(\text{WO}_4)_2$ compound exhibiting the Jahn–Teller structural transition [6]. It should also be pointed out that the nature of the structural transition in manganese monosulfide remains to be explored.

We thank N.V. Volkov for providing an opportunity to perform experimental measurements. This work was supported by the Federal program “Integratsiya” (project no. 69) and the Russian Foundation for Basic Research–BRFFI (project no. 00-02-81059 Bel2000a).

REFERENCES

1. É. L. Nagaev, *Usp. Fiz. Nauk* **166**, 833 (1996) [*Phys. Usp.* **39**, 781 (1996)].
2. G. A. Petrakovskii, L. I. Ryabinkina, G. M. Abramova, *et al.*, *Pis'ma Zh. Éksp. Teor. Fiz.* **69**, 895 (1999) [*JETP Lett.* **69**, 949 (1999)].
3. H. H. Heikens, G. A. Wiegers, and C. F. van Bruggen, *Solid State Commun.* **24**, 205 (1977).
4. G. A. Petrakovskii, L. I. Ryabinkina, D. A. Velikanov, *et al.*, *Fiz. Tverd. Tela (St. Petersburg)* **41**, 1660 (1999) [*Phys. Solid State* **41**, 1520 (1999)].
5. G. A. Petrakovskii, G. V. Loseva, L. I. Ryabinkina, *et al.*, *J. Magn. Magn. Mater.* **140–144**, 146 (1995).
6. V. P. D'yakonov, V. I. Markovich, and V. L. Kovarskii, *Fiz. Tverd. Tela (St. Petersburg)* **40**, 2221 (1998) [*Phys. Solid State* **40**, 2017 (1998)].

Translated by V. Sakun

Anisotropy of Normal Resistivity in Oxygen-Deficient $\text{YBa}_2\text{Cu}_3\text{O}_{7-x}$ Single Crystals

V. N. Zverev* and D. V. Shovkun

Institute of Solid-State Physics, Russian Academy of Sciences, Chernogolovka, Moscow region, 142432 Russia
*e-mail: zverev@issp.ac.ru

Received June 15, 2000

Temperature dependences of the resistivity tensor components ρ_{ab} and ρ_c were measured for $\text{YBa}_2\text{Cu}_3\text{O}_{7-x}$ single crystals with different oxygen contents. The resistivity anisotropy ρ_c/ρ_{ab} was found to grow exponentially with decreasing temperature. The results are compared with the predictions of different models describing transverse transport in the normal state of cuprate high- T_c superconductors. © 2000 MAIK "Nauka/Interperiodica".

PACS numbers: 74.25.Fy; 74.72.Bk

Cuprate high- T_c superconductors are strongly anisotropic materials with a clearly defined laminated structure. The presence of cuprate CuO_2 planes, which are responsible, as is customarily believed, for superconductivity, is the common feature of these compounds. Although the normal conductivity of cuprate high- T_c superconductors has been intensively studied both experimentally and theoretically since the very discovery of high- T_c superconductivity (HTSC), there is still much debate over the mechanism of normal conductivity of these materials.

Within the CuO_2 layers, the conductivity of the cuprate HTSC compounds is metallic, with the resistivity ρ_{ab} linearly decreasing with a decrease in temperature over a wide temperature range. To explain such a dependence, new particles—holons and spinons—were introduced into the RVB model [1] and the theory of marginal Fermi liquid was suggested in [2]. This dependence can also be successfully explained by the usual electron–phonon scattering [3].

In the direction perpendicular to the CuO_2 layers, the resistivity of $\text{YBa}_2\text{Cu}_3\text{O}_{7-x}$ may increase with decreasing temperature even in the optimally doped ($x \approx 0$) samples [4]. As the oxygen concentration decreases, the $\rho_c(T)$ dependence becomes progressively steeper with a negative slope over the whole range from room temperature to T_c . Such behavior was originally explained by the crystal imperfections, namely, by the effect of semiconducting interlayers or by the disorder and localization effects in the transverse motion [5]. More recently, several theoretical models were suggested that explained such behavior for perfect crystals. In the theory of Anderson and Zou [1], the linear term in the temperature dependence is supplemented by a contribution proportional to $1/T$. The theory of Alexandrov and Mott predicts a considerably steeper exponential growth [6, 7]. In their theory, the transverse conduc-

tivity is mediated by polarons, whose concentration exponentially decreases with decreasing temperature because of polaron binding into bipolarons.

Recently, Abrikosov [8] proposed a new mechanism for carrier transport along the c axis in the HTSC materials, namely, resonance electron tunneling between the CuO_2 planes through the localized states in the CuO chains. It should be stressed that the Abrikosov theory assumes that the centers mediating the resonance tunneling are positioned exactly halfway in between the neighboring CuO_2 planes. This situation is automatically realized in $\text{YBa}_2\text{Cu}_3\text{O}_{7-x}$ single crystals with reduced oxygen content, where the role of such resonance levels may be played by the fragments of broken CuO chains. The applicability of the Abrikosov model to other cuprate HTSC compounds is unclear. It follows from the calculations in [8] that the temperature dependence of the resistivity anisotropy in the tunneling mechanism should have the form

$$\rho_c/\rho_{ab} = AT \cosh^2(T_0/T), \quad (1)$$

where A is a constant dependent on the parameters of the electron spectrum and the doping level, and T_0 is the characteristic activation energy specified by the energy levels mediating resonance tunneling. Equation (1) is expected to hold for the samples with oxygen concentration lower than optimal, where the CuO chains are broken, while the lower bound for the oxygen concentration is near the metal–insulator transition because of the competition with direct carrier tunneling between the CuO_2 planes. To our knowledge, no works devoted to the experimental verification of this model were published after appearance of the theory [8].

The purpose of this work is to experimentally study the temperature dependence of resistivity anisotropy for perfect $\text{YBa}_2\text{Cu}_3\text{O}_{7-x}$ single crystals with different carrier concentrations and to compare the results with

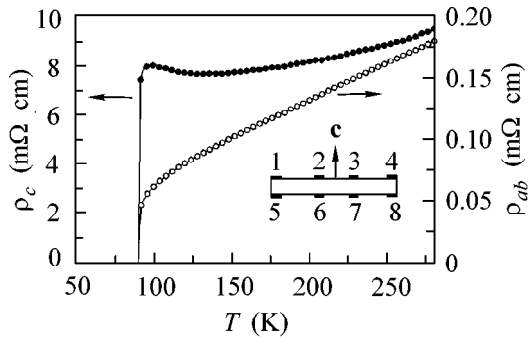


Fig. 1. Temperature dependence of the resistivity components ρ_{ab} and ρ_c for an initial single crystal of $\text{YBa}_2\text{Cu}_3\text{O}_{7-x}$. The geometry of contacts is shown in the inset.

the theory. In these studies, it is necessary to measure the resistivity tensor components ρ_{ab} and ρ_c for the same sample with different doping levels. To this end, we used the dc flux transformer method [9], allowing these components to be calculated from the measured potential differences arising at the opposite surfaces in the central part of the sample upon passing a current through the contacts at the edges of one of the surfaces. These measurements require at least six contacts (two current and four potential). We made measurements for samples with eight contacts, four at each of the surfaces (Fig. 1). This made it possible to pass current both through the upper pair of current contacts (1, 4) and through the lower pair (contacts 5, 8) and each time measure voltages $V_{2,3}$ and $V_{6,7}$ followed by averaging the measurement results. This minimized the error caused by the inaccurate positioning of the contacts.

The results of this work were obtained for a $\text{YBa}_2\text{Cu}_3\text{O}_{7-x}$ single crystal shaped like a rectangular plate $1.5 \times 0.2 \times 0.05$ mm in size, with the crystallographic c axis coinciding with the normal to the plate plane. The contacts were made from 30- μm -diameter gold wires glued by silver paste to the surfaces perpendicular to the c axis. The sizes of the contact areas were no greater than 0.15 mm, and the resistance of the fired contacts was on the order of 1 Ω . The initial $\text{YBa}_2\text{Cu}_3\text{O}_{7-x}$ single crystals were grown in a ZrO_2 crucible by the method described in [10]. After annealing at 500°C in oxygen, the samples showed a narrow (of width less than 0.5 K) superconducting transition and critical temperature $T_c \approx 91$ K (Fig. 1). The desired decrease in the oxygen concentration was achieved by choosing an appropriate temperature of annealing in air at atmospheric pressure followed by quenching in liquid argon, according to the data reported in [11–13].

When annealing, the samples were dusted with a powder of $\text{YBa}_2\text{Cu}_3\text{O}_{7-x}$ to preserve the high quality of the surfaces.

For measuring the temperature dependences of resistivity, the sample and nearby thermometer and heater were placed inside a glass Dewar vessel, which

was immersed upside down in liquid helium. To enhance temperature homogeneity, the sample was placed in a sapphire container.

The temperature dependences $\rho_{ab}(T)$ and $\rho_c(T)$ of the initial optimally doped single crystal are presented in Fig. 1. One can see that the $\rho_{ab}(T)$ dependence is linear over almost the whole temperature range except for a region near T_c , where the deviations from linearity are caused by fluctuative superconductivity. By contrast, the $\rho_c(T)$ curve is nonlinear and has a portion with a negative slope near T_c . The characteristic values of the resistivity tensor components and their temperature behavior correspond to the ones typically observed for high-quality single crystals [4].

It is seen from Fig. 2 that the $\rho_c(T)$ curve is linearized when the product $\rho_c T$ is plotted as a function of T^2 . This fact suggests that the temperature dependence $\rho_c(T)$ has the form

$$\rho_c = A_c/T + B_c T. \quad (2)$$

Expression (2) was used in a series of works as an argument in support of the RVB model, which predicts such a temperature behavior for both resistivity tensor components [1]. We would like to call attention to the fact that, for a doping level lower than optimal, the temperature dependences $\rho_{ab}(T)$ and $\rho_c(T)$ are no longer described by the curves corresponding to the samples with $T_c < 91$ K (Fig. 2).

Let now turn to the results obtained for the resistance anisotropy. The temperature dependence ρ_c/ρ_{ab} for a sample with reduced oxygen content ($T_c = 77$ K, $x \approx 6.77$) is shown in Fig. 3. The approximation of the experimental results by Eq. (1) is shown by the dashed line with optimal parameters $A = 0.178$ K $^{-1}$ and $T_0 = 223$ K. For comparison, the exponential approximation

$$\rho_c/\rho_{ab} = A_1 \exp(\Delta/T) \quad (3)$$

is also shown in Fig. 3 by the solid line. It is seen that Eq. (1), although satisfactorily describing the experimental data, makes it noticeably worse that does the activation exponent in Eq. (3). The log- $1/T$ plots of resistivity anisotropy are shown in Fig. 4 for several levels of doping with oxygen. In these coordinates, the experimental curves are seemingly linearized, whereas the dependence corresponding to Eq. (1) (dashed lines) is at variance with the experiment. Note that the optimization by Eqs. (1) and (3) was carried out in the same temperature range for each of the sample states. The temperature dependence is saturated at high values of resistivity anisotropy $\rho_c/\rho_{ab} > 10^3$; the saturation is most pronounced for the upper curve. This is likely caused by shunting of the conduction along the c axis, e.g., by virtue of direct carrier tunneling between the CuO_2 layers or through conduction along the dislocations or any other imperfections in the sample. The saturation of temperature dependence $\rho_c(T)$ narrows the interval where the temperature dependence can be

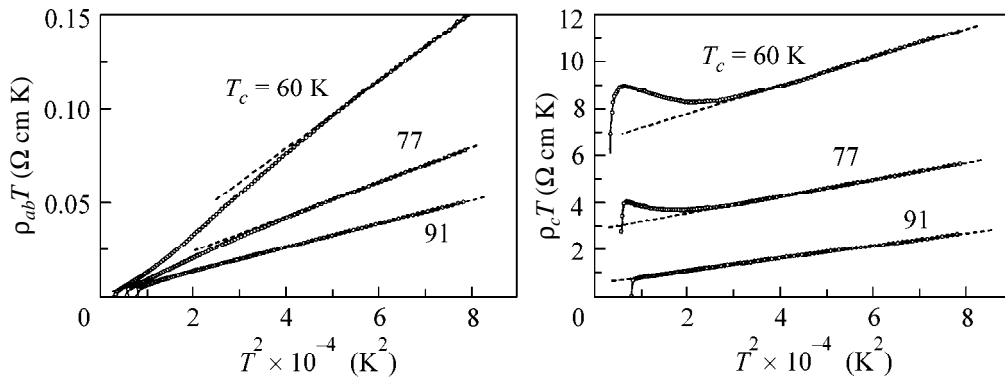


Fig. 2. Plots of $\rho_{ab}T$ and $\rho_c T$ as functions of T^2 for the samples with different oxygen content. Dashed lines are drawn through the rectilinear portions of the experimental curves.

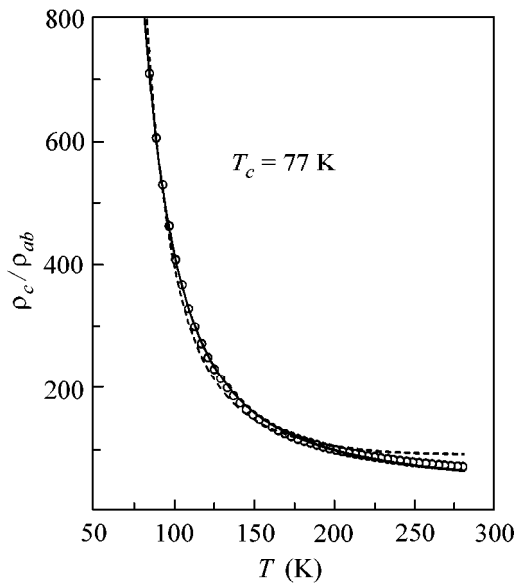


Fig. 3. Temperature dependence of the resistivity anisotropy for the sample with $T_c = 77$ K. The dashed and the solid curves are the interpolations by Eqs. (1) and (3), respectively.

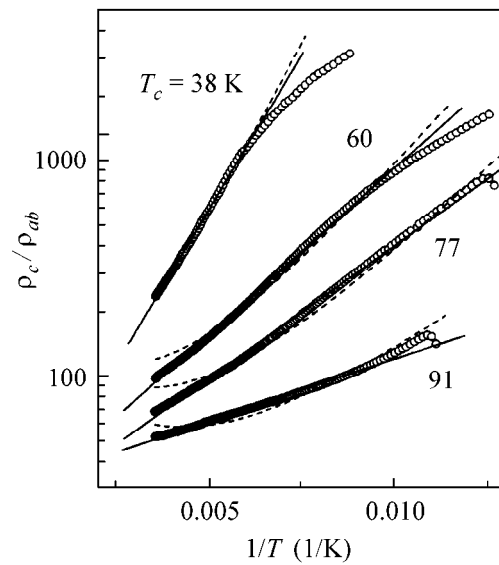


Fig. 4. Temperature dependences of the resistivity anisotropy for the samples with different doping level. Dashed lines are the interpolations by Eq. (1).

rationalized by one of the discussed theoretical models. In the upper curve, this interval is narrowed to $150 < T < 280$ K, within which the distinction between Eqs. (1) and (3) becomes insignificant.

The rectilinear portions in the curves shown in Fig. 4 correspond to the activation energies Δ increasing with a decrease in T_c ; they are equal to 146, 295, 356, and 665 K for the four curves shown in the figure. The pre-exponential factor A_1 virtually does not change and lies in the range 20–30. The exponential dependence of the anisotropy may be due to the fact that either the carriers are forced to overcome an energy barrier in moving across the CuO_2 planes or the concentration of carriers involved in transverse transport depends exponentially on temperature at $T > T_c$. The latter is possible, e.g., if the normal transport is preceded by the thermal decay

of somehow “prepared” electron pairs. Among the models providing the temperature exponent for the concentration of normal excitations, the bipolaron model of Alexandrov and Mott [6, 7], in which conduction along the c axis is accomplished by thermally excited polarons, is noteworthy. This should result in the temperature dependence of type (3) with an activation energy of half the bipolaron binding energy. The latter is independent of temperature but increases with decreasing carrier concentration. Note that exponential temperature behavior was previously observed for the resistivity anisotropy in $\text{Bi}_2\text{Sr}_2\text{CaCu}_2\text{O}_{8+\delta}$ single crystals with different oxygen content [14] and interpreted within the framework of this model.

To summarize, it is established that the temperature dependence of the resistivity anisotropy in oxygen-

deficient $\text{YBa}_2\text{Cu}_3\text{O}_{7-x}$ single crystals with $0 < x < 0.5$ is best described by an exponential function. The Abrikosov theory qualitatively fits the experiment but yields steeper temperature dependences. The RVB theory does not describe the experimental results for samples with oxygen concentrations below the optimal.

We are grateful to V.F. Gantmakher, V.V. Ryazanov, and M.R. Trunin for valuable remarks and to G.A. Emel'chenko and I.G. Naumenko for providing the $\text{YBa}_2\text{Cu}_3\text{O}_{7-x}$ single crystals. This work was supported by the Russian Foundation for Basic Research (project no. 98-02-16636) and the program "Superconductivity" (project no. 96-060).

REFERENCES

1. P. W. Anderson and Z. Zou, Phys. Rev. Lett. **60**, 132 (1988).
2. C. M. Varma, P. B. Littlewood, S. Schmitt-Rink, *et al.*, Phys. Rev. Lett. **63**, 1996 (1989).
3. G. M. Éliashberg, Pis'ma Zh. Éksp. Teor. Fiz. **48**, 275 (1988) [JETP Lett. **48**, 305 (1988)].
4. Y. Iye, in *Physical Properties of High T_c Superconductors*, Ed. by D. M. Ginsberg (World Scientific, Singapore, 1992).
5. A. G. Rojo and K. Levin, Phys. Rev. B **48**, 16861 (1993).
6. A. S. Alexandrov and N. F. Mott, Rep. Prog. Phys. **57**, 1197 (1994).
7. A. S. Alexandrov, V. V. Kabanov, and N. F. Mott, Phys. Rev. Lett. **77**, 4796 (1996).
8. A. A. Abrikosov, Usp. Fiz. Nauk **168**, 683 (1998) [Phys. Usp. **41**, 605 (1998)].
9. G. A. Levin, J. Appl. Phys. **81**, 714 (1997).
10. M. R. Trunin, A. A. Zhukov, G. A. Emel'chenko, and I. G. Naumenko, Pis'ma Zh. Éksp. Teor. Fiz. **65**, 893 (1997) [JETP Lett. **65**, 938 (1997)].
11. A. N. Lavrov and L. P. Kozeeva, Physica C (Amsterdam) **253**, 313 (1995).
12. A. N. Lavrov and L. P. Kozeeva, Physica C (Amsterdam) **248**, 365 (1995).
13. V. F. Gantmakher, L. P. Kozeeva, A. N. Lavrov, *et al.*, Pis'ma Zh. Éksp. Teor. Fiz. **65**, 834 (1997) [JETP Lett. **65**, 870 (1997)].
14. X. H. Chen, M. Yu, K. Q. Ruan, *et al.*, Phys. Rev. B **58**, 14219 (1998).

Translated by V. Sakun

Theory of Ferromagnetism for Metals of Cubic Symmetry

R. O. Zaitsev*

Kurchatov Institute Russian Research Center, pl. Kurchatova 1, Moscow, 123182 Russia

*e-mail: zaitsev@mbslab.kiae.ru

Received June 5, 2000

The conditions for the occurrence of ferromagnetism in 3d metals of cubic symmetry are obtained based on the concept of strong interaction in a single unit cell. The Hubbard model with infinitely strong repulsion is invoked for a quantitative description. The calculations are carried out in the zero-loop and one-loop approximations. The reasons for the occurrence of ferromagnetism in nickel and α -iron and its absence in Pd, Pt, and γ -iron are analyzed. © 2000 MAIK "Nauka/Interperiodica".

PACS numbers: 75.10.Jm; 75.50.Bb

Ferromagnetism of iron, cobalt, and nickel is caused by strong intraatomic interactions. According to calculations [1], this energy (Hubbard energy) for the Ni, Co, and Fe d electrons is 18.96, 17.77, and 16.54 eV, respectively, and far exceeds the transition energy $t^{i,k}(\mathbf{r})$ between the nearest neighboring atoms, for which reason the Hubbard energy is assumed to be infinite in what follows. The major part of the Hamiltonian has the form

$$\hat{H} = \sum_{\mathbf{r}, \mathbf{r}', \sigma} t^{i,k}(\mathbf{r} - \mathbf{r}') \hat{a}_{i,\sigma}^+(\mathbf{r}) \hat{a}_{k,\sigma}(\mathbf{r}') + \sum_{\mathbf{r}, \sigma, k} (\epsilon_k - \sigma H) \hat{a}_{i,\sigma}^+(\mathbf{r}) \hat{a}_{i,\sigma}(\mathbf{r}). \quad (1)$$

The (i, k) indices take five possible values corresponding to different crystallographic indices of d electrons. The matrix elements for the transition to the 4s states are not taken into account, because they are irrelevant to ferromagnetism. Band calculations indicate (see, e.g., [2]) that the energy of cubic anisotropy is slightly smaller than the energy of nearest neighbor hopping. For this reason, all one-particle energies, for simplicity, are set equal to the chemical potential taken with the opposite sign: $\epsilon_k = -\mu$. The matrix of tunnel transitions is assumed to be diagonal with respect to the crystallographic indices, and the corresponding density of one-particle states is replaced by the semielliptical density of states:

$$\sum_{\mathbf{r}} e^{-i\mathbf{p}\mathbf{r}} t^{i,k}(\mathbf{r}) = \delta_{i,k} t(\mathbf{p}), \quad (2)$$

$$\sum_{\mathbf{p}} \delta(\epsilon - t_{\mathbf{p}}) = \frac{2}{\pi} \sqrt{1 - \epsilon^2}.$$

The $\hat{a}_{i,\sigma}^+(\mathbf{r})$ and $\hat{a}_{k,\sigma}(\mathbf{r}')$ operators are the creation and annihilation operators for the hole d states, respectively. The product of these operators defines the hole density h_d , which is related to the s -electron density n_s (not exceeding unity) by the electroneutrality requirement.

Therefore, the problem is to examine hole-shell filling $0 < h_d < 1$ for the fcc nickel lattice and $2 < h_d < 3$ for the bcc and fcc iron lattices and to find the ferromagnetic instability regions. The $1 < h_d < 2$ range is not considered, because it corresponds to the fcc cobalt lattice, which does not exist at temperatures below 723 K.

After the diagonalization of the zeroth Hamiltonian corresponding to the nonoverlapping atomic states, the creation and annihilation operators are represented as expansions in terms of all possible transitions between the N and $N + 1$ hole states (cf. [3]):

$$\hat{a}_{(m,\sigma)}^+(\mathbf{r}) = \sum_{\alpha} g_{\alpha}^{m,\sigma} \hat{X}_{\mathbf{r}}^{\alpha}, \quad (3)$$

$$\hat{a}_{(n,\sigma)}(\mathbf{r}) = \sum_{\beta} g_{\beta}^{n,\sigma} \hat{X}_{\mathbf{r}}^{\beta}.$$

Here, the indices α and β correspond to the back and forth $s \rightarrow p$ transitions; i.e., $\beta(p, s) = -\alpha(s, p)$. The genealogical coefficients $g_{\alpha}^{m,\sigma}$ are evaluated below. The equations for the mean occupation numbers n_m are derived from the definition of the temperature Green's function calculated for each pair of conjugated X operators (cf. [4]):

$$D^{\alpha,\beta}(\mathbf{r}, \tau; \mathbf{r}, \tau') = -\Theta(\tau - \tau') \langle X_{\mathbf{r}}^{\alpha}(\tau) X_{\mathbf{r}}^{\beta}(\tau') \rangle + \Theta(\tau' - \tau) \langle X_{\mathbf{r}}^{\beta}(\tau') X_{\mathbf{r}}^{\alpha}(\tau) \rangle.$$

To calculate the one-particle Green's function, let us use the simplest one-loop self-consistent-field approxi-

mation. In this approximation, the Fourier transform $D_{\omega}^{\alpha, \beta}(\mathbf{p})$ of the one-particle Green's function differs from the so-called virtual Green's function $G_{\omega}^{\alpha, \beta}(\mathbf{p})$ only by the factor f_{β} . The virtual Green's function, in turn, satisfies the Dyson-type equation

$$\begin{aligned} D_{\omega}^{\alpha, \beta}(\mathbf{p}) &= G_{\omega}^{\alpha, \beta}(\mathbf{p})f_{\beta}; \\ \{\hat{G}_{\omega}^{-1}(\mathbf{p})\}_{\beta}^{\alpha} &= \{i\omega - \epsilon_m + \epsilon_s\}\delta(\alpha + \beta) - \Sigma_{\omega}^{\alpha, \beta}(\mathbf{p}), \end{aligned} \quad (4)$$

where $\epsilon_m - \epsilon_s$ is the energy corresponding to the α th transition, and $\omega = T(2n + 1)\pi$.

For a given one-particle transition $\beta(m, s)$, each end multiplier f_{β} , by definition, is equal to the sum of the mean occupation numbers for the initial and final states. At the same time, the self-energy part is equal, in the approximation adopted, to the sum of a product of the end multiplier times the generalized hopping matrix and a one-loop correction that depends neither on frequency nor on momentum:

$$\begin{aligned} f_{\alpha(s, m)} &= n_s + n_m, \\ \Sigma_{\omega}^{\alpha, \beta}(\mathbf{p}) &= f_{\alpha}t_{\beta}^{\alpha}(\mathbf{p}) + \Sigma_{\omega}^{\alpha, \beta}, \\ t_{\beta}^{\alpha}(\mathbf{p}) &= g_{\alpha}^{k, \sigma}t_s^k(\mathbf{p})g_{\beta}^{s, \sigma}. \end{aligned} \quad (5)$$

The mean occupation numbers n_{N+1}^m for the final states m are found from the diagonal component with $\beta = -\alpha$:

$$\begin{aligned} &\lim_{\delta \rightarrow 0^+} D_{\omega}^{\alpha, \beta}(\mathbf{r}, \tau; \mathbf{r}, \tau + \delta) \\ &= \lim_{\delta \rightarrow 0^+} T \sum_{\omega, \mathbf{p}} D_{\omega}^{\alpha, \beta}(\mathbf{p}) \exp(i\omega\delta) \\ &= \langle X_{\mathbf{r}}^{\beta(m, s)} X_{\mathbf{r}}^{\alpha(s, m)} \rangle = \langle X_{\mathbf{r}}^{m, s} X_{\mathbf{r}}^{s, m} \rangle = \langle X_{\mathbf{r}}^{m, m} \rangle = n_{N+1}^m. \end{aligned} \quad (6)$$

Equations (6) and (7) define all end multipliers $f(\alpha(s, m)) = n_s + n_m$ that appear in the expression for the diagonal components of the one-particle Green's function which, in turn, is expressed through all possible end multipliers and the one-loop self-energy parts $\Sigma_{\omega}^{\alpha, \beta}$.

The simplest equations for the determination of end multipliers can be obtained upon averaging the T -product of the annihilation operator times the linear combination of the conjugated X operators with arbitrary coefficients $\gamma_{\alpha}^{m, \sigma}$:

$$\begin{aligned} &-\langle \hat{T} \{ \hat{a}_{(n, \sigma)}(\mathbf{r}, \tau) \hat{Y}_{(m, \sigma)}(\mathbf{r}', \tau') \} \rangle \\ &= -\sum_{\alpha, \beta} g_{\alpha}^{n, \sigma} \gamma_{\beta}^{m, \sigma} \langle \hat{T} \{ \hat{X}_{\mathbf{r}, \tau}^{\alpha} \hat{X}_{\mathbf{r}, \tau'}^{\beta} \} \rangle. \end{aligned}$$

In this expression, use is made of the expansion of annihilation operator (3) with the known genealogical coefficients $g_{\beta}^{n, \sigma}$. By going to the limit $\tau' \rightarrow \tau$, $\tau' > \tau$, one

obtains the following equations for all $(N + 1)$ -particle occupation numbers n_{N+1}^s :

$$\begin{aligned} &\sum_{\alpha} g_{\alpha(m, s)}^{(k, \sigma)} n_{N+1}^s \gamma_{\alpha(s, m)}^{(k, \sigma)} \\ &= T \sum_{\alpha, \beta} g_{\alpha(m, s)}^{(k, \sigma)} \gamma_{\beta(s, m)}^{(k, \sigma)} \lim_{\delta \rightarrow 0^+} \sum_{\omega, \mathbf{p}} D_{\omega}^{\alpha, \beta}(\mathbf{p}) \exp(i\omega\delta). \end{aligned} \quad (7)$$

The equation of state is obtained by setting $\gamma_{\beta(s, m)}^{(k, \sigma)} = g_{\beta(s, m)}^{(k, \sigma)}$ in this relationship.

Restricting oneself to the transitions between the N - and $(N + 1)$ -hole states with degeneracy multiplicities R_- and R_+ , respectively, one arrives at the following equation of state for any integer-valued interval $[h_d] < h_d < [h_d] + 1$ of mean hole numbers:

$$\begin{aligned} h_d &= [h_d] + R_+ f K, \\ f &= \frac{h_d - [h_d]}{R_-} + \frac{[h_d + 1] - h_d}{R_+} = \frac{1}{R_- + K(R_+ - R_-)}. \end{aligned} \quad (8)$$

The square brackets stand for the integral part.

The temperature dependence of the mean occupation numbers is expressed through the number κ of orbital states and the Fermi distribution function $n_F(\epsilon)$ of the eigenvalues of the virtual Green's function (4):

$$\begin{aligned} K &= \frac{1}{\kappa} \sum_{\lambda=1}^{\kappa} \sum_{\mathbf{p}} n_F(g^2 f \epsilon_{\mathbf{p}}^{(\lambda)} - \mu), \\ D_n &= \frac{1}{\kappa} \sum_{\lambda=1}^{\kappa} \sum_{\mathbf{p}} (\epsilon_{\mathbf{p}}^{(\lambda)})^n n'_F(f g^2 \epsilon_{\mathbf{p}}^{(\lambda)} - \mu). \end{aligned} \quad (9)$$

Here, $\epsilon_{\mathbf{p}}^{(\lambda)}$ are the eigenvalues of transition matrix (1), which coincide with the energies in the tight-binding approximation, and g^2 is the sum of the squares of the genealogical coefficients entering expansion (2).

The coefficients D_n appear in the variation of the equation of state with respect to the external magnetic field δH :

$$\begin{aligned} \sum_{\alpha} (g_{\alpha(m, s)}^{(k, \sigma)})^2 \delta n_s &= (K + g^2 f D_1) \sum_{\alpha} g_{\alpha}^2 \delta f_{\alpha}^{\sigma} \\ &+ f D_0 \sum_{\alpha} g_{\alpha}^2 \delta \Sigma_{\alpha}^{\sigma} - f g^2 D_0 \sigma \delta H^{\sigma}. \end{aligned} \quad (10)$$

To derive the remaining equations for the variations δn_s of occupation numbers in the $(N + 1)$ -hole states, let us

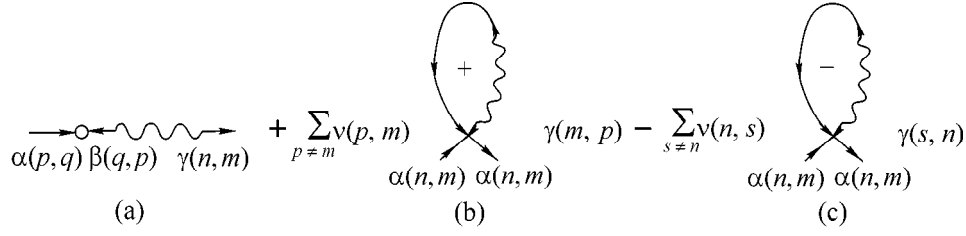


Fig. 1. (a) Zero-loop, (b) one-loop, and (c) self-energy parts.

invoke all possible sets of auxiliary coefficients orthogonal to a given set of genealogical coefficients:

$$\sum_{\alpha} g_{\alpha(m,s)}^{(k,\sigma)} \gamma_{\alpha(s,m)}^{(k,\sigma)} = 0. \quad (11)$$

Making use of these conditions, let us take a variation of Eq. (7) to deduce the relationships independent of the magnetic-field variation:

$$\begin{aligned} & \sum_{\alpha} g_{\alpha(m,s)}^{(k,\sigma)} \delta n_{N+1}^s \gamma_{\alpha(s,m)}^{(k,\sigma)} \\ &= K \sum_{\alpha} g_{\alpha(m,s)}^{(k,\sigma)} \gamma_{\alpha(s,m)}^{(k,\sigma)} \delta f_{\alpha}^{\sigma} + A \sum_{\alpha} g_{\alpha(m,s)}^{(k,\sigma)} \gamma_{\alpha(s,m)}^{(k,\sigma)} \delta \Sigma_{\alpha}^{\sigma}, \end{aligned} \quad (12)$$

where the new coefficient A for $H = 0$ is expressed through the tight-binding energies $\epsilon_{\mathbf{p}}^{(\lambda)}$:

$$A = \frac{1}{g^2 \kappa} \sum_{\lambda=1}^{\kappa} \sum_{\mathbf{p}} n_F(f g^2 \epsilon_{\mathbf{p}}^{(\lambda)} - \mu) - n_F(-\mu). \quad (13)$$

It is straightforward to obtain the equations for $\delta \Sigma_{\alpha}^{\sigma}$ from their definition in terms of the integrals of Green's functions (the so-called one-loop approximation):

$$\begin{aligned} \delta \Sigma_{\alpha}^{(\sigma)} &= -[Q W_{\alpha,\beta} - D_1 U_{\alpha,\beta}] \delta \Sigma_{\beta}^{(\sigma)} \\ &+ g^2 D_2 U_{\alpha,\beta} \delta f_{\beta}^{(\sigma)} - \sigma \delta H R_{\alpha} D_1. \end{aligned} \quad (14)$$

The components of the R_{α} vector and the $W_{\alpha,\beta}$ and $U_{\alpha,\beta}$ matrices are expressed through the numerical values of the S matrix constructed in accordance with the definition of the self-energy matrix [see Eq. (5) and the figure]:

$$\begin{aligned} R_{\alpha} &= \sum_{\beta} S_{\alpha,\beta}, \quad U_{\alpha,\beta} = R_{\alpha} \frac{g_{\beta}^2}{g}, \\ W_{\alpha,\beta} &= U_{\alpha,\beta} - S_{\alpha,\beta} = \sum_{\gamma} S_{\alpha,\gamma} \frac{g_{\beta}^2}{g} - S_{\alpha,\beta}, \\ g^2 &= \sum_{\gamma} g_{\gamma}^2. \end{aligned} \quad (15)$$

The coefficient Q can be related to the K quantity appearing in the equation of state (9) with $H = 0$:

$$\begin{aligned} Q &= \frac{1}{f g^2 \kappa} \sum_{\lambda=1}^{\kappa} \sum_{\mathbf{p}} [n_F(f g^2 \epsilon_{\mathbf{p}}^{(\lambda)} - \mu) - n_F(-\mu)] \\ &= \frac{1}{f g^2} [K - n_F(-\mu)]. \end{aligned} \quad (16)$$

With nickel, for which the empty and one-hole states are in resonance, all genealogical coefficients are unity, while the variations of the end multipliers coincide with the variations of the single-hole occupation numbers:

$$\delta n_I^{\sigma} = \delta f^{\sigma}, \quad \hat{S} = \hat{U} = 1, \quad \hat{W} = 0. \quad (17)$$

On substituting these relationships into basic Eqs. (10), (12), and (14), one can determine variations for the end multipliers and the occupation numbers.

The condition for ferromagnetism can be found from the requirement that the appropriate system of homogeneous equations be resolvable at zero magnetic-field variation:

$$1 - K = f D_1 + D_1(1 - K) - f(D_0 D_2 - D_1^2). \quad (18)$$

In the $T = 0$ limit, all coefficients are expressed in terms of the integrals of density of states:

$$K = \int_{-\infty}^{\nu} \rho(\epsilon) d\epsilon, \quad f D_k = -\nu^k \rho(\nu), \quad \nu = \mu/f. \quad (19)$$

In the model of semielliptical density of states $\rho(\epsilon) = 2\sqrt{1 - \epsilon^2}/\pi$, the following condition holds:

$$\begin{aligned} K &= \frac{\alpha - \sin \alpha}{2\pi}, \quad f D_1 = \frac{\sin \alpha}{\pi}, \\ \frac{1 - K}{-(2\kappa - 1)K^2 + (2\kappa - 2)K + 2} &= \frac{\sin \alpha}{\pi}. \end{aligned} \quad (20)$$

For a given degeneracy multiplicity 2κ , the last equation determines the critical K_c value corresponding to the critical concentration

$$h_{dc} = 2\kappa K_c / [1 + (2\kappa - 1)K_c].$$

For $\kappa = 5$, two critical points are obtained: $K_{c1} = 0.1161$, i.e., $h_{c1} = 0.5671$, and $K_{c2} = 0.295$, i.e., $h_{c2} = 0.8071$. (These results are in qualitative agreement with the results obtained in [5]).

With iron, where the two-hole states are in resonance with the three-hole states, one has three independent genealogical coefficients $\mathbf{g} = (1, \sqrt{2/3}, 1/\sqrt{3})$, so that $\gamma_1 = (1, 0, -\sqrt{3})$ and $\gamma_2 = (\sqrt{3}, -2\sqrt{2}, 1)$ can be chosen as two independent, mutually orthogonal vectors.

The variations for three-hole states with four different spin projections $S_z = \pm 3/2$ and $S_z = \pm 1/2$ can be expressed through the variations of three end multipliers:

$$\delta n_{(III)}^{(3\sigma/2)} = \sum_{\alpha=1}^3 \delta f_{(k,\alpha)}^{(\sigma)}, \quad \delta n_{(III)}^{(\sigma/2)} = \delta f_{(k,2)}^{(\sigma)}. \quad (21)$$

One can see that the end multipliers are independent of the number \mathbf{k} of the orbital state.

It is straightforward to evaluate the one-loop self-energy parts in Figs. 1b and 1c and express them through three independent integrals, each proportional to the square of one of the genealogical coefficients. As a result, matrices (15) appearing in Eq. (14) are found to be

$$\hat{S} = \begin{pmatrix} 0; & 0; & 1 \\ 0; & 2; & -1 \\ 3; & -2; & 0 \end{pmatrix}; \quad \mathbf{R} = (1, 1, 1); \quad (22)$$

$$\hat{W} = \begin{pmatrix} 1/2; & 1/3; & -5/6 \\ 1/2; & -5/3; & 7/6 \\ -5/2; & 7/3; & 1/6 \end{pmatrix}.$$

Substituting these relations and matrices into basic Eqs. (10) and (14), one can determine variations for the end multipliers and the occupation numbers.

This system of equations can be resolved at zero magnetic-field variation only if the corresponding determinant is zero:

$$1 = -2Q, \quad 1 = 3Q, \quad K = 1,$$

$$K(1-K) = g^2 f D_1 \left(\frac{2}{3} + K \right) + K(1-K) D_1$$

$$+ f g^2 \left(\frac{2}{3} + K \right) (D_2 D_0 - D_1^2). \quad (23)$$

In our case, $g^2 = 12$, $R_- = 30$, and $R_+ = 40$. The inverse of the end multiplier is a linear function of K :

$$\frac{1}{f} = 30 + 10K, \quad K = \frac{\alpha - \sin \alpha}{2\pi}, \quad (24)$$

$$f g^2 D_1 = \frac{\sin \alpha}{\pi}, \quad h_d = 6 \frac{1+K}{3+K}.$$

Substitution of these relations into Eq. (23) allows its right-hand side to be expressed as a function of K and α , which are related to each other by equation of state (24). The solution of these equations gives the α and K parameters corresponding to the critical number of holes, above which the ferromagnetic instability does not arise. Note that the singularities associated with the poles at $Q = 1/3$, $Q = 1/2$, and $K = 1$ are irrelevant to the ferromagnetic instability, because the corresponding eigenvectors are orthogonal to the vector perturbations of a uniform magnetic field.

The numerical solution of Eq. (23), together with the equation of state at $T = 0$, gives only a single root: for the semielliptical density of states (3) $\alpha_c = 2.6938$ and $K_c = 0.3583$, so that the ferromagnetic instability occurs in a limited concentration range $2 < h_d < h_{c1} = 2.428$. This interval is slightly larger than the one given by the zero-loop approximation: $2 < h_d < h_{c0} = 2.3388$.

This result is pertinent to the ferromagnetism of the bcc α -iron lattice, for which the saturation magnetic moment is 2.2 μB . As to the nonferromagnetic phase of γ -iron, measurements suggest that the number of d electrons in fcc iron is approximately 7.5, so that the number of holes is 2.5.

Thus, α -iron is a ferromagnet, because the number of hole states (≈ 2.2) falls within the ferromagnetic instability interval. The absence of ferromagnetism in γ -iron is explained by the fact that the number of holes in the $3d$ shell, ≈ 2.5 , exceeds the critical value calculated in both zero-loop and one-loop approximations.

General Eqs. (10)–(14) can also be applied to cobalt, for which the number of holes ranges from unity to two. As a result, the ferromagnetism region is found to be $1 < h_c < 1.585$. However, the resulting critical h_c value is obtained for $T = 0$. It cannot be experimentally verified for Co, because its fcc crystal phase exists at temperatures $T > T^* = 723$ K, while the ferromagnetism disappears at $T = T_c = 1440$ K.

The theory suggested in this work qualitatively explains the magnetic properties of the Ni, Pd, and Pt metals. All of them have a cubic unit cell of the fcc type. The total number of conduction electrons is 10, and the number of electrons in the unfilled s shell does not exceed unity. Band calculations suggest [2] that the number of s electrons in the unfilled s shell is 0.81, 0.59, and 0.94 for Ni, Pd, and Pt, respectively. One can thus infer that the number h_d of d -hole states is also equal to 0.81, 0.59, and 0.94. The number of hole states for nickel is intermediate between h_d in palladium and

platinum, so that the hole concentrations in Pd and Pt are beyond the ferromagnetic instability range, whereas the intermediate hole concentration in Ni falls within this range. The critical values $h_{c1} = 0.567$ and $h_{c2} = 0.807$ obtained by the theory suggested in this work are slightly smaller than those given by the band calculations. Nevertheless, the value of $\mu_B = 0.6$, commonly accepted for the saturation magnetic moment of Ni, is not contradictory to the calculations of this work and falls within the calculated magnetic ordering range.

This work was supported by the Russian Foundation for Basic Research, project no. 98-02-17388.

REFERENCES

1. C. F. Fischer, *At. Data* **4**, 301 (1972).
2. W. A. Harrison, *Electronic Structure and the Properties of Solids: The Physics of the Chemical Bond* (Freeman, San Francisco, 1980; Mir, Moscow, 1983).
3. J. Hubbard, *Proc. R. Soc. London, Ser. A* **277**, 237 (1963).
4. R. O. Zaitsev, *Zh. Éksp. Teor. Fiz.* **112**, 2223 (1997) [*JETP* **85**, 1218 (1997)].
5. W. Nolting, W. Borgiel, V. Dose, and Th. Fauster, *Phys. Rev. B* **40**, 5015 (1989).

Translated by V. Sakun

Exact Singlet Bond Ground States for Electronic Models¹

D. V. Dmitriev, V. Ya. Krivnov*, and A. A. Ovchinnikov

Joint Institute of Chemical Physics, ul. Kosygina 4, Russian Academy of Sciences, Moscow, 117977 Russia

Max-Planck-Institut für Physik Komplexer Systeme, 01187 Dresden, Germany

*e-mail: krivnov@deom.chph.ras.ru

Received June 14, 2000

We proposed several 1D and 2D electronic models with the exact ground state. The ground-state wave function of these models is represented in terms of “singlet bond” functions consisting of homopolar and ionic configurations. The Hamiltonians of these models include correlated hopping of electrons, pair hopping terms, and spin interactions. © 2000 MAIK “Nauka/Interperiodica”.

PACS numbers: 71.10.–w; 75.10.Jm

The study of strongly correlated electron systems has been an important subject in theoretical condensed matter physics. In general, the Hamiltonians of these systems include many types of interactions, and they are difficult to solve. The integrable models provided us with a very good understanding of correlation effects in many-body systems. Unfortunately, the construction of such models is difficult due to the strict conditions for the integrability. In recent years, there has been increasing interest in studying models where at least the ground state can be found exactly [1–4]. The most popular methods for the construction of an exact ground state are the so-called optimal ground state (OGS) approach [2] and the matrix-product (MP) method [3, 4]. The ground-state wave function in the MP method is represented by Trace of a product of matrices describing one-site states. This ground state is “optimum” in the sense that it is the ground state of each local interaction. This method allows the construction of a large class of spin models. A similar approach has been used in the OGS method for the construction of the electronic models with the special ground states.

In this paper, we propose new 1D and 2D models of interacting electrons with an exact ground state. We note that our models have ground states that are very different from those constructed in the OGS approach. The ground-state wave function of our models is expressed in terms of the two-particle “singlet bond” (SB) function located on sites i and j of the lattice:

$$[i, j] = c_{i,\uparrow}^+ c_{j,\downarrow}^+ - c_{i,\downarrow}^+ c_{j,\uparrow}^+ + x(c_{i,\uparrow}^+ c_{i,\downarrow}^+ + c_{j,\uparrow}^+ c_{j,\downarrow}^+) |0\rangle, \quad (1)$$

where $c_{i,\sigma}^+$, $c_{i,\sigma}$ are the Fermi operators and x is an arbitrary coefficient. The SB function is the generalization of the Resonating Valence Bond (RVB) function [5] including ionic states. The presence of the ionic states is very important from the physical point of view

because, as a rule, the bond functions contain definite amounts of the ionic states as well.

A series of 1D and 2D quantum spin models, for which the exact ground state can be represented in the RVB form, are considered in [6–10]. It is natural to try to find electronic models with an exact ground state at half-filling formed by SB functions in the same manner as for the above-mentioned spin models. The electronic models of these types include the correlated hopping of electrons, as well as the spin interactions and pair hopping terms.

The model with dimerization. As the first example, we consider the 1D electronic model with a two-fold degenerate ground state in the form of a simple product of SB dimers, similar to the ground state of the well-known spin-1/2 Majumdar–Ghosh model [6]. For the half-filling case, the proposed ground-state wave functions are

$$\Psi_1 = [1, 2][3, 4] \dots [N-1, N] \quad (2)$$

and

$$\Psi_2 = [2, 3][4, 5] \dots [N, 1]. \quad (3)$$

In order to find the Hamiltonian for which the wave functions (2) and (3) are the exact ground-state wave functions, we represent the Hamiltonian as a sum of local Hamiltonians h_i defined on three neighboring sites (periodic boundary conditions are supposed):

$$H = \sum_{i=1}^N h_i. \quad (4)$$

The basis of three-site local Hamiltonians h_i consists of 64 states, while only 8 of them are present in Ψ_1 and Ψ_2 . These 8 states are

$$[i, i+1] \varphi_{i+2}, \quad \varphi_i [i+1, i+2], \quad (5)$$

where φ_i is one of the four possible electronic states in the i th site: $|0\rangle_i$, $|\uparrow\rangle_i$, $|\downarrow\rangle_i$, $|2\rangle_i$.

¹ This article was submitted by the authors in English.

The local Hamiltonian h_i , for which all functions (5) are the exact ground-state wave functions, can be written as the sum of the projectors onto the other 56 states $|\chi_k\rangle$:

$$h_i = \sum_k \lambda_k |\chi_k\rangle \langle \chi_k|, \quad (6)$$

where λ_k are arbitrary positive coefficients. This means that the wave functions Ψ_1 and Ψ_2 are the ground states of each local Hamiltonian with zero energy. Hence, Ψ_1 and Ψ_2 are the optimum ground-state wave functions of the total Hamiltonian H with zero energy, similar to the models in [2–4]. In the general case, the local Hamiltonian h_i is multiparameter and depends on the parameters λ_k and x . We consider one of the simplest forms of h_i including the correlated hopping of electrons of different types and spin interactions between nearest- and next-to-nearest neighbor sites:

$$\begin{aligned} h_i = & 2 - x(t_{i,i+1} + t_{i+1,i+2}) \\ & + (x^2 - (1+x^2)(1-n_{i+1})^2)T_{i,i+2} \\ & + 8\frac{1-x^2}{3}(\mathbf{S}_i \cdot \mathbf{S}_{i+1} + \mathbf{S}_{i+1} \cdot \mathbf{S}_{i+2} + \mathbf{S}_i \cdot \mathbf{S}_{i+2}), \end{aligned} \quad (7)$$

where

$$\begin{aligned} T_{i,j} = & \sum_{\sigma} (c_{i,\sigma}^+ c_{j,\sigma} + c_{j,\sigma}^+ c_{i,\sigma})(1 - n_{i,-\sigma} - n_{j,-\sigma}), \\ t_{i,j} = & \sum_{\sigma} (c_{i,\sigma}^+ c_{j,\sigma} + c_{j,\sigma}^+ c_{i,\sigma})(n_{i,-\sigma} - n_{j,-\sigma})^2, \end{aligned}$$

and \mathbf{S}_i is the $SU(2)$ spin operator.

Each local Hamiltonian h_i is a nonnegatively defined operator at $|x| \leq 1$. The following statements related to the Hamiltonian (7) are valid.

1. The functions (2) and (3) are the only two ground-state wave functions of the Hamiltonian (7) at $N_e = N$ (N_e is the total number of electrons). They are not orthogonal, but their overlap is $\sim e^{-N}$ at $N \gg 1$.

2. The ground state energy $E_0(N_e/N)$ is a symmetric function with respect to the point $N_e/N = 1$ and has a global minimum $E_0 = 0$ at $N_e/N = 1$.

3. The translational symmetry of (7) is spontaneously broken in the ground state, leading to the dimerization

$$\langle |t_{i,i+1} - t_{i+1,i+2}| \rangle = 2.$$

The excited states of the model cannot be calculated exactly, but we expect that there has to be a gap, because the ground state is formed by the ultrashort-range SB functions. If it is the case, the function $E_0(N_e/N)$ has a cusp at $N_e/N = 1$.

Actually, this model is the fermion version of the Majumdar–Ghosh spin model. Moreover, it reduces to

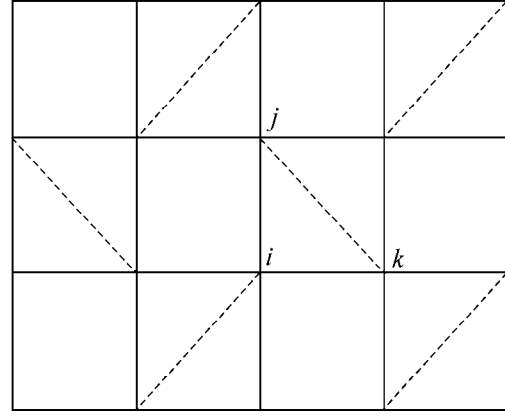


Fig. 1. The lattice in the Shastry–Sutherland model.

the Majumdar–Ghosh model at $x = 0$ and in the subspace with $n_i = 1$.

For $x = 1$, Hamiltonian (7) is simplified and takes the form:

$$H = -2 \sum_j (t_{j,j+1} - 1) - \sum_j e^{i\pi n_{j+1}} T_{j,j+2}. \quad (8)$$

The 2D model. We can easily construct the 2D electronic model with the exact ground state which is analogous to the Shastry–Sutherland model [7] (Fig. 1). The Hamiltonian of this model is

$$H = \sum_{\{i,j,k\}} h_{i,j} + h_{i,k} + h_{j,k}^d, \quad (9)$$

where the sum is over all triangles $\{i,j,k\}$, one of which is shown in Fig. 1. Thus, each diagonal line belongs to two different triangles. The local Hamiltonians $h_{j,k}^d$ acting on the diagonal of the triangle $\{i,j,k\}$ and $h_{i,j}, h_{i,k}$ have the form (for the sake of simplicity, we put $x = 1$)

$$\begin{aligned} h_{j,k}^d = & -2t_{j,k} + 4, \\ h_{i,j} = & -t_{i,j} - e^{i\pi n_k} T_{i,j}, \\ h_{i,k} = & -t_{i,k} - e^{i\pi n_j} T_{i,k}. \end{aligned}$$

It is easy to check that

$$h_{j,k}^d |\varphi_i[j,k]\rangle = (h_{i,j} + h_{i,k}) |\varphi_i[j,k]\rangle = 0.$$

All other states of the local Hamiltonian $h_{i,j} + h_{i,k} + h_{j,k}^d$ have higher energies. Therefore, the ground-state wave function in the half-filling case is the product of the SB functions located on the diagonals shown by dashed lines in Fig. 1. This model has a nondegenerate singlet ground state with ultrashort-range correlations.

The ladder model. Let us now consider electronic models with a more complicated ground state including different configurations of short-range SB functions. The form of these ground states is similar to that for spin models proposed in [8] and generalized in [9].

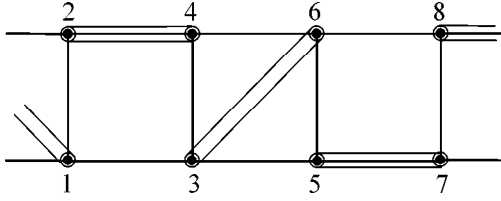


Fig. 2. The two-leg ladder model.

In the 1D case, our model describes the two-leg ladder model (Fig. 2). Its ground state is a superposition of the SB functions, where each pair of nearest neighbor rungs of the ladder is connected by one SB. One possible configuration of singlet bonds is shown in Fig. 2.

The wave function of this ground state can be written as

$$\Psi_s = \psi^{\lambda\mu}(1)g_{\mu\nu}\psi^{\nu\rho}(2)g_{\rho\kappa}\dots\psi^{\sigma\tau}(N)g_{\tau\lambda}. \quad (10)$$

A wave function of this type for spin models has been proposed in [8]. The functions $\psi^{\lambda\mu}(i)$ describe the i th rung of the ladder:

$$\psi^{\lambda\mu}(i) = c_1\phi_{2i-1}^\lambda\phi_{2i}^\mu + c_2\phi_{2i}^\lambda\phi_{2i-1}^\mu, \quad (11)$$

with

$$\phi_k^\lambda = \begin{pmatrix} |\uparrow\rangle_k \\ |\downarrow\rangle_k \\ |2\rangle_k \\ |0\rangle_k \end{pmatrix}, \quad g_{\lambda\mu} = \begin{pmatrix} 0 & 1 & 0 & 0 \\ -1 & 0 & 0 & 0 \\ 0 & 0 & 0 & x \\ 0 & 0 & x & 0 \end{pmatrix}.$$

It is easy to see that

$$g_{\lambda\mu}\phi_i^\lambda\phi_j^\mu = [i, j].$$

Therefore, the function Ψ_s is a singlet wave function depending on two parameters x and c_1/c_2 . Actually, this form of Ψ_s is equivalent to the MP form with 4×4 matrices $A_{\lambda\nu}(i) = g_{\lambda\mu}\psi^{\mu\nu}(i)$. Moreover, at $x = 0$ and $c_1/c_2 = -1$ the function Ψ_s reduces to the wave function of the well-known AKLT (Affleck–Kennedy–Lieb–Tasaki) spin-1 model [8].

In order to find the Hamiltonian for which the wave function (10) is the exact ground-state wave function, it is necessary to consider which states are present on the two nearest rungs in Ψ_s . It turns out that there are only 16 states from a total of 256 in the product $\psi^{\lambda\mu}(i)g_{\mu\nu}\psi^{\nu\rho}(i+1)$. The local Hamiltonian h_i acting on the two nearest rungs i and $i+1$ can be written in the form of Eq. (6) with the projectors onto the 240 missing states. The total Hamiltonian is the sum of the local ones (4). The explicit form of this Hamiltonian is very cumbersome and therefore is not given here.

The correlation functions for the ground state (10) can be calculated in exactly the same manner as was done for spin models [8]. It can be shown that all corre-

lations exponentially decay in the ground state. We also expect that this model has a gap.

This method of constructing the exact ground state can also be generalized to 2D and 3D lattices [9]. Following [9], one can rigorously prove that the ground state of these models is always a nondegenerate singlet.

1D models with the giant spiral order. There is one more spin-1/2 model with an exact ground state of the RVB type [10]. Its Hamiltonian has the form

$$H = -\sum_i \mathbf{S}_i \cdot \mathbf{S}_{i+1} + \frac{1}{4} \sum_i \mathbf{S}_i \cdot \mathbf{S}_{i+2}. \quad (12)$$

This model describes the ferromagnet–antiferromagnet transition point. The exact singlet ground state can be expressed by the combinations of the RVB functions (i, j) distributed uniformly over the lattice points:

$$\Phi_0 = \sum (i, j)(k, l)(m, n)\dots, \quad (13)$$

where the summation goes over all combinations of sites, under the condition that $i < j, k < l, m < n \dots$. The spin correlations in the singlet ground state show a giant spiral structure [10].

The analogue of the wave function (13) in the SB terms is:

$$\Psi_0 = \sum_{i < j \dots} (-1)^P [i, j][k, l][m, n]\dots, \quad (14)$$

where $P = (i, j, k, l, \dots)$ is the permutation of numbers $(1, 2, \dots, N)$. It is interesting to note that the singlet wave function (14) can also be written in the MP form but with an infinite-size matrices [11]. The Hamiltonian, for which the wave function (14) is the exact ground-state wave function, has the form

$$H = \sum_{i=1}^N \left(T_{i,i+1} - \frac{2}{x} t_{i,i+1} - 4\mathbf{S}_i \cdot \mathbf{S}_{i+1} + \frac{4}{x^2} \eta_i \cdot \eta_{i+1} + 4 \frac{x^2 - 3}{x^2} \eta_i^z \eta_{i+1}^z \right), \quad (15)$$

where

$$\eta_i^+ = c_{i,\downarrow}^+ c_{i,\uparrow}^+, \quad \eta_i^- = c_{i,\uparrow} c_{i,\downarrow}, \quad \eta_i^z = (1 - n_i)/2.$$

This model describes the transition point where the singlet ground state (14) is degenerate with the ferromagnetic state. The spin–spin correlations in the singlet ground state (14) have a giant spiral form, as in the spin model (12), while other correlations vanish in the thermodynamic limit [11].

In summary, we have constructed electronic models with an exact ground state. The ground-state wave function of these models is built from SB functions in the same manner as are the well-known RVB ground states of spin models. We have considered three types of SB ground states. All electronic models considered

have physical properties similar to those of the original spin models. We note that the proposed approach can be generalized for the construction of other models with the ground states of more complicated SB forms.

We are grateful to the Max-Planck-Institut für Physik Komplexer Systeme for kind hospitality. This work was supported by the Russian Foundation for Basic Research (project nos. 00-03-32981 and 00-15-97334).

REFERENCES

1. R. Strack and D. Vollhardt, Phys. Rev. Lett. **70**, 2637 (1993); Phys. Rev. Lett. **72**, 3425 (1994).
2. Jan de Boer and A. Schadschneider, Phys. Rev. Lett. **75**, 4298 (1995).
3. A. Klumper, A. Schadschneider, and J. Zittartz, Z. Phys. B **87**, 281 (1992); Europhys. Lett. **24** (4), 293 (1993).
4. A. K. Kolezhuk and H.-J. Mikeska, Phys. Rev. B **56**, R11380 (1997); Int. J. Mod. Phys. B **12**, 2325 (1998).
5. P. W. Anderson, Mater. Res. Bull. **8**, 153 (1973); Science (Washington, D.C.) **235**, 1196 (1987).
6. C. K. Majumdar and D. K. Ghosh, J. Math. Phys. **10**, 1388 (1969); **10**, 1399 (1969).
7. B. S. Shastry and B. Sutherland, Physica B (Amsterdam) **108**, 1069 (1981).
8. I. Affeck, T. Kennedy, E. H. Lieb, and H. Tasaki, Phys. Rev. Lett. **59**, 799 (1987); Commun. Math. Phys. **115**, 477 (1988).
9. D. V. Dmitriev, V. Ya. Krivnov, and A. A. Ovchinnikov, Zh. Éksp. Teor. Fiz. **115**, 249 (1999) [JETP **88**, 138 (1999)].
10. T. Hamada, J. Kane, S. Nakagawa, and Y. Natsume, J. Phys. Soc. Jpn. **57**, 1891 (1988); **58**, 3869 (1989).
11. D. V. Dmitriev, V. Ya. Krivnov, and A. A. Ovchinnikov, Phys. Rev. B **61**, 14592 (2000).

Poles of Structural Factor and Secondary Emission from a Semi-Infinite Crystal¹

V. N. Peregudov and V. M. Manichev

Kurchatov Institute Russian Research Center, pl. Kurchatova 1, Moscow, 123182 Russia

Received June 19, 2000

Secondary emission from a semi-infinite crystal is considered. The contribution to the emission amplitude originating from structural factor singularities is analyzed. Poles of the structural factor determine the main contribution to the emission amplitude. The energy and angular distributions of the emission depend on the crystallographic orientation of the crystal surface and are characterized by a set of allowed vectors of the reciprocal lattice. It is shown that emission anisotropy related to the crystallographic directions is due to the coherent character of the photoabsorption process, and diffraction scattering leads only to relative change in the emission intensity in allowed low-index directions. The concrete calculations are performed for (100) and (111) surfaces of a diamond-like lattice. © 2000 MAIK “Nauka/Interperiodica”.

PACS numbers: 61.14.-x; 78.70.-g

Photo-, Auger and fluorescence emissions from X-ray irradiated crystals are intensively used for structure reconstruction on a crystal surface. Development of experimental facilities in this field allows one to obtain information concerning the surface structure of irradiated crystals [1–5]. Application of these emissions for crystal holography is also widely discussed [6–11]. Characteristic features of the angular distribution of the emission investigated in the papers cited above are interpreted as a result of diffraction scattering. Several authors tried to analyze interference between direct and scattered emissions from individual atoms (see [12] and ref. therein). Mathematical methods of structure reconstruction were also developed. Parallel with new holographic schemes, some refined methods, such as a Patterson-like scheme were proposed [13]. Discussed schemes of structure reconstruction based on measuring the angular and energy distributions of emission take into account scattering by individual atoms as independent scatterers and do not take into account the periodic nature of the scattering potential. Correct determination of the positions of displacement atoms near a crystal surface makes it desirable to have for comparison emission scattered by the periodic potential of a semi-infinite perfect crystal. In this paper, analysis of anisotropy of the secondary emission from a single semi-infinite crystal under X-ray irradiation is proposed.

During emission registration experiments, it is not possible to distinguish between the atom emitter and atom scatterer. Therefore, in the case of identical atoms, it is convenient to consider an amplitude of the emission probability which depends only on the emission wave vector \mathbf{k} , which determines the energy and

direction of the measured emission. It is known that the scattering potential acting on the electrons in a crystal is a sum of all atomic potentials. A Fourier transform of this potential $U(\mathbf{q})$, which determines the scattering with transferred momentum \mathbf{q} , is given by

$$U(\mathbf{q}) = V(\mathbf{q})S(\mathbf{q}). \quad (1)$$

Here, $V(\mathbf{q})$ is the atomic factor; $S(\mathbf{q}) = \sum_n \exp(i(\mathbf{q}\mathbf{r}_n))$ is the structural factor (SF) of a semi-infinite crystal; \mathbf{r}_n is an atomic position; and the summation is taken over all atomic positions with $z_n \leq 0$, where the z axis of a Cartesian coordination system is directed along the external normal to the irradiated surface. Equation (1) does not take into account thermal atomic motion which leads to the Debye–Waller factor in this equation. The finite summation limit over $z_n \leq 0$ in SF determines the influence of crystallographic orientation of the surface. The explicit form of the \mathbf{q} -dependence of SF can be obtained through the layer-by-layer summation for the investigated lattice and given surface orientation. It is known that $V(\mathbf{q})$ does not have singularities, and a change in the wave vector \mathbf{k}' in the scattering is determined by the poles \mathbf{q}_{jlm} of $S(\mathbf{q})$, which are a subset of the total set of vectors of the reciprocal lattice. This set depends strongly on the crystallographic orientation of the crystal surface. Below, the diamond-like lattice is taken as an example to demonstrate the dependence of the set on the surface crystallography.

The concrete calculations fulfilled for the important case of the (100) surface of the diamond-like lattice allow one to obtain the explicit form of SF. It has the following form:

$$S_{100}(\mathbf{q}) = \left(4 \cos \frac{q_x a}{4} \cos \frac{q_y a}{4} \cos \frac{q_z a}{4} \right)^{-1}. \quad (2)$$

¹ This article was submitted by the authors in English.

Here, a is the size of a unit cell of the diamond-like lattice. This equality shows the presence of poles at

$$\mathbf{q}_{jlm} = (2j + 1, 2l + 1, 2m + 1)2\pi/a, \quad (3)$$

where j, l, m are integers. In the case of a weakly scattering potential, $U_s \ll E$, where E is the electron energy, the pole singularities of SF (2) allow the calculation of emission amplitude accounting for elastic scattering by the periodic potential in the Born approximation (BA) [14]. Let $F(\mathbf{k})$ be the probability amplitude of nonscattered emission. Then taking account of scattering leads to the following form of the emission amplitude:

$$G(\mathbf{k}) = F(\mathbf{k}) + W(\mathbf{k})/E, \quad (4)$$

where

$$W(\mathbf{k}) = \sum_{jlm} b_{jlm}^{(1)} F(\mathbf{k} - \mathbf{q}_{jlm}) + \sum_{jlm} b_{jlm}^{(2)} F(\mathbf{k} - 2\mathbf{q}_{jlm}) + \dots$$

has the meaning of the effective scattering potential of the semi-infinite crystal, which takes into account the momentum transfer multiple for all allowed \mathbf{q}_{jlm} . Calculation of the first two coefficients in the BA gives

$$b_{jlm}^{(1)} = \frac{32\sqrt{\pi}}{ea^3} (-1)^{j+l+m} V(\mathbf{q}_{jlm}), \quad (5)$$

$$b_{jlm}^{(2)} = i \frac{512\sqrt{\pi} V^2(\mathbf{q}_{jlm})}{3ea^6 E_{jlm}}.$$

Here,

$$E_{j,l,m} = \frac{\hbar^2 \mathbf{q}_{jlm}^2}{2m_e} \quad (6)$$

$$= 2E_s^e [(2j + 1)^2 + (2l + 1)^2 + (2m + 1)^2],$$

$E_s^e = \text{Ry}(\pi a_B/a)^2$, Ry is Rydberg's energy and a_B is the Bohr radius, and m_e is the electron mass. The second term on the right hand side of Eq. (4) describes multiple scattering as a series expansion in the scattering potential. The summation in $W(\mathbf{k})$ goes over all poles of SF, which satisfy the conditions $(\mathbf{k} - \mathbf{q}_{jlm})^2 = \mathbf{k}^2$ and $(\mathbf{k} - 2\mathbf{q}_{jlm})^2 = \mathbf{k}^2$ in the first and second orders of BA, respectively. In particular, it means that the emission amplitude with the wave vectors $\mathbf{k} = \mathbf{q}_{jlm}$ is preserved during scattering in the first order of BA. Equations (4) and (5) show that in the case of an isotropic form of the amplitude $F(\mathbf{k})$, elastic scattering preserves the isotropy in the emission intensity $|G(\mathbf{k})|^2$. This leads to the conclusion that anisotropy appearing in experimental data and related to the crystal structure [15] is formed in the process of photoabsorption and not in the diffraction scattering. There are two possible causes of this anisotropy. The first one is the coherent character of the

photoabsorption related to the crystal atomic structure. The second cause of the anisotropy of $F(\mathbf{k})$ is due to anisotropy of the photoprocess in an individual atom and can be due to the polarization of the X-ray beam and to the initial electron state in an individual atom. This second cause is in no way related to the crystalline structure. Thus, the experimental data of [15] can be considered as an indication of the coherent character of the photoabsorption process. It is possible to show that in the case of coherent photoabsorption, when $F(\mathbf{k}) \sim S(\mathbf{k})$ and all Fourier transforms of the amplitude $F(\mathbf{k})$ correspond to the poles of SF, the first order of BA does not contribute to the elastic scattering and the second order of BA leads only to a relative change in emission intensity in allowed low-index directions.

The positions of the poles of SF in the \mathbf{k} space are determined by the crystal symmetry and surface orientation. Let $[2j + 1, 2l + 1, 2m + 1]$ designate a multiplet of reciprocal vectors corresponding to equal energy (6). In the general case, it corresponds to 48 different poles in the \mathbf{k} space. These poles form a 48-et with six different wave vectors in each octant of the \mathbf{k} space. In the case when, e.g., $q_\alpha = q_\beta \neq q_\gamma$, the poles form a 24-et with three different wave vectors in each octant of the \mathbf{k} space. The spatial diagonals of the octants are threefold axes for this wave-vector system. In the case when $F(\mathbf{k}) \sim S(\mathbf{k})$, the poles form an octet with wave vectors directed along the spatial diagonals. The lowest energy octet of such states has energy $E_{[1,1,1]} = 6E_s^e$ (~ 18 eV in the case of Si). The next energy state is a 24-et and has the energy $E_{[1,1,3]} = 22E_s^e$ (~ 66 eV in the case of Si). The lowest energy 48-et has the energy $E_{[1,3,5]} = 70E_s^e$ (~ 210 eV in the case of Si).

In the case of the diamond-like lattice, a normal to a (111) surface is the threefold symmetry axis. In this case, layer-by-layer calculation of SF leads to the following expression:

$$S_{111}(\mathbf{q}) \sim -i \exp\left(\frac{iq a_0}{2}\right) \times \left[4 \sin \frac{q a_0}{6} \cos \frac{q a_0}{3}\right]^{-1} \delta\left(\frac{\mathbf{q}}{q} - \mathbf{n}_z\right). \quad (7)$$

Here, $a_0 = \sqrt{3}a/4$ is the minimum distance between atoms in the diamond-like lattice with the size of a unit cell equal to a . Note that the summation over any monolayer, which is parallel to a (111) surface, gives the same result, equal to 0, for all directions except for the normal one. In this case, the diffraction scattering changes only the z component of the wave vector.

The presence of this single direction of \mathbf{q} is the result of interference. The poles at

$$\mathbf{q}_j = (0, 0, j) \frac{6\pi}{a_0}, \quad \mathbf{q}_l = (0, 0, 2l + 1) \frac{3\pi}{2a_0} \quad (8)$$

lead to a sharp increase in the scattering along the normal direction to the (111) surface for these wavelengths. The electrons with energies

$$E_j = 96j^2 E_s^e, \quad E_l = 6(2l+1)^2 E_s^e, \quad (9)$$

give the main contribution to the emission. In this case, all poles form doublets. The characteristic distance between two lowest levels for the (111) surface of Si is ~ 36 eV.

In the case of fluorescence emission from the (100) surface, the main contribution can be expected to be from energies

$$E_{j,l,m}^f = E_s^f [(2j+1)^2 + (2l+1)^2 + (2m+1)^2]^{1/2}, \quad (10)$$

and, in the case of the (111) surface,

$$E_j^f = 4\sqrt{3}jE_s^f, \quad E_l^f = \sqrt{3}(2l+1)E_s^f. \quad (11)$$

Here, $E_s^f = 2\pi\alpha R y(a_B/a)$ determines the energy scale for the fluorescence emission and $\alpha = c\hbar/e_0^2 = 137$. The characteristic value of E_s^f equals ~ 2300 eV, while $E_s^f \sim 3$ eV.

Thus, we see that the influence of diffraction scattering on the emission anisotropy depends on the crystallographic orientation of the crystal surface. Equations (4) and (5) allow one to estimate the contribution of diffraction scattering to the electron emission. The contributions of inelastic processes, in particular plasmon excitations, can be easily estimated by experimental data from [15]. Similar angle dependences of the electron emission measured in [15] for elastic and satellite plasmon peaks indicate that they are related to the same poles of SF. Relatively small energy losses of the electrons due to the excitation of plasma oscillations are considerably smaller than the energy intervals between

neighboring multiplets (6), and angular distributions of electrons, both excited and unexcited plasmons, are formed by the same multiplet of reciprocal vectors.

This work was supported by the Russian Foundation for Basic Research, project no. 00-02-17693.

REFERENCES

1. K. Robinson and D. J. Tweet, Rep. Prog. Phys. **55**, 599 (1992).
2. C. S. Fadley, Phys. Scr., T **17**, 39 (1987).
3. M.-L. Xu and M. A. van Hove, Surf. Sci. **207**, 215 (1989).
4. I. H. Hong, S. C. Shyu, Y. C. Chou, and C. M. Wei, Phys. Rev. B **52**, 16884 (1995).
5. P. M. Len, J. D. Denlinger, E. Rotenberg, *et al.*, Phys. Rev. B **59**, 5857 (1999).
6. P. M. Len, S. Thevuthasan, C. S. Fadley, *et al.*, Phys. Rev. B **50**, 11275 (1994).
7. Hua Li, S. Y. Tong, D. Naumovic, *et al.*, Phys. Rev. B **47**, 10036 (1993).
8. S. Thevuthasan, R. X. Ynzunza, E. D. Tober, *et al.*, Phys. Rev. Lett. **70**, 595 (1993).
9. D. K. Saldin, K. Reuter, P. L. de Andres, *et al.*, Phys. Rev. B **54**, 8172 (1996).
10. T. Gog, P. M. Len, G. Materlik, *et al.*, Phys. Rev. Lett. **76**, 3132 (1996).
11. P. M. Len, T. Gog, C. S. Fadley, and G. Materlik, Phys. Rev. B **55**, R3323 (1997).
12. H. Wu, G. J. Lapeyer, H. Huang, and S. Y. Tong, Phys. Rev. Lett. **71**, 251 (1993).
13. C. Y. Chang, Z. C. Lin, Y. C. Chou, and C. M. Wei, Phys. Rev. Lett. **83**, 2580 (1999).
14. L. D. Landau and E. M. Lifshitz, *Course of Theoretical Physics*, Vol. 3: *Quantum Mechanics: Non-Relativistic Theory* (Nauka, Moscow, 1974; Pergamon, Oxford, 1977).
15. E. Puppini, C. Carbone, and R. Rochow, Phys. Rev. B **46**, 13215 (1992).

Soliton Management in the Nonlinear Schrödinger Equation Model with Varying Dispersion, Nonlinearity, and Gain¹

V. N. Serkin* and A. Hasegawa**

Institute of General Physics, Russian Academy of Sciences, ul. Vavilova 38, Moscow, 117942 Russia
*e-mail: vserkin@hotmail.ru

Benemerita Universidad Autonoma de Puebla, 72001 Puebla, Pue., Mexico

** *Soliton Communications, Higashiyama-ku, Kyoto, 605-0035, Japan*

Received June 16, 2000

The novel stable “soliton islands” in a “sea of solitary waves” of the nonlinear Schrödinger equation model with varying dispersion, nonlinearity, and gain or absorption are discovered. Different soliton management regimes are predicted. © 2000 MAIK “Nauka/Interperiodica”.

PACS numbers: 42.65.Tg; 05.45.Yv; 42.81.Dp

The nonlinear Schrödinger equation model (NLSE) is one of the most important and “universal” nonlinear models of modern science. NLSE appears in many branches of physics and applied mathematics, including condensed matter and plasma physics, nonlinear optics and quantum electronics, fluid mechanics, theory of turbulence and phase transitions, biophysics, and star formation. The best known solutions of the NLSE are those for solitary waves, or solitons. The theory of NLSE solitons was developed for the first time in 1971 by Zakharov and Shabat [1]. Zakharov and Shabat were the first to apply the inverse scattering transform method to this equation and derived a more general form for its bright, dark, and multisoliton solutions [1, 2]. Over the years, not only was experimental verification of the existence of NLSE solitons in many branches of modern science demonstrated, but also various properties of solitons derivable from the result of the inverse scattering transform theory were identified. Hasegawa and Tappert [3] were the first to show theoretically that an optical pulse in a dielectric fiber forms a solitary wave, based on the fact that the wave envelope satisfies the NLSE. Optical solitons were discovered experimentally in 1980 by Mollenauer, Stolen, and Gordon [4]. Today, optical solitons are regarded as the natural data bits and as an important alternative to the next generation of ultrahigh-speed optical telecommunication systems [5]. Picosecond optical soliton theory, developed in the framework of the NLSE model, has produced an excellent agreement between theory and experiment [6, 7].

The problem of soliton management in the nonlinear systems described by the NLSE model with varying coefficients is a new and important one (see, e.g., the review of optical soliton dispersion management principles and research as it currently stands in [8–10], and

references therein). We would also note the fact that the first soliton dispersion management experiment in a fiber with hyperbolically decreasing group velocity dispersion was realized as early as in 1991 by Dianov's group at the General Physics Institute [11].

In this letter, we predict the existence of a new type of temporal and spatial solitary waves for the NLSE model with varying dispersion, nonlinearity, and gain or absorption. We will then turn our attention to finding solutions for specified soliton management conditions. Different soliton management regimes are predicted.

Our starting point is the NLSE model with varying coefficients:

$$i \frac{\partial q^\pm}{\partial Z} \pm \frac{1}{2} D_2(Z) \frac{\partial^2 q^\pm}{\partial T^2} + N_2(Z) |q^\pm|^2 q^\pm = i \Gamma(Z) q^\pm. \quad (1)$$

NLSE (1) is written here in standard soliton units, as they are commonly known. There it is assumed that the perturbations to the dispersion parameter $D_2(Z)$, nonlinearity $N_2(Z)$, and to the amplification or absorption coefficient $\Gamma(Z)$ are not limited to the regime where they are smooth and small. Due to the well-known spatiotemporal analogy [1], both temporal and spatial solitons are described by Eq. (1). In the case of temporal solitons, T is the dimensionless time in the retarded frame associated with the group velocity of wave packets at a particular optical carrier frequency. In the case of two-dimensional spatial solitons, $T = X$ represents a transverse coordinate.

Theorem 1. Consider the NLSE model (1) with varying dispersion, nonlinearity, and gain or absorption. Suppose that the Wronskian $W\{N_2, D_2\}$ of the functions $N_2(Z)$ and $D_2(Z)$ does not vanish; the two functions $N_2(Z)$ and $D_2(Z)$ are thus linearly independent. Then there is an infinite number of solitary-wave

¹ This article was submitted by the authors in English.

solutions for Eq. (1) written in the following form:

$$q^\pm(Z, T) = \sqrt{\frac{D_2(Z)}{N_2(Z)}} P(Z) Q^\pm[P(Z)T] \times \exp\left[\pm i \frac{P(Z)}{2} T^2 + i \int_0^Z K^\pm(Z') dZ'\right], \quad (2)$$

where the real function $Q^\pm(S)$ describes the canonical functional form of bright [$\text{sgn} = +1$, $Q^+(S) = \eta \text{sech}(\eta P(Z)T)$] or dark [$\text{sgn} = -1$, $Q^-(S) = \eta \tanh(\eta P(Z)T)$] NLSE solitons [1–3], and the real functions $D_2(Z)$, $N_2(Z)$, $\Gamma(Z)$, and $P(Z)$ satisfy the system of equations

$$\begin{aligned} \frac{\partial P(Z)}{\partial Z} + P^2(Z)D_2(Z) &= 0; \\ \frac{W\{N_2(Z), D_2(Z)\}}{D_2(Z)N_2(Z)} - D_2(Z)P(Z) &= 2\Gamma(Z). \end{aligned} \quad (3)$$

Theorem 2. Consider the NLSE model (1) with varying dispersion, nonlinearity, and gain or absorption. Suppose that the Wronskian $W\{N_2, D_2\}$ vanishes; the two functions $N_2(Z)$ and $D_2(Z)$ are thus linearly dependent. Then there is an infinite number of solitary-wave solutions conserving the pulse area for Eq. (1):

$$q^\pm(Z, T) = CP(Z)Q^\pm[P(Z)T] \times \exp\left[\pm i \frac{P(Z)}{2} T^2 + i \int_0^Z K^\pm(Z') dZ'\right], \quad (4)$$

where the real functions $Q^\pm(S)$ describe a canonical form of bright ($Q^+(S)$) or dark ($Q^-(S)$) NLSE solitons, and the real functions $P(Z)$, $D_2(Z)$, $N_2(Z)$ and $\Gamma(Z)$ satisfy the system of equations

$$\begin{aligned} 2\Gamma(Z) &= \frac{1}{P} \frac{\partial P(Z)}{\partial Z}; \\ C^2 N_2(Z) = D_2(Z) &= -\frac{1}{P^2(Z)} \frac{\partial P(Z)}{\partial Z}. \end{aligned} \quad (5)$$

The explicit solutions for the traveling solitary waves can easily be constructed by applying the Galileian transformations and by using the equation for the ‘‘soliton center’’ $T_{sol}(Z)$ given by

$$\partial T_{sol}(Z)/\partial Z = -VD_2(Z), \quad (6)$$

where V is the soliton group velocity (in the case of a spatial soliton, $V = \tan\theta$ and θ is the angle of propagation in the XZ plane).

By applying Theorems 1 and 2, we develop a systematic analytical approach to find the fundamental set of the different NLSE soliton management regimes.

Case 1. Soliton dispersion management. In this case, the dispersion management function $D_2(Z)$ is

assumed to be given: $D_2(Z) = \Phi(Z)$ (we call it the control function). The function $\Phi(Z)$ is only required to be once differentiable and once integrable, but is an otherwise arbitrary function; there are no restrictions. Then there is an infinite number of solutions for Eq. (1) of the form of bright and dark dispersion-managed solitons represented by Eq. (2), where the main functions $P(Z)$ and $\Gamma(Z)$ are given by

$$\begin{aligned} P(Z) &= -\frac{1}{[C - \int \Phi(Z) dZ]}, \\ \Gamma(Z) &= \frac{1}{2} \frac{\partial}{\partial Z} \ln\left(\left|\frac{P(Z)\Phi(Z)}{N_2(Z)}\right|\right). \end{aligned} \quad (7)$$

In the limit $N(Z) = \text{const}$, Eq. (7) reduces to

$$\Gamma(Z) = \frac{1}{2} \frac{\Phi(Z)}{[C - \int \Phi(Z) dZ]} + \frac{1}{2} \frac{1}{\Phi(Z)} \frac{\partial \Phi(Z)}{\partial Z}, \quad (8)$$

where C is the constant of integration.

Case 2. Soliton energy control. In this case, the soliton energy-control function $E(Z) = 2D_2(Z)P(Z)/N_2(Z)$ is assumed to be given. The function $E(Z)$ is only required to be once differentiable and once integrable, but is an otherwise arbitrary function; there are no restrictions. Then there is an infinite number of solutions for Eq. (1) of the form of bright and dark solitons represented by Eq. (2), where the main functions $D_2(Z)$, $P(Z)$, and $\Gamma(Z)$ are given by

$$D_2(Z) = \frac{E(Z)N_2(Z)}{2P(Z)} \quad (9)$$

$$2\Gamma(Z) = \frac{\partial}{\partial Z} \ln(E(Z)/2),$$

$$P(Z) = \pm \exp\left[-\frac{1}{2} \int E(Z)N_2(Z) dZ + C\right]. \quad (10)$$

Case 3. Soliton intensity management. In this case, the soliton pulse intensity (peak power) is assumed to be controlled by the function $\Theta(Z) = D_2(Z)P^2(Z)/N_2(Z)$, where the control function $\Theta(Z)$ is only required to be once differentiable and once integrable. Then there is an infinite number of solutions for Eq. (1) of the form of bright and dark solitons represented by Eq. (2), where the main functions $D_2(Z)$, $P(Z)$, and $\Gamma(Z)$ are given by quadratures:

$$\begin{aligned} D_2(Z) &= \frac{\Theta(Z)}{[C - \int \Theta(Z) dZ]^2}; \\ P(Z) &= -\int \Theta(Z) dZ + C, \end{aligned} \quad (11)$$

$$2\Gamma(Z) = \frac{\Theta(Z)}{[C - \int \Theta(Z) dZ]} + \frac{1}{\Theta(Z)} \frac{\partial \Theta(Z)}{\partial Z},$$

and the nonlinearity is assumed to be a constant [$N_2(Z) \equiv 1$].

Case 4. Soliton pulse width management and the problem of optimal soliton compression. In this case, the soliton pulse width control function is assumed to be given: $Y(Z) = P^{-1}(Z)$. The real function $Y(Z)$ is only required to be twice differentiable, but is an otherwise arbitrary function; there are no restrictions. Then there is an infinite number of solutions for Eq. (1) of the form of bright and dark solitons represented by Eq. (2), where the main coefficients of the NLSE model $D_2(Z)$ and $\Gamma(Z)$ are given by

$$D_2 = \frac{\partial Y}{\partial Z}; \quad 2\Gamma(Z) = -\frac{1}{Y} \frac{\partial Y}{\partial Z} + \left(\frac{\partial Y}{\partial Z}\right)^{-1} \frac{\partial^2 Y}{\partial Z^2}. \quad (12)$$

Case 5. Soliton amplification management and the problem of optimal soliton amplification. In this case, the gain (or loss) function $\Gamma(Z)$ is assumed to be given: $\Gamma(Z) = \Lambda(Z)$. The gain control function $\Lambda(Z)$ is only required to be once integrable. Then there is an infinite number of solutions for Eq. (1) of the form of bright and dark solitons represented by Eq. (2), where the main functions $D_2(Z)$ and $P(Z)$ are given by quadratures:

$$|P(Z)||D_2(Z)| = \exp\left[\int 2\Lambda(Z)dZ + C_1\right], \quad (13)$$

$$|D_2| = \exp\left\{\int [2\Lambda(Z) \pm |P(Z)||D_2(Z)|]dZ + C_2\right\}, \quad (14)$$

where the integration constants $C_{1,2}$ are determined by the initial conditions.

Case 6. Combined nonlinear and dispersion soliton management regimes. In this case, the Wronskian $W\{N_2, D_2\}$ is assumed to vanish, which means that the nonlinearity and dispersion are linearly dependent functions. The main feature of soliton solutions given by Theorem 2 consists in the fact that the soliton pulse area is conserved during propagation. Suppose that the dispersion management function $D_2(Z)$ is determined by the known control function $D_2(Z) = \Xi(Z)$, where the function $\Xi(Z)$ is only required to be once integrable. Then there is an infinite number of solutions for Eq. (1) of the form of bright and dark conserving pulse area dispersion-managed solitons represented by Eq. (4), where the main functions $D_2(Z)$, $P(Z)$, $N_2(Z)$, and $\Gamma(Z)$ are given by quadratures:

$$P(Z) = -1/[C - \int \Xi(Z)dZ] \quad (15)$$

$$N_2(Z) = D_2(Z)/C^2,$$

$$2\Gamma(Z) = \Xi(Z)/[C - \int \Xi(Z)dZ]. \quad (16)$$

The interested reader can take different control functions $\Phi(Z)$ [Eqs. (7), (8)]; $E(Z)$ [Eqs. (9), (10)]; $\Theta(Z)$ [Eq. (11)]; $Y(Z)$ [Eq. (12)]; $\Lambda(Z)$ [Eqs. (13), (14)]; and $\Xi(Z)$ [Eqs. (15), (16)] to find the novel ‘‘soliton islands’’ in a ‘‘sea of solitary waves’’ for the NLSE

model (1) by using algorithms developed in this work. The soliton management scenario is determined by the indefinite integrals in Eqs. (7)–(16), which are elementary for practically any of the best known elementary functions [considered here as a probe control or management functions $\Phi(Z)\dots\Xi(Z)$: rational, algebraic, exponential and hyperbolic, trigonometric and logarithmic, and their combinations. We will present the most interesting (from the application point of view) examples in a separate publication.

The main soliton features of the predicted analytical solutions were investigated by using direct computer simulations with an accuracy as high as 10^{-9} . In future publications, we will show that the predicted managed solitary waves not only interact elastically, but they can also form the bound states, and these bound states split under weak perturbations.

Recently, Zakharov and Manakov [12] showed that, in the strong dispersion-managed nonlinear system, the leading nonlinear effect is the formation of a collective average dispersion which is a result of the interaction of all soliton pulses propagating along the optical fiber communication line, and, in the leading order, the system is described by an integrable Hamiltonian system with a plethora of soliton solutions. It was shown that, due to the formation of an additional collective dispersion, each pulse in the line generates long tails that influence the shapes of the other pulses, and the pulses feel each other when separated by an arbitrary long distance [12].

The methodology developed in this letter (Theorems 1, 2) provides a systematic way to discover and investigate another class of managed solitons with canonical bright and dark soliton pulse profiles. The surprising aspect is that analytical solutions are obtained here in quadratures. Their pure soliton-like features are confirmed by accurate direct computer simulations. We should also note that solitary waves for the NLSE model (1) must be of a rather more general character than canonical solitons for the standard NLSE model with constant coefficients, because the generalized model (1) takes into account arbitrary variations of group velocity dispersion $D_2(Z)$, nonlinearity $N_2(Z)$, and gain (or absorption) $\Gamma(Z)$. The results obtained in this letter are of general physics interest and should be readily experimentally verified.

We would like to express special gratitude to Prof. V.E. Zakharov for reading and commenting on the entire manuscript and fruitful suggestions. Special thanks are due to Prof T.H. Tieman for careful checking of the manuscript.

REFERENCES

1. V. E. Zakharov and A. B. Shabat, Zh. Éksp. Teor. Fiz. **61**, 118 (1971) [Sov. Phys. JETP **34**, 62 (1972)].
2. V. E. Zakharov and A. B. Shabat, Zh. Éksp. Teor. Fiz. **64**, 1627 (1973) [Sov. Phys. JETP **37**, 823 (1973)].

3. A. Hasegawa and F. Tappert, *Appl. Phys. Lett.* **23**, 142 (1973); **23**, 171 (1973).
4. L. F. Mollenauer, R. G. Stolen, and J. P. Gordon, *Phys. Rev. Lett.* **45**, 1095 (1980).
5. A. Hasegawa and Y. Kodama, *Solitons in Optical Communications* (Clarendon, Oxford, 1995).
6. *Optical Solitons—Theory and Experiment*, Ed. by J. R. Taylor (Cambridge Univ. Press, Cambridge, 1992).
7. G. P. Agrawal, *Nonlinear Fiber Optics* (Academic, New York, 1995; Mir, Moscow, 1996).
8. A. Hasegawa, *Physica D (Amsterdam)* **123**, 267 (1998).
9. T. I. Lakoba and D. J. Kaup, *Phys. Rev. E* **58**, 6728 (1998).
10. S. K. Turitsyn and E. G. Shapiro, *J. Opt. Soc. Am. B* **16**, 1321 (1999).
11. V. A. Bogatyrev, M. M. Bubnov, E. M. Dianov, *et al.*, *J. Lightwave Technol.* **9**, 561 (1991).
12. V. E. Zakharov and S. V. Manakov, *Pis'ma Zh. Éksp. Teor. Fiz.* **70**, 573 (1999) [*JETP Lett.* **70**, 578 (1999)].

Two-Particle Spin States and Generalized Bell's Inequalities

V. A. Andreev and V. I. Man'ko*

Lebedev Physical Institute, Russian Academy of Sciences, Leninskiĭ pr. 53, Moscow, 117924 Russia

*e-mail: *manko@astra.na.astro.it*

Received June 7, 2000

A new formalism for calculation of the spin correlation magnitude is developed. In this approach, the mean value of an operator acting in the four-dimensional space of two-particle spin states has the form of a scalar product of vectors defined in the three-dimensional direction space. A complete description of the two-particle spin states satisfying Bell inequalities is given in this formalism. It is shown that these states include both factorable and entangled states. © 2000 MAIK "Nauka/Interperiodica".

PACS numbers: 03.65.Bz

The Einstein–Podolsky–Rosen (EPR) paradox [1, 2] is often formulated in terms of Bell inequalities [3, 4] which are verified by the comparison of theory with experiment. In connection with Bell inequalities, much attention is given to two-particle quantum states and to the question as to for which of them the Bell inequalities are fulfilled and for which they are not [5–14]. The class of specific “entangled” states was distinguished which are essentially quantum objects and are precisely those for which the Bell inequalities were expected to be violated.

In this work, a complete description is given for the two-particle spin states for which the Bell inequalities are fulfilled. It is shown that the entangled states also belong to these states. We employ the standard formulation of quantum mechanics and specify quantum states in terms of wave functions and density matrices. The tomographic description of one-particle spin states was given in [15, 16]; for the two-particle states, a similar problem was solved in [17]; and the EPR paradox was discussed in terms of quantum tomography in [18].

Let there be only one spin, for which the “up” and “down” spin directions along the Z axis are denoted by $|+\rangle$ and $Z-|-\rangle$, respectively. Spin operators are specified on these vectors by the relationships

$$\begin{aligned} S_x|+\rangle &= \frac{1}{2}|-\rangle, & S_x|-\rangle &= \frac{1}{2}|+\rangle, \\ S_y|+\rangle &= \frac{i}{2}|-\rangle, & S_y|-\rangle &= -\frac{i}{2}|+\rangle, \\ S_z|+\rangle &= \frac{1}{2}|+\rangle, & S_z|-\rangle &= -\frac{1}{2}|-\rangle. \end{aligned} \quad (1)$$

The \hat{a} operator of a doubled spin projection onto the direction specified by vector $\mathbf{a} = (a_x, a_y, a_z)$ has the form

$$\hat{a} = 2(\mathbf{a}, \mathbf{S}) = 2(a_x S_x + a_y S_y + a_z S_z). \quad (2)$$

For the two-particle states, one can introduce the operator [4]

$$\hat{a} \otimes \hat{b} = 4(\mathbf{a}, \mathbf{S}^{(1)}) \otimes (\mathbf{b}, \mathbf{S}^{(2)}), \quad (3)$$

defined in a four-dimensional linear space with basis vectors

$$\begin{aligned} \Psi_{++} &= |(1+)\rangle|(2+)\rangle, & \Psi_{+-} &= |(1+)\rangle|(2-)\rangle, \\ \Psi_{-+} &= |(1-)\rangle|(2+)\rangle, & \Psi_{--} &= |(1-)\rangle|(2-)\rangle. \end{aligned} \quad (4)$$

Operator (3) corresponds to the observable called the spin correlation. Let us study its properties. In basis (4), operator (3) has the following matrix form:

$$\hat{a} \otimes \hat{b} = \begin{pmatrix} a_z b_z & a_z(b_x - ib_y) & (a_x - ia_y)b_z & (a_x - ia_y)(b_x - ib_y) \\ a_z(b_x + ib_y) & -a_z b_z & (a_x - ia_y)(b_x + ib_y) & -(a_x - ia_y)b_z \\ (a_x + ia_y)b_z & (a_x + ia_y)(b_x - ib_y) & -a_z b_z & -a_z(b_x - ib_y) \\ (a_x + ia_y)(b_x + ib_y) & -(a_x + ia_y)b_z & -a_z(b_x + ib_y) & a_z b_z \end{pmatrix}. \quad (5)$$

If the two-particle spin state in basis (4) is described by the density matrix

$$\rho = \|\rho_{ij}\|, \quad i, j = 1, 2, 3, 4, \quad (6)$$

then the spin correlation can be represented as

$$P = \|P_{ij}\| = \begin{pmatrix} (\rho_{14} + \rho_{23} + \rho_{32} + \rho_{41}) & i(\rho_{14} - \rho_{23} + \rho_{32} - \rho_{41}) & (\rho_{13} + \rho_{31} - \rho_{24} - \rho_{42}) \\ i(\rho_{14} + \rho_{23} - \rho_{32} - \rho_{41}) & (-\rho_{14} + \rho_{23} + \rho_{32} - \rho_{41}) & i(\rho_{13} - \rho_{31} - \rho_{24} + \rho_{42}) \\ (\rho_{12} + \rho_{21} - \rho_{34} - \rho_{43}) & i(\rho_{12} - \rho_{21} - \rho_{34} + \rho_{43}) & (\rho_{11} - \rho_{22} - \rho_{33} + \rho_{44}) \end{pmatrix}. \quad (8)$$

In analyzing the many-particle states, it is often worthwhile to divide them into three classes: factorable, separable, and entangled. The factorable states are the states whose density matrix ρ_f can be represented as a tensor product of the density matrices of its subsystems:

$$\rho_f = \rho^\alpha \otimes \rho^\beta. \quad (9)$$

The states whose density matrix $\rho_{\Sigma f}$ can be represented as a sum of factorable density matrices are called separable:

$$\rho_{\Sigma f} = \sum_i^n \rho_i^\alpha \otimes \rho_i^\beta. \quad (10)$$

The entangled states are the states whose density matrices ρ_e can be represented neither as (9) nor as (10). In the case of two-particle systems, ρ^α and ρ^β are the density matrices of one and the other particles, respectively. The states ρ_f , ρ^α , and ρ^β , as well as the ρ_e states, may be both pure and mixed. For the factorable states, Eq. (7) for spin correlation can be simplified. Let

$$\rho_f = \rho^\alpha \otimes \rho^\beta = \begin{pmatrix} \rho_{11}^\alpha & \rho_{12}^\alpha \\ \rho_{21}^\alpha & \rho_{22}^\alpha \end{pmatrix} \otimes \begin{pmatrix} \rho_{11}^\beta & \rho_{12}^\beta \\ \rho_{21}^\beta & \rho_{22}^\beta \end{pmatrix}. \quad (11)$$

Then, matrix (8) can be represented as a product of two matrices:

$$P = (P^\alpha)^T P^\beta = \begin{pmatrix} (\rho_{12}^\alpha + \rho_{21}^\alpha) & 0 & 0 \\ i(\rho_{12}^\alpha - \rho_{21}^\alpha) & 0 & 0 \\ (\rho_{11}^\alpha - \rho_{22}^\alpha) & 0 & 0 \end{pmatrix} \times \begin{pmatrix} (\rho_{12}^\beta + \rho_{21}^\beta) & i(\rho_{12}^\beta - \rho_{21}^\beta) & (\rho_{11}^\beta - \rho_{22}^\beta) \\ 0 & 0 & 0 \\ 0 & 0 & 0 \end{pmatrix}. \quad (12)$$

$$E(\mathbf{a}, \mathbf{b}) = \text{Sp}(\hat{a} \otimes \hat{b} \rho)$$

$$= (a_x \ a_y \ a_z) P \begin{pmatrix} b_x \\ b_y \\ b_z \end{pmatrix} = (\mathbf{a}, P\mathbf{b}), \quad (7)$$

where P is the 3×3 matrix

For such ρ_f matrices, the mean (7) takes the form

$$E(\mathbf{a}, \mathbf{b}) = \text{Sp}(\hat{a} \otimes \hat{b} \rho) = (P^\alpha \mathbf{a}, P^\beta \mathbf{b}) = (\mathbf{r}^\alpha, \mathbf{a})(\mathbf{r}^\beta, \mathbf{b}), \quad (13)$$

where

$$\mathbf{r}^\alpha = ((\rho_{12}^\alpha + \rho_{21}^\alpha), i(\rho_{12}^\alpha - \rho_{21}^\alpha), (\rho_{11}^\alpha - \rho_{22}^\alpha)).$$

It follows from Eq. (8) that the matrix corresponding to state (10) is

$$P_{\Sigma f} = \sum_i^n P_i = \sum_i^n (P_i^\alpha)^T P_i^\beta, \quad (14)$$

where $(P_i^\alpha)^T$ and P_i^β are matrices of the form (12).

Let there be a source emitting pairs of particles forming a certain two-particle state and let \mathbf{a} , \mathbf{b} , \mathbf{c} , and \mathbf{d} be four arbitrarily chosen directions. The Bell inequality for the two-particle spin states has the form

$$|E(\mathbf{a}, \mathbf{b}) + E(\mathbf{a}, \mathbf{c}) + E(\mathbf{d}, \mathbf{b}) - E(\mathbf{d}, \mathbf{c})| \leq 2. \quad (15)$$

One can readily see that the Bell inequality is fulfilled for the $\rho_{\Sigma f}$ states.

Statement 1. If matrix P is representable as a sum (14) with n terms, it cannot be represented as an analogous sum with a different number of terms.

This statement follows from the fact that there are only three linearly independent matrices of the form (12).

Thus, we have found that all matrices P are divided into four nonintersecting classes: those irrepresentable in the form of sum (14) and those representable in the form of such sums containing one, two, and three terms.

Let us now study the relationship between the matrices ρ and P and find out which ρ matrices correspond to the same matrix P .

Statement 2. For every matrix P there is a six-parameter set of ρ matrices. Their elements are

$$\begin{aligned}\rho_{14} &= 1/4[P_{11} - P_{22} - i(P_{12} + P_{21})], \\ \rho_{23} &= 1/4[P_{11} + P_{22} + i(P_{12} - P_{21})],\end{aligned}\quad (16)$$

$$\begin{aligned}\rho_{11} &= 1/4(1 + P_{33} + A_1 + A_2), \\ \rho_{22} &= 1/4(1 - P_{33} - A_1 + A_2), \\ \rho_{33} &= 1/4(1 - P_{33} + A_1 - A_2), \\ \rho_{44} &= 1/4(1 + P_{33} - A_1 - A_2),\end{aligned}\quad (17)$$

$$\begin{aligned}\rho_{13} &= 1/4[(P_{13} - iP_{23}) + (A_{13} + iB_{13})], \\ \rho_{24} &= 1/4[-(P_{13} - iP_{23}) + (A_{13} + iB_{13})],\end{aligned}\quad (18)$$

$$\begin{aligned}\rho_{12} &= 1/4[(P_{31} - iP_{32}) + (A_{12} + iB_{12})], \\ \rho_{34} &= 1/4[-(P_{31} - iP_{32}) + (A_{12} + iB_{12})].\end{aligned}\quad (19)$$

Here,

$$A_1, A_2, A_{12}, B_{12}, A_{13}, B_{13}\quad (20)$$

are arbitrary real parameters.

This result is consistent with the fact that the matrices P and ρ are described by 9 and 15 parameters, respectively. The ranges of parameters (20) are determined by the following constraints on the density matrix elements (6):

$$\rho_{ii} \leq 1, \quad \rho_{ii}\rho_{jj} \leq \rho_{ij}\rho_{ji}.\quad (21)$$

To this point, no assumptions were made about the structure of the P and ρ matrices. Now let the matrix ρ be factorable, i.e., representable in the form (9). It is in correspondence with a factorable P matrix of the form (12). According to Statement 2, there is a six-parameter set of matrices ρ that are also in correspondence with P . Let us clarify what restrictions should be imposed on parameters (20) for the factorable matrices to be separated from this set.

Statement 3. For every matrix P representable in the form (12) there is a one-parameter set of factorable matrices ρ . Their elements are determined by Eqs. (16)–(19) with the following additional constraints on parameters (20):

$$\begin{aligned}A_1 A_2 &= P_{33}, \quad P_{13} B_{13} = -P_{23} A_{13}, \\ P_{31} B_{12} &= -P_{32} A_{12}, \\ A_1(A_{13} + iB_{13}) &= P_{13} - iP_{23}, \\ A_2(A_{12} + iB_{12}) &= P_{31} - iP_{32}.\end{aligned}\quad (22)$$

We have found that parameters (20) must satisfy relations (22) in order for the matrix ρ reconstructed from the matrix P to be factorable. If these conditions are not fulfilled, the matrix ρ is irrepresentable in the form (9). It is also irrepresentable as a sum (10) because, according to Statement 1, in this case its matrix P could not be written in the form (12). Never-

theless, the Bell inequality is fulfilled for the states with such a density matrix.

Thus, we have found a six-parameter set of states whose density matrices are not factorized and are not separable, but which satisfy the Bell inequality. In a more general case, they should be supplemented by the states whose P matrix is representable as sum (14) with two and three terms.

The states possessing factorable P matrices (12) will be called the P -factorable states; similarly, the P -separable states possess P matrices (14); and P matrices of the P -entangled states cannot be represented in the form (14).

Using the P -matrix technique, one can refine the Bell inequalities by expressing their right-hand sides through the parameters of the P matrices of the respective state. Note, first of all, that Bell inequality (15) is fulfilled for pure factorable states and there are sets of vectors for which this inequality transforms to an equality. Indeed, Eq. (13) is valid for factorable states. It is easy to see that, if the state ρ^α is pure, the vector \mathbf{r}^α has unit length:

$$|\mathbf{r}^\alpha| = 1.\quad (23)$$

If this state is mixed, then $|\mathbf{r}^\alpha| < 1$. Therefore, for factorable states (9), taking Eq. (13) into account, one can obtain the inequality

$$|E(\mathbf{a}, \mathbf{b}) + E(\mathbf{a}, \mathbf{c}) + E(\mathbf{d}, \mathbf{b}) - E(\mathbf{d}, \mathbf{c})| \leq 2|\mathbf{r}^\alpha||\mathbf{r}^\beta|.\quad (24)$$

It is also seen from Eq. (13) that the Bell inequality can transform to an equality for the pure states and the specific choice of vectors \mathbf{a} , \mathbf{b} , \mathbf{c} , and \mathbf{d} ; as to the mixed states, they satisfy inequality (24), which is stronger than the initial inequality (15). Such inequalities will be referred to as the generalized Bell inequalities. The right-hand side of this inequality can be as small as desired.

To this point, the two-particle P -factorable states were considered. These states satisfy inequality (24). If the state is P -separable, then each term in Eq. (14) satisfies inequality (24) multiplied by the respective coefficient. For the whole state, the inequality may be stronger than the sum of individual inequalities.

Let us now consider the P -entangled state Ψ_E formed by the states Ψ_1 and Ψ_2 with probabilities w_1 and w_2 :

$$\begin{aligned}\Psi_1 &= \alpha\Psi_{++} + \beta\Psi_{--}, \quad \Psi_2 = \gamma\Psi_{+-} + \delta\Psi_{-+}, \\ |\alpha|^2 + |\beta|^2 &= 1, \\ |\gamma|^2 + |\delta|^2 &= 1, \quad w_1 + w_2 = 1.\end{aligned}\quad (25)$$

The corresponding P matrix is

$$P_E = \begin{pmatrix} (\gamma\delta^* + \gamma^*\delta)w_2 + (\alpha\beta^* + \alpha^*\beta)w_1 & 0 & 0 \\ 0 & (\gamma\delta^* + \gamma^*\delta)w_2 - (\alpha\beta^* + \alpha^*\beta)w_1 & 0 \\ 0 & 0 & w_1 - w_2 \end{pmatrix}. \quad (26)$$

Selecting α , β , γ , and δ so as to satisfy the condition

$$\begin{aligned} (\alpha\beta^* + \alpha^*\beta)w_1 &= 0, \\ (\gamma\delta^* + \gamma^*\delta)w_2 &= (w_1 - w_2), \end{aligned} \quad (27)$$

one obtains that state (26) satisfies the generalized Bell inequality

$$\begin{aligned} |E(\mathbf{a}, \mathbf{b}) + E(\mathbf{a}, \mathbf{c}) + E(\mathbf{d}, \mathbf{b}) - E(\mathbf{d}, \mathbf{c})| \\ \leq 2\sqrt{2}|w_1 - w_2|. \end{aligned} \quad (28)$$

It is seen that, depending on the probabilities of the pure states in the mixed state, the right-hand side of inequality (28) can be both as small as desired and large enough to violate the standard Bell inequality (15).

In the general case, the generalized Bell inequality has the form

$$\begin{aligned} |E(\mathbf{a}, \mathbf{b}) + E(\mathbf{a}, \mathbf{c}) + E(\mathbf{d}, \mathbf{b}) - E(\mathbf{d}, \mathbf{c})| \\ \leq \sqrt{2} \sup_{\mathbf{n}_1, \mathbf{n}_2} (\|P(n_1)\| + \|P(n_2)\|), \end{aligned} \quad (29)$$

where sup is taken over all pairs of vectors n_1, n_2 satisfying the conditions

$$(\mathbf{n}_1, \mathbf{n}_2) = 0, \quad \|n_1\| = \|n_2\| = 1.$$

It immediately follows from the definition (7) of operator P that $\|P\| \leq 1$; therefore, the maximum value of the right-hand side of inequality (29) is $2\sqrt{2}$. As is seen from Eq. (28), this value is attained for the pure entangled states.

The above analysis demonstrates that, from the fact that a certain state satisfies Bell inequality (15), one cannot draw any definite conclusion about the nature of this state. It may be both entangled and factorable. If inequality (15) is violated, the corresponding state is necessarily entangled.

An alternative conclusion is the following: for every state there is a more rigorous generalized inequality whose right-hand side is determined by the norm of the P matrix of this state. For the pure factorable states, this norm is unity and they satisfy the usual inequality (15);

for the separable and mixed factorable states, the norm of the P matrix is strictly less than unity and they satisfy the generalized Bell inequality (24). The entangled states satisfy generalized inequalities (29).

REFERENCES

1. A. Einstein, B. Podolsky, and N. Rosen, Phys. Rev. **47**, 777 (1935).
2. N. Bohr, Phys. Rev. **48**, 696 (1935).
3. J. S. Bell, Physics (Long Island City, N.Y.) **1**, 195 (1964).
4. A. Bohm, *Quantum Mechanics: Foundations and Applications* (Springer-Verlag, New York, 1986; Mir, Moscow, 1990).
5. R. F. Werner, Phys. Rev. A **40**, 4277 (1989).
6. S. Popescu, Phys. Rev. Lett. **72**, 797 (1994); **74**, 2619 (1995).
7. M. Horodecki, P. Horodecki, and R. Horodecki, Phys. Lett. A **210**, 377 (1996); **223**, 1 (1996).
8. M. Horodecki, P. Horodecki, and R. Horodecki, Phys. Rev. Lett. **78**, 574 (1997); **80**, 5239 (1998).
9. A. Peres, Phys. Rev. Lett. **80**, 2245 (1998).
10. M. Levenstein and A. Sanpera, Phys. Rev. Lett. **80**, 2261 (1998).
11. R. Horodecki, M. Horodecki, and P. Horodecki, Phys. Rev. A **59**, 1799 (1999).
12. R. Garisto and L. Hardy, Phys. Rev. A **60**, 827 (1999).
13. T. F. Jordan, Phys. Rev. A **60**, 2726 (1999).
14. D. V. Strekalov, Y.-H. Kim, and Y. Shin, Phys. Rev. A **60**, 2685 (1999).
15. V. V. Dodonov and V. I. Man'ko, Phys. Lett. A **229**, 335 (1997).
16. O. V. Man'ko and V. I. Man'ko, Zh. Éksp. Teor. Fiz. **112**, 796 (1997) [JETP **85**, 430 (1997)].
17. V. A. Andreev and V. I. Man'ko, Zh. Éksp. Teor. Fiz. **114**, 437 (1998) [JETP **87**, 239 (1998)].
18. V. A. Andreev and V. I. Man'ko, J. Opt. B **2**, 122 (2000).

Translated by R. Tyapaev